

Departamento de Electricidad y Electrónica
UNIVERSIDAD DEL PAIS VASCO
THE UNIVERSITY OF THE BASQUE COUNTRY



Universidad
del País Vasco

Euskal Herriko
Unibertsitatea

CAMPUS OF
INTERNATIONAL
EXCELLENCE

Near- and Far-field Studies of Polariton-Enhanced Interactions
between Light and Molecules

Thesis by
Andrei Bylinkin

for the degree of
Doctor of Philosophy in Physics

Supervised by
Dr. Alexey Nikitin and
Prof. Rainer Hillenbrand

Donostia-San Sebastian, Spain, April 2024



Resumen

La interacción de la luz con la materia juega un papel importante en diversos campos científicos y tecnológicos. Algunos ejemplos básicos de interacciones entre la luz y la materia incluyen, pero no se limitan a, la reflexión, transmisión, dispersión, absorción y emisión de luz. Estas interacciones son cruciales para una variedad de aplicaciones, que van desde el desarrollo de dispositivos ópticos, como lentes y espejos, hasta la creación de soluciones energéticas como paneles solares, e incluso en técnicas de imagen en medicina y tecnologías de comunicación. Asimismo, entender las diferentes interacciones entre la luz y la materia nos permite manipular la luz para diversos fines, desde mejorar la eficiencia de los sistemas de conversión de energía hasta mejorar el rendimiento de dispositivos electrónicos y fotónicos.

El acoplamiento fuerte (SC, por sus siglas en inglés) entre la luz y las excitaciones dipolares en la materia es un tipo de interacción particularmente interesante donde pueden emerger nuevos estados híbridos conocidos como polaritones. Los niveles de energía de estos estados híbridos tienen una separación mayor que la suma de las anchuras individuales de línea [1]. Por lo general, lograr un acoplamiento fuerte con una pequeña cantidad de materia, como capas delgadas o moléculas individuales, requiere aumentar el confinamiento y la mejora del campo alrededor de la materia. Frecuentemente, esto se logra posicionando la materia dentro de un resonador óptico convencional, como una microcavidad de Fabry-Pérot. Es importante destacar que el SC abre nuevas posibilidades para controlar y manipular propiedades de los materiales, como el transporte de portadores en semiconductores orgánicos [2, 3], la reactividad química de las moléculas [4–7] o el magnetotransporte en gases de electrones bidimensionales [8].

El SC también puede ocurrir en capas o superficies delgadas, cuando una excitación dipolar es fuerte, como aquellas que se producen por las oscilaciones de electrones en metales o las vibraciones de la red en cristales polares. Esto conduce a la aparición de plasmones polaritones de superficie (SPPs, por sus siglas en inglés) y fonones polaritones (PhPs, por sus siglas en inglés). Estos polaritones poseen una longitud de onda más corta en comparación con la longitud de onda de la luz en el espacio libre, así como un gran confinamiento del campo electromagnético. De hecho, el uso de estos polaritones en lugar de la luz permite reducir significativamente la cantidad de materia requerida para lograr el SC, abriendo así nuevas oportunidades para desarrollar dispositivos y sensores optoelectrónicos compactos, ultrasensibles y eficientes [9–11]. Un enfoque práctico del SC a la nanoescala es utilizar resonadores polaritónicos, que permitan el SC, por ejemplo, entre excitones y SPPs a frecuencias visibles [12] o entre vibraciones moleculares y PhPs

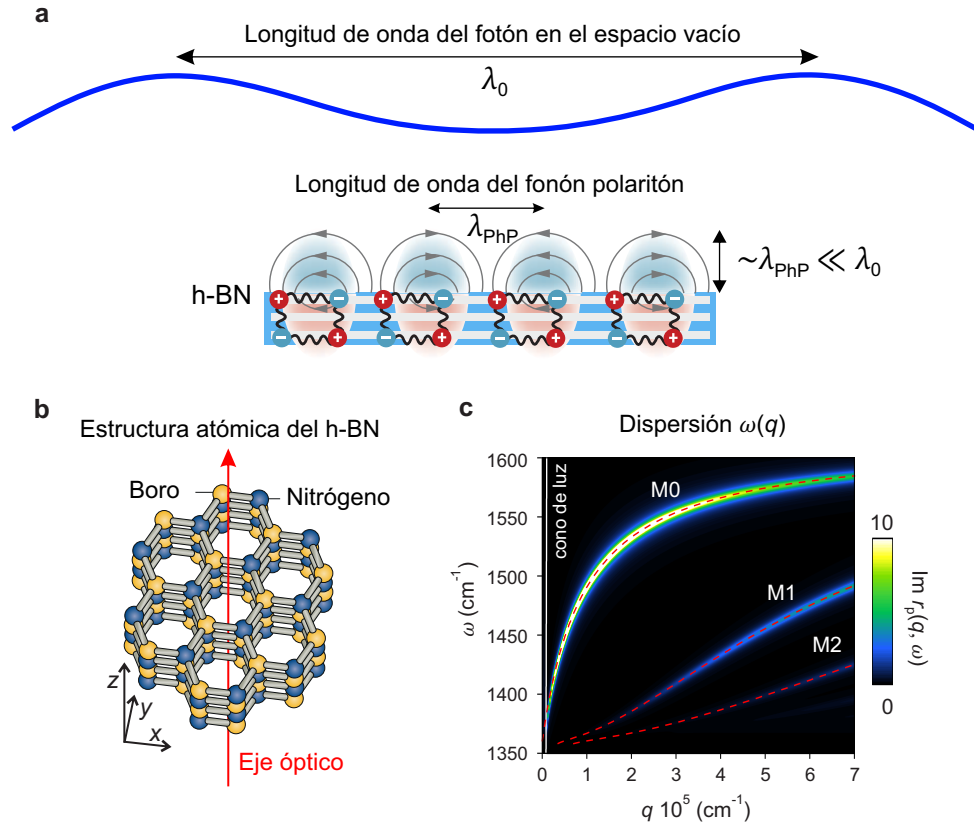


Figure 1: PhPs ultraconfinados en una capa delgada de h-BN. **a**, Ilustración de PhP – luz acoplada a vibración de la red cristalina – en una capa delgada de h-BN. **b**, Estructura atómica de h-BN. **c**, El gráfico de colores muestra la componente imaginaria del coeficiente de reflexión de Fresnel, $\text{Im}[r_p(q, \omega)]$, de una capa de h-BN de 40 nm de espesor rodeada por aire. Las curvas discontinuas en rojo muestran la relación de dispersión de los modos PhP M0, M1 y M2. La línea blanca muestra la relación de dispersión de la luz en aire.

a frecuencias de infrarrojo [13, 14] y THz [15, 16].

Los PhPs en cristales de van der Waals (vdW) han surgido recientemente como candidatos prometedores para lograr a la nanoescala un acoplamiento fuerte entre la luz infrarroja y las vibraciones moleculares (conocido como acoplamiento fuerte vibracional, VSC, por sus siglas en inglés). Estos PhPs permiten un mayor confinamiento y mejora del campo en el infrarrojo. Aumentan los tiempos de vida a los picosegundos y pueden sintonizarse a través del grosor del cristal y los entornos dieléctricos que los rodean [17, 18]. Es importante señalar que los PhPs se ajustan espectralmente con algunas resonancias vibracionales moleculares que aparecen en el rango de frecuencias infrarrojas. De hecho, los PhPs localizados en nanorresonadores con un alto factor de calidad, Q , hechos de nitruro de boro hexagonal (h-BN, por sus siglas en inglés) se emplearon recientemente para lograr VSC [13, 14]. Estas aplicaciones enfatizan el potencial del h-BN para su uso tanto en la espectroscopía infrarroja de campo lejano ultrasensible, como su relevancia hacia el control local de la reactividad química. A pesar de estas importantes aplicaciones, el potencial que poseen los PhPs ultraconfinados propagantes en capas no estructuradas para la espectroscopía vibracional molecular mejorada por polaritones no ha sido investigado

experimental ni teóricamente. La imagen a la nanoescala (nanoimagen) en el espacio real de los modos híbridos no ha sido estudiada hasta ahora, pero es crucial para un análisis detallado experimental del VSC explotando PhPs. Además, la combinación de PhPs y SPPs para generar campos electromagnéticos fuertemente confinados (*hotspots*) tanto en frecuencias infrarrojas como visibles — un componente esencial para lograr SC a la nanoescala — en las mismas posiciones espaciales y con dimensiones similares aún no ha sido investigada. Esta tesis introduce experimentos de nanoimagen en infrarrojo para estudiar las interacciones entre los PhPs propagantes ultraconfinados y las vibraciones moleculares. Además, estudia el acoplamiento de doble banda entre la luz y las moléculas diseñando una heteroestructura que soporta SPPs y PhPs en las frecuencias visibles e infrarrojas, respectivamente.

Esta tesis está estructurada de la siguiente manera:

En el Capítulo 1 se introducen los conceptos básicos de cómo la luz interactúa con la materia. Primero se introducen los modelos para la función dieléctrica de la materia y posteriormente los modelos para la descripción de los polaritones en materiales del tipo vdW. En particular, se describen los modos confinados de PhP en el infrarrojo que aparecen en capas (ultra)delgadas de h-BN (véase Figura 1). En este capítulo también se discuten algunas propiedades de los polaritones y cómo estas propiedades permiten mejorar significativamente la interacción entre la luz y las moléculas, principalmente debido al confinamiento de campo cercano proporcionado por estos polaritones.

En el Capítulo 2 se presentan las principales técnicas experimentales y los formalismos teóricos utilizados en esta tesis. Se comienza con una breve discusión sobre la microscopía óptica de campo cercano de tipo dispersivo (s-SNOM, por sus siglas en inglés), incluyendo la nanoimagen s-SNOM de frecuencia única y la espectroscopía de transformada de Fourier a nanoescala (espectroscopía nano-FTIR, por sus siglas en inglés). Posteriormente se explican las técnicas de supresión de fondo utilizadas en s-SNOM, cruciales para recuperar la señal de campo cercano sin fondo. En el capítulo también se discute la técnica de interferometría de polaritones, la cual es importante para la imagen de polaritones ultraconfinados usando s-SNOM [19–22]. Por otro lado, se presenta el modelo de osciladores armónicos acoplados, el cual es un método simple pero ampliamente utilizado para analizar e interpretar datos experimentales en el contexto de SC entre luz y materia. Partiendo del método de la matriz de transferencia y determinando los polos de la reflectividad, en la última sección del capítulo se analizan los modos normales para obtener información acerca de la dispersión de polaritones interactuando con otras excitaciones, particularmente vibraciones moleculares.

En el Capítulo 3 se presentan los resultados experimentales de nanoimagen en el infrarrojo para estudiar las interacciones entre PhPs ultraconfinados en h-BN y vibraciones moleculares en la capa de un semiconductor orgánico, específicamente 4,4'-bis(N-carbazolil)-

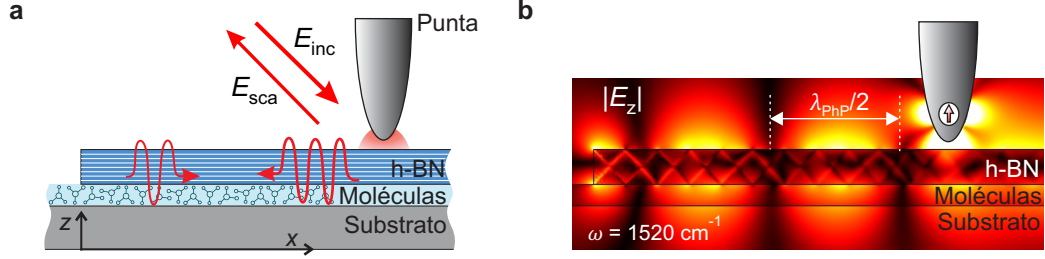


Figure 2: Observación en el espacio real del acoplamiento fuerte entre PhP y moléculas. **a**, Ilustración del experimento de nanoimagen. **b**, Distribución del campo cercano simulado (componente z), generada por una fuente de dipolo puntual (esquematiada por la flecha roja) que imita la punta iluminada. Fuera de la placa de h-BN, el campo cercano revela esencialmente la interferencia del modo PhP M0.

1,1'-bifenilo (moléculas de CBP). Utilizando espectroscopía nano-FTIR y nanoimagen s-SNOM de frecuencia única, se realizó la interferometría de PhPs. Esto último permite estudiar una interacción entre PhPs en capas delgadas no estructuradas de h-BN y excitaciones en moléculas de CBP (ubicadas debajo de las capas de h-BN mostradas en los esquemas en las Figuras 2a y 2b). A diferencia de los experimentos tradicionales de acoplamiento fuerte, como aquellos que involucran la configuración de Kretschmann-Raether o nanorresonadores de polaritones, la interferometría de PhPs permite la observación directa en el espacio real de los cambios que producen las resonancias vibracionales de las moléculas en las propiedades de los PhPs. En el primer experimento, la espectroscopía nano-FTIR permitió la reconstrucción de la relación de dispersión completa de los PhPs en un único barrido lineal, revelando la interacción entre el PhP y las moléculas, así como un incremento en el decaimiento espacial de los PhPs cerca de las resonancias vibracionales de las moléculas. Este incremento en el decaimiento espacial de los PhPs podría utilizarse en futuras aplicaciones para detectar huellas de las vibraciones moleculares a través de la acumulación de pérdidas del PhP. Cabe mencionar que los experimentos de nanoimagen s-SNOM de frecuencia única proporcionan una mejora en la relación señal-ruido y resolución espectral, permitiendo así un análisis cuantitativo de la interacción entre el PhP y la molécula. Esta interacción conduce a modificaciones significativas en la longitud de propagación de los PhPs y la aparición de dispersión anómala que evidencia la velocidad de grupo negativa. Por otro lado, determinando las frecuencias de los modos cuasinormales del sistema acoplado PhP-molécula, se obtuvo un anticruce y división en la relación de dispersión de los modos del sistema acoplado. Este anticruce evidencia el acoplamiento fuerte entre el PhP y la molécula, y además se logró reproducir mediante simulaciones numéricas. De hecho, mediante las simulaciones numéricas se muestra la factibilidad de alcanzar un acoplamiento fuerte con solo una monocapa de moléculas orgánicas, expandiendo así las posibilidades para experimentos futuros. Este capítulo demuestra que los PhPs propagantes en materiales de vdW no estructurados pueden acoplarse fuertemente con vibraciones moleculares, ofreciendo potencialmente una nueva plataforma para sondear el acoplamiento fuerte y controlar reacciones químicas a nivel local. Además, la fuerte interacción PhP-molécula facilita el desarrollo de sensores de

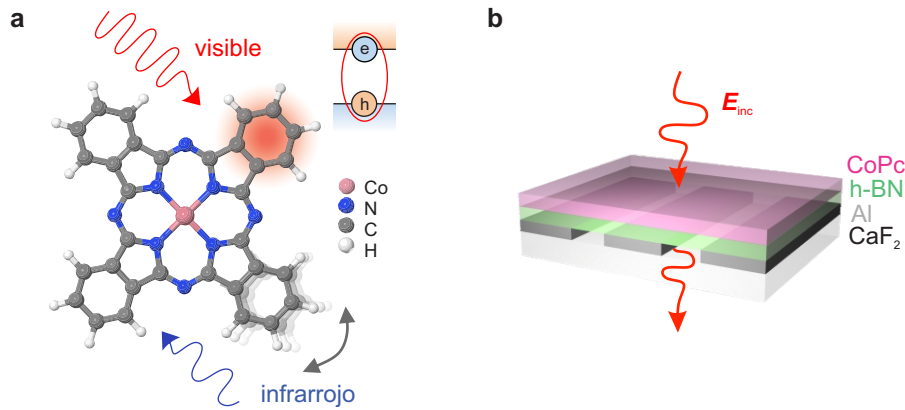


Figure 3: Acoplamiento de doble banda entre polaritones y excitaciones moleculares tanto en frecuencias visibles como infrarrojas. **a** Esquema de la estructura atómica de la molécula CoPc junto con sus resonancias vibracionales y excitónicas. **b** Esquema del experimento de campo lejano de los nanorresonadores polaritónicos cubiertos por la molécula.

espectroscopía ultracompactos y sensibles para integrar en un chip. Asimismo, una gran variedad de materiales de vdW presentan oportunidades para ir más allá del rango espectral del h-BN, como se demostró recientemente con la observación de PhP en MoO₃ y V₂O₅. Es importante señalar que, a diferencia de los enfoques convencionales que se basan en nanorresonadores, los cuales a menudo introducen pérdidas adicionales por daño de la muestra e incertidumbres de fabricación, este trabajo abre nuevos caminos para estudiar las interacciones fuertes entre luz y materia sin pasos de fabricación desafiantes adicionales, reduciendo así el daño a los materiales de vdW.

En el Capítulo 4, se utilizan simulaciones numéricas para demostrar que el acoplamiento fuerte puede lograrse simultáneamente entre polaritones de SPPs y transiciones electrónicas en frecuencias visibles, y entre PhPs y vibraciones moleculares en frecuencias infrarrojas en una heteroestructura libre de cavidad. La heteroestructura consiste en una capa de moléculas de ftalocianina de cobalto(II) (CoPc) colocada entre capas de aluminio (Al) y h-BN. Las moléculas de CoPc exhiben resonancias excitónicas y vibracionales en frecuencias visibles e infrarrojas, respectivamente (como se ilustra en la Figura 3a). Al posicionar las moléculas entre dos materiales polaritónicos (Al y h-BN), se logran campos electromagnéticos altamente confinados en las frecuencias visibles e infrarrojas dentro de la capa molecular (líneas discontinuas en la Figura 3a), asegurando una fuerte superposición de ambos campos y moléculas en el mismo lugar espacial. Los resultados experimentales se obtuvieron en nanorresonadores basados en heteroestructuras compuestas por *ribbons* de Al y capas de h-BN. Estos nanorresonadores soportan tanto SPPs como PhPs en los rangos de frecuencia visible e infrarrojo, respectivamente. La presencia y localización de dos *hotspots* se corroboró utilizando s-SNOM en ambos rangos de frecuencia visible e infrarrojo. En particular, al colocar moléculas sobre los nanorresonadores y realizar espectroscopía de campo lejano visible e infrarrojo (esquemático en la Figura 3b), se proporciona evidencia experimental directa de una gran división de modos en ambos ran-

gos de frecuencia. En este capítulo se demuestra que, mediante la ingeniería de una heteroestructura compuesta por materiales plasmónicos y fonónicos, se puede acceder simultáneamente a interacciones luz-materia dentro de las frecuencias visibles e infrarrojas. Esta configuración permite un acoplamiento fuerte luz-materia de doble banda, vinculando polaritones confinados (SPPs y PhPs) con las excitaciones electrónicas o vibracionales de moléculas. De hecho, al ajustar la dispersión de estos polaritones a través del grosor de las capas de la heteroestructura, se facilita el acoplamiento de momento y energía entre los polaritones y las excitaciones moleculares. Por lo tanto, el acoplamiento fuerte de doble banda puede ofrecer oportunidades novedosas para manipular reacciones químicas, avanzar en la imagen óptica y detección, o la conversión ascendente optomecánica, marcando así un paso adelante en la manipulación de interacciones luz-materia.

En conclusión, mediante el uso de técnicas de nanoimagen en campo cercano se demuestra el SC entre polaritones propagantes en cristales delgados de vdW y vibraciones moleculares en capas moleculares delgadas adyacentes. Además, los cálculos numéricos verifican los resultados experimentales y predicen el SC para capas moleculares de grosor nanométrico y polaritones en materiales vdW constituidos por pocas capas. Este resultado sugiere que los polaritones propagantes podrían servir como una plataforma prometedora para la espectroscopía en chip ultrasensible y experimentos futuros de SC. Asimismo, se introducen nanoresonadores de doble banda que poseen diferentes tipos de polaritones a frecuencias visibles e infrarrojas, que se acoplan simultáneamente a excitones y vibraciones moleculares en una capa molecular adyacente. Estas capacidades de acoplamiento de doble banda pueden ofrecer nuevas posibilidades para controlar el acoplamiento entre excitón y vibración molecular en futuras aplicaciones optoelectrónicas.

Summary

Light-matter interaction plays an important role in various scientific and technological fields. Basic examples of light-matter interactions include, but are not limited to, reflection, transmission, scattering, absorption, and emission of light. These interactions are crucial for a variety of applications, ranging from the development of optical devices, such as lenses and mirrors, to the creation of energy solutions like solar panels, and even in medical imaging techniques and communication technologies. Essentially, understanding light-matter interactions allows us to manipulate light for various purposes, from enhancing the efficiency of energy conversion systems to improving the performance of electronic and photonic devices.

Strong coupling (SC) is a particularly intriguing interaction regime between light and dipolar matter excitations where new hybrid states — polaritons — can emerge, whose energy level separation is larger than the sum of their average individual linewidths [1]. Achieving strong coupling with a small amount of matter, such as thin layers or individual molecules, requires increasing the field confinement and enhancement around the matter. This is often done by placing the matter inside a conventional optical resonator, like a Fabry-Pérot microcavity. Importantly, SC opens new possibilities for controlling and manipulating material properties, such as carrier transport in organic semiconductors [2, 3], chemical reactivity of molecules [4–7], or magnetotransport in two-dimensional electron gases [8].

Strong coupling can also occur in thin layers or surfaces, when dipolar excitations are strong, such as electron oscillations in metals or lattice vibrations in polar crystals. This leads to the emergence of surface plasmon polaritons (SPPs) and phonon polaritons (PhPs). These polaritons exhibit a shorter wavelength compared to free-space light and large field confinement. Employing these polaritons instead of light allows to significantly reduce the amount of matter required to achieve SC, thus opening opportunities for developing compact, ultrasensitive, and efficient optoelectronic devices and sensors [9–11]. A typical approach to explore SC at the nanoscale is to use polariton resonators, enabling SC between excitons and SPPs at visible frequencies [12] or between molecular vibrations and PhPs at mid-infrared (mid-IR) [13, 14] and THz frequencies [15, 16].

PhPs in van der Waals (vdW) crystals have recently emerged as particularly promising candidates for achieving strong coupling between infrared light and molecular vibrations (known as vibrational strong coupling, VSC) at the nanoscale. These PhPs offer particularly large mid-IR field confinement and enhancement, long picosecond lifetimes, and

tunability through crystal thickness and dielectric surroundings [17, 18]. Importantly, PhPs align spectrally with some molecular vibrational resonances prominent in the mid-IR frequency range. Indeed, localized PhPs in high-Q-factor nanoresonators made of hexagonal boron nitride (h-BN) were recently employed to achieve VSC [13, 14], highlighting the potential of h-BN for ultrasensitive far-field infrared spectroscopy and exciting perspectives towards local control of chemical reactivity. However, the potential of ultra-confined propagating PhPs in unstructured layers for polariton-enhanced molecular vibrational spectroscopy has neither been experimentally nor theoretically explored. Real-space nanoimaging of the hybrid modes has been also elusive so far, yet it is crucial for in-depth experimental analysis of VSC exploiting PhPs. Furthermore, the combination of ultra-confined PhPs and SPPs to generate strongly confined electromagnetic fields (hotspots) at both mid-IR and visible frequencies—an essential component for achieving SC at the nanoscale—at the same spatial positions and with similar dimensions has not yet been explored. This thesis reports mid-IR nanoimaging experiments to study the interactions between ultra-confined propagating PhPs and molecular vibrations. Additionally, it studies dual-band polariton-enhanced coupling between light and molecules by designing a heterostructure that supports SPPs and PhPs in the visible and mid-IR frequencies, respectively.

This thesis is structured as follows:

Chapter 1 introduces the basics of how light interacts with matter, starting with the models for the dielectric function of matter. It then covers polaritons in vdW materials, focusing on ultra-confined infrared PhP modes in thin h-BN layers. The chapter also discusses how unique properties of polaritons can significantly enhance the interaction between light and molecules, primarily due to the near-field confinement provided by these polaritons.

Chapter 2 covers the main experimental and theoretical approaches used in this thesis. It starts with a brief discussion on scattering-type scanning near-field optical microscopy (s-SNOM), including single frequency s-SNOM nanoimaging and nanoscale Fourier transform infrared spectroscopy (nano-FTIR spectroscopy). It then explains the background suppression techniques used in s-SNOM, crucial for retrieving background-free near-field signal. The chapter also discusses the so-called polariton interferometry, an important method for imaging ultra-confined polaritons using s-SNOM [19–22]. Next, it presents the coupled harmonic oscillators model, a simple yet widely used method to analyze and interpret experimental data in the context of strong coupling. Finally, it explores the eigenmode analysis, which involves determining the poles of reflectivity through the transfer matrix method to gain insights into the dispersion of polaritons interacting with other excitations, particularly molecular vibrations.

Chapter 3 presents mid-IR nanoimaging experiments to study the interactions between ultra-confined PhPs in h-BN and molecular vibrations in the organic semiconductor layer, specifically 4,4'-bis(N-carbazolyl)-1,1'-biphenyl (CBP molecules). Utilizing nano-FTIR spectroscopy and single-frequency s-SNOM nanoimaging we perform the PhPs interferometry. The latter enables studying an interaction between PhPs in thin unstructured h-BN layers and excitations in CBP molecules. In contrast to traditional strong-coupling experiments, such as those involving the Kretschmann-Raether configuration or polariton nanoresonators, PhPs interferometry enables direct real-space observation of how vibrational resonances of molecules impact PhP properties. In the first experiment, nano-FTIR spectroscopy enabled the reconstruction of the entire PhP dispersion relation in a single line scan, revealing the PhP-molecule interaction and increased spatial decay of PhPs near molecular vibrational resonances. This increased PhP spatial decay demonstrates a potential possibility to detect molecular vibrational signatures through PhP loss accumulation. Furthermore, single-frequency nanoimaging s-SNOM experiments provided an improved signal-to-noise ratio and spectral resolution, allowing for a quantitative analysis of the PhP-molecule interaction. The PhP-molecule interaction leads to significant modifications in PhP propagation length and the emergence of anomalous dispersion evidencing the negative group velocity. The frequencies of quasinormal modes of the PhP-molecule coupled system were determined, showing anti-crossing and mode splitting, as an evidence of the SC in excellent agreement with numerical calculations. Moreover, numerical simulations show the feasibility of achieving strong coupling with just a monolayer of organic molecules, expanding the possibilities for future experiments. This chapter demonstrates that propagating PhPs in unstructured vdW materials can strongly couple with molecular vibrations, potentially offering a new platform for testing strong coupling and controlling chemical reactions at a local level. Additionally, the strong PhP-molecule interaction facilitates the development of sensitive, ultra-compact, on-chip spectroscopy sensors. Moreover, a large variety of vdW materials presents exciting opportunities to go beyond the spectral range of h-BN, as recently demonstrated by PhP observation on MoO₃ and V₂O₅. Importantly, unlike conventional approaches that rely on nanoresonators, which often introduce additional losses from sample damage and fabrication uncertainties, this work opens new pathways for studying strong light-matter interactions without additional challenging fabrication steps, reducing the damage to vdW materials.

In Chapter 4, numerical simulations are used to demonstrate that SC can be simultaneously achieved between SPPs and electronic transitions at visible frequencies, and between PhPs and molecular vibrations at mid-IR frequencies in a cavity-free heterostructure. The cavity-free heterostructure consists of a layer of Cobalt(II) Phthalocyanine (CoPc) molecules placed between aluminium (Al) and h-BN layers. CoPc molecules exhibit both excitonic and vibrational resonances in visible and mid-IR frequencies, respectively. By positioning the molecules between two polaritonic materials (Al and h-BN), highly confined visible and mid-IR electromagnetic fields are achieved inside the molecular layer,

ensuring a strong overlap of both fields and molecules at the same spatial location. For experimental studies, nanoresonators based on heterostructure composed of Al ribbons and h-BN flakes are utilized. These nanoresonators support both SPPs and PhPs in the visible and mid-IR frequency ranges, respectively. The presence and co-localization of two hotspots are corroborated using s-SNOM in both visible and mid-IR frequency ranges. By placing molecules - for practical reasons - on the nanoresonators and performing visible and mid-IR far-field spectroscopy, direct experimental evidence of large mode splitting in both frequency ranges is provided. This chapter demonstrates that by engineering a heterostructure composed of plasmonic and phononic materials, one can simultaneously access light-matter interactions within both visible and mid-IR frequencies. This configuration enables dual-band strong light-matter coupling, linking confined polaritons (SPPs and PhPs) with the electronic or vibrational excitations of molecules. Adjusting the dispersion of these polaritons through the layer thickness of heterostructure facilitates momentum-energy coupling between the polaritons and molecular excitations. Future dual-band SC may offer novel opportunities for manipulating chemical reactions, advanced optical imaging and sensing, or optomechanical up-conversion, marking a step forward in the manipulation of light-matter interactions.

In conclusion, using near-field nanoimaging techniques, we demonstrate that SC can be achieved between propagating polaritons in thin vdW crystals and molecular vibrations in adjacent thin molecular layers. Our numerical calculations support our findings and also predict SC for nanometer-thin molecular layers and polaritons in few-layer vdW materials, which could make propagating polaritons a promising platform for ultra-sensitive on-chip spectroscopy and future SC experiments. Furthermore, we introduce novel dual-band nanoresonators hosting different types of polaritons at visible and mid-infrared frequencies, which simultaneously couple to excitons and molecular vibrations in an adjacent molecular layer. These dual-band coupling capabilities may offer new possibilities for controlling coupling between exciton and molecular vibration in future optoelectronics applications.

Contents

Resumen	i
Summary	vi
Chapter 1: Basics of light-matter interaction	1
1.1 Dielectric function of matters	2
1.2 Hybrid light-matter excitations (polaritons) in van der Waals materials . .	7
1.3 Near-field infrared interactions between light and molecules	13
Chapter 2: Experimental and theoretical methods	17
2.1 Scattering-type scanning near-field optical microscopy (s-SNOM)	18
2.1.1 Working principle of s-SNOM	18
2.1.2 Setup for s-SNOM and nano-FTIR spectroscopy	21
2.1.3 Imaging of ultra-confined polaritons (polariton interferometry) . .	22
2.2 Two-coupled harmonic oscillators model	28
2.3 Quasi-eigenmode analyses using transfer matrix approach	30
Chapter 3: Vibrational strong coupling between phonon polaritons and molecules	37
3.1 Introduction	38
3.2 Sample preparation	39
3.3 Hyperspectral phonon polariton interferometry	39
3.4 Quantitative analysis of coupling between phonon polaritons and molecules	43
3.4.1 Nanoimaging in the region of anomalous dispersion	43
3.4.2 Strong coupling analysis	44
3.4.3 Theoretical eigenmode analysis	46
3.5 Influence of layer thickness on coupling	47
3.6 Conclusion	49
3.7 Supplementary information	50
3.7.1 Dielectric function of materials	50
3.7.2 Data processing of the polariton interferometry experiments	52

Chapter 4: Dual-band coupling of polaritons with vibrational and electronic excitations in molecules	59
4.1 Introduction	60
4.2 Dual-band strong-coupling concept in a cavity-free structure	61
4.3 Sample preparation	63
4.4 Polaritonic nanoresonators	65
4.4.1 Far- and Near-field characterization	65
4.4.2 Theoretical analyses of the polaritonic modes	67
4.5 Coupling between polaritons and molecular excitations	69
4.5.1 Extinction spectra of the molecule covered nanoresonators	69
4.5.2 Quasi-normal mode analysis	71
4.5.3 Mode splitting from experimental extinction spectra	73
4.6 Mode splitting dependence on molecular layer thickness	78
4.7 Conclusion	79
4.8 Supplementary information	80
4.8.1 Dielectric function of materials	80
4.8.2 Data processing of the nanoimaging experiments	82
List of Publications	84
Bibliography	89
Acknowledgments	107

1

Basics of light-matter interaction

In this chapter, we provide a basic information about the interaction of light with various materials. It begins with an introduction of a Lorentz oscillator and Drude model for modelling the dielectric function of matters. Then we discuss the phenomena arising from the coupling of light with dipolar matter excitations, particularly phonon polaritons in van der Waals materials. The final section, focuses on exploiting the polaritons to enhance interactions between light and molecules, with implications in infared spectroscopy and strong-coupling experiments.

1.1 Dielectric function of matters

The dielectric function of materials, denoted as $\varepsilon(\omega)$ or relative permittivity, is pivotal in the fields of optics and electromagnetism. It describes how materials polarize under an electric field and subsequently influence the propagation of light. Various models have been developed to describe $\varepsilon(\omega)$, each tailored to different materials and their specific properties.

One of the frequently used models is the Lorentz oscillator model, which provides a classical, phenomenological description of the dielectric response in insulators, semiconductors, and molecules [23]. This model considers electrons and ions in matter as damped harmonic oscillators – similar to springs – that are driven by an external electromagnetic field. Essentially, it views polarizable matter as a set of identical, independent, and uniformly acting harmonic oscillators. Each oscillator, having mass m and charge e , is subject to a combination of forces: a linear restoring force $K\mathbf{x}$, where K is the spring constant and \mathbf{x} is the displacement from equilibrium; a damping force $b\dot{\mathbf{x}}$, where b is the damping constant; and a driving force produced by the electric field \mathbf{E} . The equation of motion for such an oscillator is:

$$m\ddot{\mathbf{x}} + b\dot{\mathbf{x}} + K\mathbf{x} = e\mathbf{E}. \quad (1.1)$$

Considering the electric field oscillates at frequency ω , $\mathbf{E}(t) = \mathbf{E}_0 e^{-i\omega t}$, the solution to the Eq. 1.1 can be derived and it is given by:

$$\mathbf{x}(t) = \frac{e}{m} \frac{\mathbf{E}(t)}{\omega_0^2 - \omega^2 - i\Gamma\omega}, \quad (1.2)$$

where $\omega_0 = (K/m)^{1/2}$ and $\Gamma = b/m$ represent the resonance frequency and the linewidth (damping) of the Lorentz oscillator, respectively. The complex relationship between \mathbf{x} and \mathbf{E} indicates that the displacement and the field are generally out of phase. To explore the implications of this phase difference, we express the displacement as $\mathbf{x} = Ae^{i\Theta}(e\mathbf{E}/m)$, where A and Θ denote the amplitude and phase, respectively, calculated as:

$$A(\omega) = \frac{1}{[(\omega_0^2 - \omega^2)^2 + \Gamma^2\omega^2]^{1/2}}, \quad (1.3)$$

$$\Theta(\omega) = \tan^{-1} \left(\frac{\Gamma\omega}{\omega_0^2 - \omega^2} \right). \quad (1.4)$$

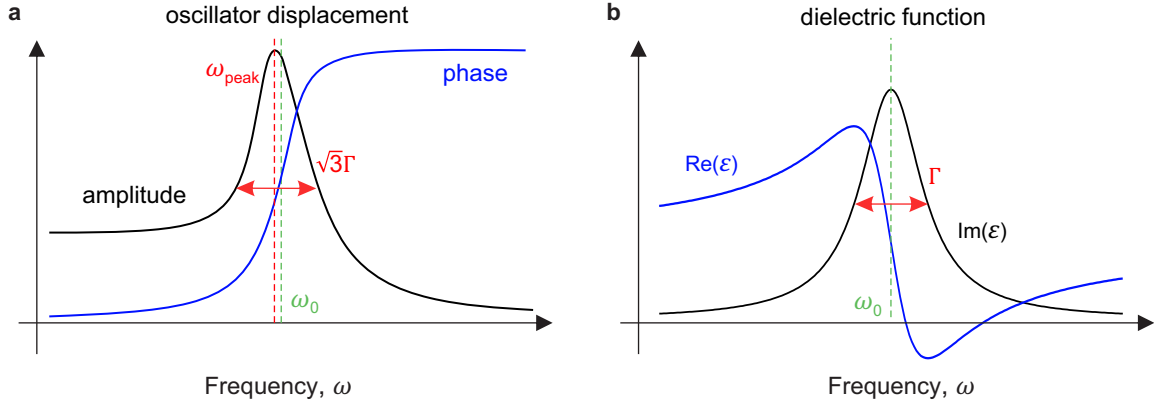


Figure 1.1: Illustration of the characteristics of the Lorentz model **a**, The amplitude and phase as a function of the frequency of the single damped oscillator. **b**, The real and imaginary part of the dielectric function. **a,b**, Vertical green line marks the resonance frequency of the oscillator, ω_0 .

Fig. 1.1a illustrates A and Θ as functions of frequency (black and blue curves, respectively). We note that the amplitude exhibits a peak at $\omega_{\text{peak}} = \sqrt{\omega_0^2 - \Gamma^2/2}$, with the peak's height inversely proportional to Γ , $A(\omega_{\text{peak}}) = (\Gamma\omega_0)^{-1}$, and the full width at half-maximum (FWHM) equals to $\sqrt{3}\Gamma$. At frequencies much lower than ω_0 , the oscillator responds in phase with the driving force ($\Theta \simeq 0^\circ$), whereas at frequencies significantly higher, ($\omega \gg \omega_0$), they are 180° out of phase, this transition happening near ω_0 (blue curve in Fig. 1.1a).

Analyzing a reaction of single oscillator to a time-harmonic electric field unveils optical constants for a group of such oscillators. The induced dipole moment \mathbf{p} of an oscillator is $e\mathbf{x}$. With n_0 oscillators per unit volume, the polarization \mathbf{P} (dipole moment per unit volume) becomes $\mathbf{P} = n_0\mathbf{p} = n_0e\mathbf{x}$, leading to:

$$\mathbf{P} = \frac{\omega_p^2}{\omega_0^2 - \omega^2 - i\Gamma\omega} \varepsilon_0 \mathbf{E}, \quad (1.5)$$

where the plasma frequency is defined as $\omega_p^2 = n_0e/m\varepsilon_0$, where ε_0 is the vacuum permittivity. Using a constitutive relation $\mathbf{P} = \varepsilon_0\chi\mathbf{E}$, where χ is the electric susceptibility of the matter, which directly connected with dielectric function $\varepsilon(\omega) = 1 + \chi(\omega)$. The resulting complex dielectric function can be expressed as:

$$\varepsilon(\omega) = 1 + \frac{\omega_p^2}{\omega_0^2 - \omega^2 - i\Gamma\omega}. \quad (1.6)$$

The real and imaginary parts of the dielectric function, $\varepsilon(\omega)$, are illustrated in Fig. 1.1b. It is important to note, that Eq. 1.6 implies that when frequency approaches infinity, $\omega \rightarrow \infty$, the dielectric function converges to 1, $\varepsilon(\omega \rightarrow \infty) = 1$. This value of dielectric function at $\omega \rightarrow \infty$ is often referred to as the high-frequency or background dielectric constant, denoted as ε_∞ . In real materials, various excitations occur across different frequency ranges, including microwave, infrared, visible, and ultra-violet. These excitations

collectively influence the dielectric function [24]. For accurate representation of dielectric function of materials in different frequency ranges, $\varepsilon(\omega \rightarrow \infty) = 1$ is substituted with ε_∞ . In result, the complex dielectric function is expressed as:

$$\varepsilon(\omega) = \varepsilon_\infty + \frac{\omega_p^2}{\omega_0^2 - \omega^2 - i\Gamma\omega}. \quad (1.7)$$

The Lorentz oscillator model adequately describes excitations resulting from the same type of oscillators in materials and is commonly applied to molecular vibrations in organic molecules in infrared frequency range. As an example of this, in Fig. 1.2a,b, we present an application of this model, illustrating the real and imaginary parts of the dielectric function for organic molecules. Here our focus is on the shape of the dielectric function. The real part of dielectric function exhibits a dispersive behaviour, crossing the ε_∞ at the resonance frequency of molecular vibration (Fig. 1.2a). We also note that oscillator strength of the molecular vibration is not so high and thus the real part of the dielectric function is typically positive. As discussed in note 1.1, the imaginary part of the dielectric function is characterized by a symmetric Lorentzian peak function, with a FWHM of Γ (Fig. 1.2b).

1.1. Imaginary part of the Lorentz dielectric function

It is important to note that when the frequency is close to the resonance frequency, specifically where $\omega_0 - \omega \ll \omega_0$, we can simplify the expression $\omega_0^2 - \omega^2$ using the approximation $\omega_0^2 - \omega^2 \approx 2\omega_0(\omega_0 - \omega)$. This allows us to express the dielectric function near resonance as:

$$\varepsilon(\omega) = 1 + \frac{\omega_p^2}{2\omega_0} \frac{1}{\omega_0 - \omega - i\frac{\Gamma}{2}}. \quad (1.8)$$

The imaginary part of the dielectric function can be thus represented by a symmetric Lorentzian peak function:

$$\text{Im}[\varepsilon(\omega)] = \frac{\omega_p^2}{2\omega_0} \frac{\frac{\Gamma}{2}}{(\omega_0 - \omega)^2 + (\frac{\Gamma}{2})^2} \propto L(\omega, \omega_0, \Gamma), \quad (1.9)$$

where ω_0 is the frequency of the peak and Γ is the peak's width at half its maximum height, known as the full width at half-maximum (FWHM).

Mathematically, the general form of the Lorentzian peak function is given by:

$$L(x, x_0, \Gamma) = \frac{1}{\pi} \frac{\frac{\Gamma}{2}}{(x_0 - x)^2 + (\frac{\Gamma}{2})^2}, \quad (1.10)$$

where x_0 is the center and Γ is a FWHM. The Lorentzian function is normalized so that $\int_{-\infty}^{\infty} L(x) dx = 1$.

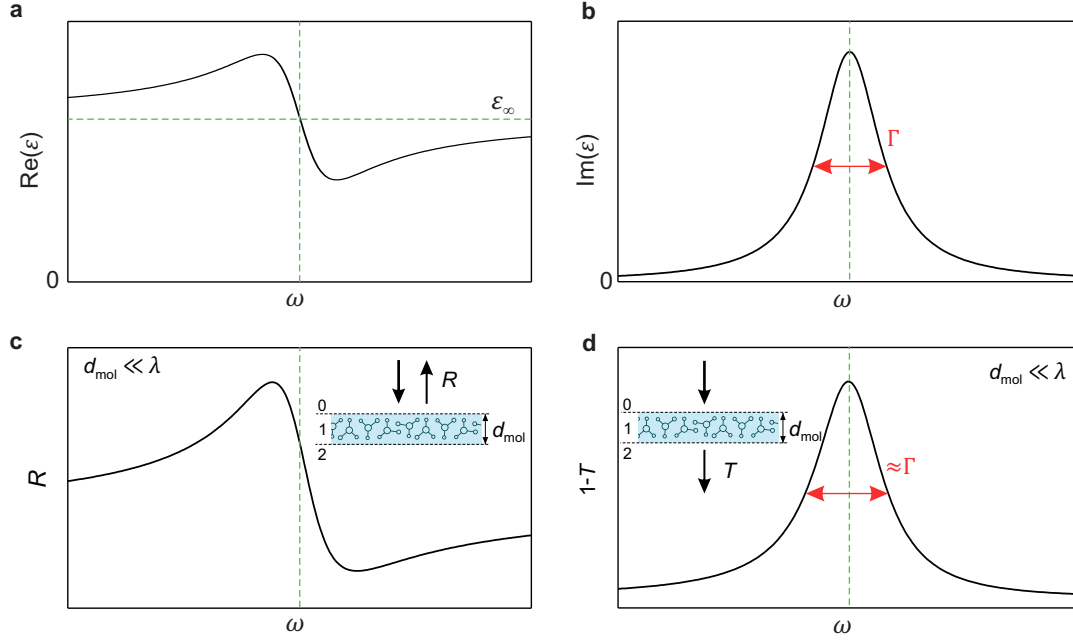


Figure 1.2: Illustration of dielectric function of infrared vibration of organic molecules at ω_0 (indicated by dashed vertical green line) **a,b**, The real and imaginary part of the dielectric function, respectively. **c,d** The reflection and transmission spectra of the thin layer of molecules with thickness, which is much smaller than the wavelength of the infrared light, $d_{\text{mol}} \ll \lambda$.

To associate dielectric function with experimentally measurable quantities, we calculate the reflection, R , and extinction spectra, $1 - T$, where T denotes the transmission spectra, of a thin layer of molecules surrounded by air at normal incident (see schematics in Fig. 1.2c,d). The calculations are performed considering the dielectric function of molecules illustrated in Fig. 1.2a,b, employing the Fresnel equations [25]:

$$\begin{aligned}
 R &= \left(\frac{r_{01} + r_{12}e^{2i\alpha}}{1 + r_{01}r_{12}e^{2i\alpha}} \right)^2, \\
 T &= \left(\frac{t_{01}t_{12}e^{i\alpha}}{1 + r_{01}r_{12}e^{2i\alpha}} \right)^2,
 \end{aligned} \tag{1.11}$$

where $r_{ik} = (\sqrt{\varepsilon_k} - \sqrt{\varepsilon_i}) / (\sqrt{\varepsilon_k} + \sqrt{\varepsilon_i})$, $t_{ik} = 1 + r_{ik}$ are the reflection and transmission coefficients, respectively, at interfaces between layers characterized by the dielectric functions ε_i and ε_k , with the indices $i, k = 0, 1, 2$ indicating specific layers (see schematics in Fig. 1.2c,d). The parameter α is given by $\alpha = \sqrt{\varepsilon_1} \frac{\omega}{c} d_{\text{mol}}$, where c and d_{mol} are the speed of light and thickness of the molecular layer, respectively. Fig. 1.2c,d show the calculated transmission and extinction spectra for a thin layer of molecules, where the layer's thickness is significantly smaller than the wavelength of the infrared light $d_{\text{mol}} \ll \lambda$, demonstrating that the reflection spectra echo the real part of $\varepsilon(\omega)$, while the extinction spectra resemble its imaginary part with a FWHM of about Γ .

In the context of polar crystals, which exhibit strong lattice vibrations, known as optical phonons, the dielectric function, Eq. 1.7, can be written in the following form [23]:

$$\varepsilon(\omega) = \varepsilon_\infty \left(\frac{\omega_{\text{LO}}^2 - \omega^2 - i\omega\Gamma}{\omega_{\text{TO}}^2 - \omega^2 - i\omega\Gamma} \right), \quad (1.12)$$

where ω_{TO} , ω_{LO} are the resonance frequencies of transverse (TO) and longitudinal (LO) optical phonons, respectively. Γ is a phenomenological linewidth (damping), which is associated with the TO phonon. We note that ω_{LO} is defined at the frequency where the dielectric function becomes zero. The frequency range between the TO and LO phonon frequencies, where the dielectric function turns negative, is known as the Reststrahlen band (from the German word for “residual rays”). This region is important in the materials science, as it often corresponds to strong absorption and reflectivity, influencing the optical properties of polar crystals.

The relationship between the TO and LO phonon frequencies can be understood through the Lyddane-Sachs-Teller (LST) relationship, which is given by:

$$\frac{\omega_{\text{LO}}^2}{\omega_{\text{TO}}^2} = \frac{\varepsilon(0)}{\varepsilon(\infty)}, \quad (1.13)$$

where $\varepsilon(0)$ and $\varepsilon(\infty)$ are the static and high-frequency dielectric constants of the material. The LST relationship is essential as it directly links the vibrations of the crystal lattice with the dielectric response of matter, helping us better understand the optical behaviour of polar crystals.

For metals or doped semiconductors, the Drude model is typically used, which provides a simplified yet effective description of the optical properties of these materials. This model assumes that the free electrons in material behave like a gas of charged particles, influencing the dielectric response under an electromagnetic field. We note that the Drude model is a special case of the previously discussed Lorentz model (Eq. 1.7), specifically under the condition when the resonance frequency, ω_0 , is considered to be zero. The dielectric function in Drude model is given by:

$$\varepsilon(\omega) = \varepsilon_\infty - \frac{\omega_p^2}{\omega^2 + i\Gamma\omega}. \quad (1.14)$$

In the high-frequency limit, where the frequency is significantly larger than the damping factor ($\omega \ll \Gamma$) and assuming $\varepsilon_\infty = 1$, the dielectric function in Drude model simplifies to:

$$\varepsilon(\omega) = 1 - \frac{\omega_p^2}{\omega^2}. \quad (1.15)$$

In this limit, the dielectric function becomes negative for frequencies below the plasma frequency, ω_p , indicating that electromagnetic waves are reflected with negligible losses. This characteristic explains why metals and doped semiconductors reflect light in the frequency range below ω_p , providing a basis for understanding their optical behavior.

In summary, this section has provided a brief overview of the dielectric function in various materials, an essential concept in the field of optics and electromagnetism. We have briefly discussed the Lorentz oscillator model, providing a classical viewpoint on dielectric behaviour in various materials. Then, the discussion on the dielectric properties of polar crystals, including the LST relationship, underscores the connection between lattice dynamics and dielectric response. Concluding with the Drude model we expanded our understanding to include how metals and doped semiconductors interact with light. The dielectric functions are crucial for the detailed exploration of material properties in the subsequent sections.

1.2 Hybrid light-matter excitations (polaritons) in van der Waals materials

Hybrid light-matter excitations, known as polaritons, constitute a rapidly evolving and captivating field in optics and physics. These excitations arise from the strong coupling between electromagnetic waves and oscillations in solid-state systems, thus blending the characteristics of light and matter [26, 27]. This unique interplay gives polaritons exceptional properties, most notably the ability to confine and manipulate light below the wavelength scale of photons, significantly surpassing the diffraction limit of photons. This capability is crucial for creating ultra-compact photonic devices that utilize the unique properties of polaritons [28–30]. Furthermore, by exploiting the large concentration of electromagnetic field associated with polaritons, it becomes possible to develop highly sensitive molecular sensors [31–33], opening new avenues in detection and sensing technologies.

Exploring polaritons in van der Waals (vdW) materials has significantly broadened polariton research [17, 18, 34]. These materials are characterized by their layered structures, featuring strong in-plane bonds and weaker van der Waals forces between layers. This structural feature allows the materials to be easily exfoliated into thin layers, providing a versatile platform for studying light-matter interactions. Additionally, restacking these exfoliated vdW layers into vertical heterostructures is possible, where electromagnetic coupling between polaritonic modes of adjacent layers leads to novel optical characteristics beyond those of the individual constituents [35–43]. Importantly, polaritons in vdW materials unlock new possibilities for exploring electronic phenomena and lattice dynamics. Specifically, polaritonic images allow us access to regions of the dispersion relations

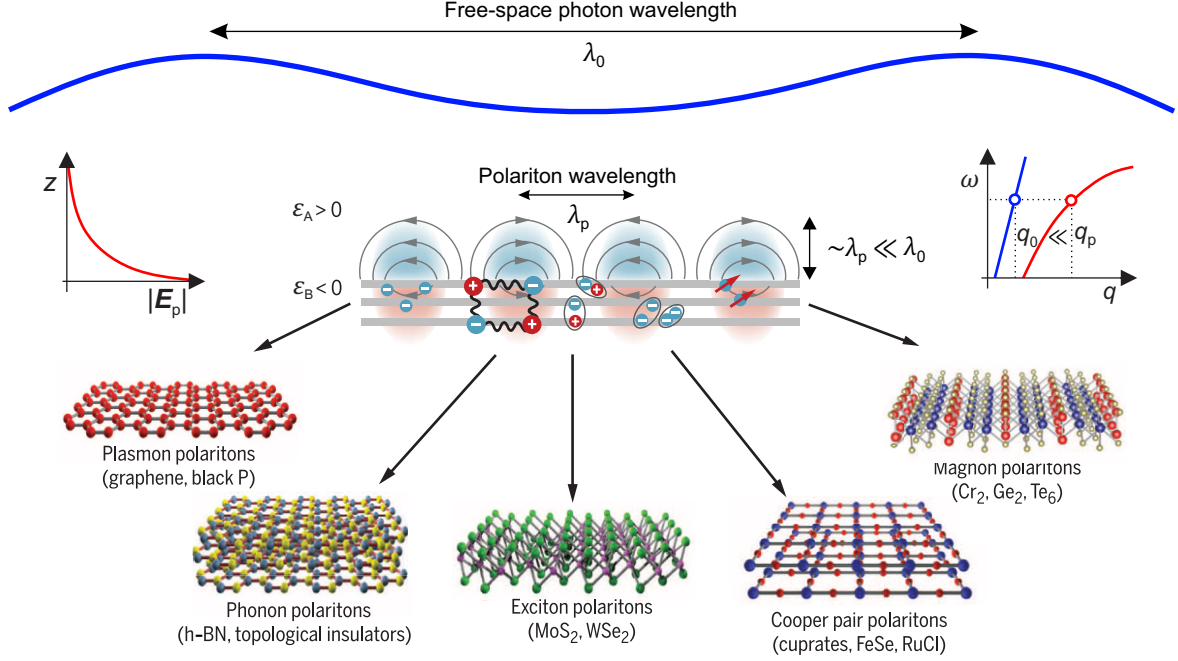


Figure 1.3: Overview of polaritons in van der Waals (vdW) materials. Polaritons, which are mixed light-matter oscillations, can arise in various physical phenomena: electrons in graphene and topological insulators (surface plasmon polaritons), infrared-active phonons in hexagonal boron nitride (phonon polaritons), excitons in dichalcogenide materials (exciton polaritons), superfluidity in FeSe- and Cu-based superconductors with high critical temperature T_c (Cooper-pair polaritons), and magnetic resonances (magnon polaritons). Different vdW materials support all these types of polaritons. The matter oscillation component in these polaritonic materials leads to a negative dielectric function ($\epsilon_B < 0$), facilitating the confinement of optical fields at the boundary with a positive-dielectric function ($\epsilon_A > 0$) medium. vdW polaritons yield significant confinement, measured by the ratio of the free-space photon wavelength (λ_0) to the polariton wavelength (λ_p). The left inset illustrates the exponential decay of the polariton field originating from the surface of the vdW material. The right inset illustrates the dispersion curves of photons and polaritons in blue and red, respectively. q_p and q_0 represent the momentum of polariton and free-space photon, respectively. Adapted from Ref. 17.

of various excitations that exceed the capabilities of conventional optics [19, 20, 44–49].

In vdW materials, various polaritonic excitations are distinguishable by their specific matter excitations (Fig. 1.3). For instance, plasmon polaritons in materials like graphene [19, 20] and black phosphorus [50, 51] arise from the coupling of conduction electrons with light. Phonon polaritons at mid-IR frequencies occur in materials such as h-BN [52] and MoO_3 [53], resulting from light’s interaction with bound atomic charges. Exciton polaritons, seen in MoS_2 and WSe_2 at visible and near-IR frequencies [54], emerge from light coupling with bound electron-hole pairs. Additionally, the emergence of Cooper pair polaritons in high- T_c superconductors [55] and magnon polaritons in ferromagnetic materials [56] are intriguing prospects.

The matter excitations in these materials lead to negative dielectric function, facilitating the confinement of the optical field at the boundary with a positive dielectric function medium (see illustration of the polariton field decay in Fig. 1.3). The anisotropic crystal structure of vdW materials may cause the in-plane and out-of-plane dielectric functions of

the same layered crystal to have opposite signs, leading to unusual behaviour of light with substantial field confinement (see detailed discussion about phonon polariton modes in a h-BN in page 10). This confinement significantly compresses the polaritons' wavelength relative to the wavelength of photons in free space, with compression ratios reaching 100 to 1000 in the THz and mid-IR frequency ranges. Such extreme confinement not only highlights the unique properties of vdW materials but also opens up possibilities for sub-wavelength light manipulation and enhanced light-matter interaction studies. In addition, the in-plane anisotropy of dielectric function leads to elliptic and hyperbolic polaritonic dispersion, a phenomenon that has garnered significant theoretical and experimental interest [57, 58]. Such dispersion relations are important in understanding the propagation and localization of electromagnetic waves in these materials, further enriching the field of nanophotonics and nano-optics.

The large momentum of polaritons in vdW materials, compared to free-space photons (see right inset in Fig. 1.3), presents a significant challenge in their excitation. We note that this large momentum can be also attributed to the thickness of the vdW materials, since polariton momentum is typically inversely proportional to the layer thickness of these materials [52, 59]. The main difficulty in exciting polaritons arises from momentum mismatch that needs to be compensated for effective polariton excitation. To address this issue, various methods, such as the nanostructuring of vdW materials [13, 60], the use of metallic antennas, gratings or cavities [61–64] are employed to effectively excite and study polaritons. Furthermore, polaritons can be effectively studied using a scattering-type scanning near-field optical microscope (s-SNOM) or electron energy loss spectroscopy (EELS) techniques. In the s-SNOM technique, the microscope's tip acts as an antenna, providing the necessary large momentum to excite these highly confined polaritons [19, 20, 52], whereas in the EELS technique the evanescent nature of the electromagnetic fields produced by a fast electrons offers the capability to investigate different polaritons [65–67].

Moreover, some of vdW materials can be tuned via external stimuli such as electric fields [68], mechanical strain [69] and chemical doping [70], presenting new opportunities for controlling and manipulating polaritonic modes. This ability to customize polaritonic responses is essential for developing devices with tailored properties, potentially transforming ultrafast photonic circuits, sensors, and quantum information processing [71–73].

In conclusion, the exploration of vdW polaritonics offers an exciting and promising avenue to investigate unique physical phenomena and apply these findings to enhance our comprehension and development of light-matter interactions. The study of vdW polaritonics is crucial for advancing numerous applications, including high-resolution imaging and the development of compact, efficient photonic devices and sensors [74–77].

Hyperbolic phonon polaritons in the h-BN layer

Hexagonal boron nitride (h-BN) has emerged as a key vdW material in the realm of mid-infrared nanophotonics. This material is composed of boron and nitrogen atoms covalently bonded along the plane, forming a hexagonal lattice, as shown in Fig. 1.4a. The B–N bond is polar covalent, due to a significant electronegativity difference between boron and nitrogen, which exceeds 0.4 eV [78]. h-BN’s layers are held together by van der Waals forces, similar to graphite [79]. The crystal structure of h-BN is highly anisotropic, leading to different frequencies for in-plane and out-of-plane lattice vibrational modes (optical phonons). This results in h-BN being an optically uniaxial material, with its optical axis aligned perpendicular to the layers of covalently bonded B–N atoms (aligned with the z -direction). The dielectric function of h-BN is represented by a diagonal tensor $\hat{\epsilon} = \text{diag}(\epsilon_x, \epsilon_y, \epsilon_z)$, where $\epsilon_x = \epsilon_y = \epsilon_{\perp}$ and $\epsilon_z = \epsilon_{\parallel}$.

The components of the dielectric tensor of h-BN are modeled using Eq. 1.12 [52, 80, 81]:

$$\epsilon_j(\omega) = \epsilon_{\infty,j} \left(\frac{\omega_{\text{LO},j}^2 - \omega^2 - i\omega\Gamma_j}{\omega_{\text{TO},j}^2 - \omega^2 - i\omega\Gamma_j} \right), \quad (1.16)$$

where $j = \perp, \parallel$. The parameters for the parallel components are $\epsilon_{\infty,\parallel} = 2.95$, $\omega_{\text{LO},\parallel} = 760 \text{ cm}^{-1}$, $\omega_{\text{TO},\parallel} = 825 \text{ cm}^{-1}$, $\Gamma_{\parallel} = 2 \text{ cm}^{-1}$. For the perpendicular components are $\epsilon_{\infty,\perp} = 4.9$, $\omega_{\text{LO},\perp} = 1360 \text{ cm}^{-1}$, $\omega_{\text{TO},\perp} = 1610 \text{ cm}^{-1}$ and $\Gamma_{\perp} = 7 \text{ cm}^{-1}$ [82]. We note that these parameters are attributed to standard h-BN crystals, typically referred to as ‘natural’.

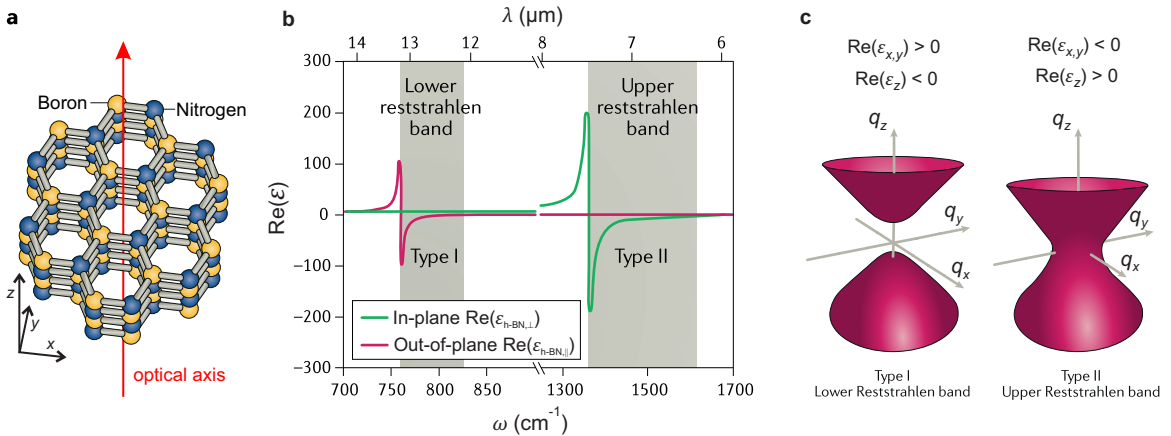


Figure 1.4: Hexagonal boron nitride (h-BN). **a** Atomic structure of h-BN. **b** The in-plane (ordinary, green) and out-of-plane (extraordinary, red) IR dielectric function of h-BN. In each of the two Reststrahlen bands, the real part of the dielectric function is negative for one of the two directions (ordinary or extraordinary) and positive for the other. **c** Isofrequency surfaces in the type I lower Reststrahlen band (left) and in the type II upper Reststrahlen band (right). Adapted from Ref. 77.

Fig. 1.4b shows the infrared dielectric function of h-BN. h-BN exhibits two Reststrahlen bands in the mid-IR frequency range, identified as the upper band ($\omega = 1360 - 1610 \text{ cm}^{-1}$) and the lower band ($\omega = 760 - 825 \text{ cm}^{-1}$), linked to the in-plane and out-of-plane optical phonons, respectively [81]. A distinctive feature is the opposite signs of the real parts of the dielectric function components in these bands, i.e., $\text{Re}(\varepsilon_{\parallel}) \cdot \text{Re}(\varepsilon_{\perp}) < 0$. This unique characteristic allows light to propagate through bulk h-BN within these Reststrahlen bands.

When light propagates through h-BN at the frequencies within these Reststrahlen bands, it exhibits unusual behavior. The isofrequency surface in reciprocal space, formed by the momentum of the PhPs, q , at a specific frequency, exhibits the shape of a hyperboloid, as shown in Fig. 1.4c. This contrasts sharply with the behavior of light in isotropic materials, where the isofrequency surface forms a sphere due to uniform momentum magnitude in all directions.

So far, we have discussed light propagation within bulk h-BN, where it exhibits unique behavior in the Reststrahlen bands. Now, we shift our focus to thin h-BN layers, frequently employed in nanophotonics experiments. A thin layer of h-BN supports a set of propagating PhPs modes, denoted Mn , which can be described by the following dispersion relation in the quasistatic limit [52]:

$$q(\omega) + i\kappa(\omega) = -\frac{\psi}{d} \left[\arctan\left(\frac{\varepsilon_1}{\varepsilon_{\perp}\psi}\right) + \arctan\left(\frac{\varepsilon_2}{\varepsilon_{\perp}\psi}\right) + \pi l \right], \psi = \frac{\sqrt{\varepsilon_{\parallel}}}{i\sqrt{\varepsilon_{\perp}}} \quad (1.17)$$

where $n = 0, 1, 2, \dots$ is the mode index. $\varepsilon_1, \varepsilon_2$ are the dielectric functions of materials above and below the h-BN slab, respectively. $q + i\kappa$ is a complex-valued momentum, which features an imaginary part that defines the amplitude decay (propagation) length, $L = \kappa^{-1}$ [22, 83, 84]. It is important to note that, more conventionally, the intensity decay (propagation) length is defined as $L_{\text{int}} = (2\kappa)^{-1}$ (see note in Section 2.3) [85, 86].

To discuss and analyze the PhP modes we choose a 40 nm thick h-BN layer surrounded by air as a representative example (the typical thickness of the exfoliated layers). We calculate and analyze the PhP modes in the frequencies of the upper Reststrahlen band, focusing on the same frequency range that will be used for PhP modes in the following chapters. An instructive way to visualize both the dispersion and the damping is via a colour plot of $\text{Im}[r_p(q, \omega)]$ at real q and ω (Fig. 1.5a) [23, 52]. We superpose the PhP dispersion, calculated using Eq. 1.17, for modes $n = 0, 1, 2$ (dashed red lines in Fig. 1.5a) onto the colour plot. The spatial distribution of the vertical component of the electric field for the M0, M1 and M2 modes at $\omega = 1420 \text{ cm}^{-1}$ is shown in Fig. 1.5c-e. Each Mn mode exhibits $n+1$ nodes in the vertical direction, such that the M0 mode possesses a single node. As can be seen in Fig. 1.5c-e, higher mode indices n result in increased lateral confinement and an increase in the momentum of the PhP mode.

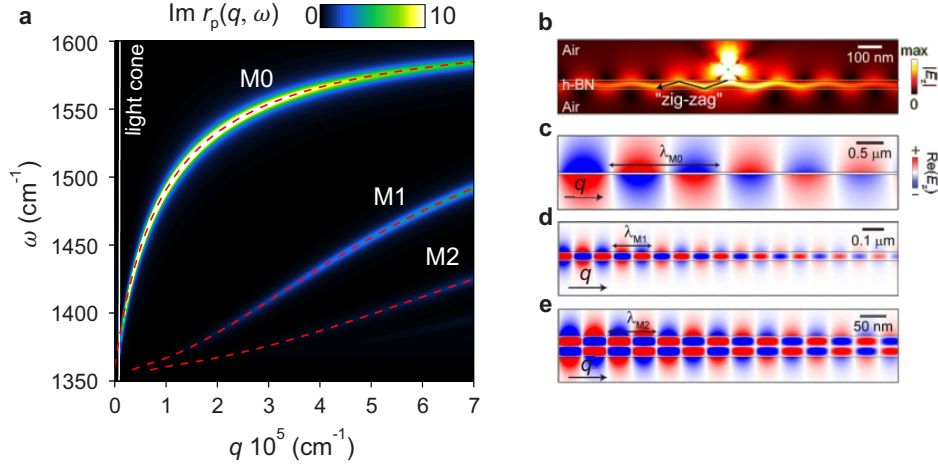


Figure 1.5: Phonon polariton (PhP) modes in thin h-BN layer. **a** Color plot shows calculated imaginary part of Fresnel reflection coefficient, $\text{Im}[r_p(q, \omega)]$, of a $d_{\text{h-BN}} = 40$ nm thickness layer surrounded by air ($\varepsilon_1 = \varepsilon_2 = 1$). The dashed red curves show the analytical dispersion calculated by Eq. 1.17. The white line shows the dispersion of the light in vacuum (light cone). **b** Dipole source (green dot) launching the PhPs of a thin layer, forming a characteristic "zig-zag" pattern due to the multiple reflection of the hyperbolic rays from the top and bottom slab surfaces, for the same system as in **a**. We note that this pattern can be explained as a superposition of the all slab modes. **c-e** Vertical component of the electric field of the **c** - M0 mode, **d** - M1 mode, and **e** - M2 mode, propagating from left to right. Note the different scale in each panel. The frequency in **b-d** is marked by the vertical dashed white line in **a**, $\omega = 1420$ cm^{-1} . **b-e** taken from Ref. 87.

Due to their large momenta, PhPs in unstructured layers cannot be effectively studied using far-field optical techniques, such as Kretschmann-Raether or Otto configurations [88, 89] due to limitations in the prism's dielectric constant. As an alternative, PhPs can be effectively studied using a scattering-type scanning near-field optical microscope (s-SNOM), a method where the microscope's tip acts as an antenna and efficiently excite PhPs providing the necessary large momentum (see Section 2.1 for more details). Additionally, PhPs can also be excited by other localized sources, such as a metallic antenna placed on the h-BN [62], a metal edge on the h-BN surface [22], or a wrinkle on the h-BN surface [90]. To illustrate the excitation of PhPs by a localized source, we calculate the electric field distribution induced by a vertically oriented dipole placed above the h-BN slab (Fig. 1.5b). We note that the "zig-zag" pattern near the dipole is a result of the superposition of many excited Mn modes [22, 91].

Recent advances in the synthesis of h-BN crystals have enabled the production of highly pure isotopically enriched crystals [92]. This improvement has significantly reduced phonon damping, thereby enhancing both the propagation length and the lifetime of the phonons by several times [80]. We note that the experiments conducted in Chapters 3 and 4 utilized isotopically enriched ^{10}B h-BN.

1.3 Near-field infrared interactions between light and molecules

The field of nanophotonics, which focuses on the manipulation of light at sub-wavelength scales, is experiencing significant progress in enhancing interactions between light and molecules, unlocking applications for fields ranging from environmental monitoring and defense to chemical analysis and medical diagnostics [11]. This progress is largely attributed to the development of new types of metasurfaces [93–96], photonic crystals [97, 98], and plasmonic nanostructures [99–101]. A prominent challenge in this domain is infrared spectroscopy [102], a pivotal technique for material characterization, which often encounters limitations with absorption cross-sections, especially when analyzing thin layers or small quantities of molecules.

To address this limitation, surface-enhanced infrared absorption (SEIRA) spectroscopy has emerged as a groundbreaking technique [103–106]. SEIRA enhances the interaction between infrared light and molecular vibrations, enhancing the vibrational signatures of materials without altering their intrinsic properties. This is primarily achieved using plasmon-resonant metallic structures, such as gratings [107], nanoparticles or antennas [105, 108–110], which intensify near-field interactions (see plasmonic nanoantenna example in Fig. 1.6a). Beyond traditional metals, SEIRA’s scope extends to metal oxides [111], highly doped semiconductors [112, 113], graphene [63, 114–116] and even dielectrics [96, 117], thereby broadening its range of applications.

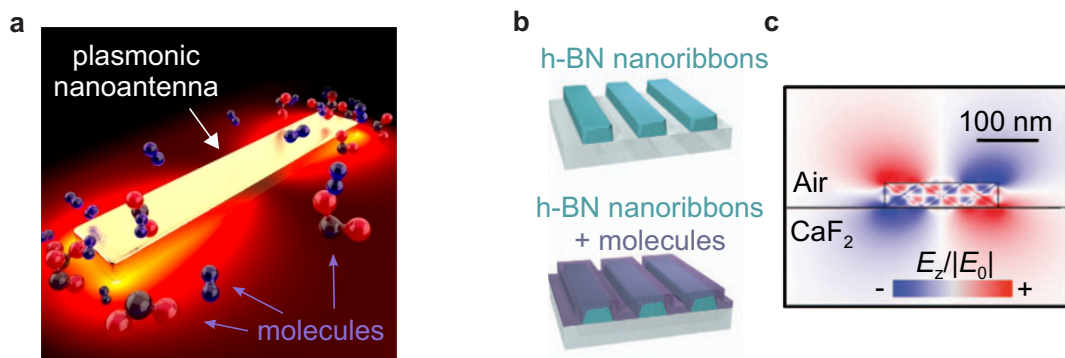


Figure 1.6: Surface-enhanced infrared absorption (SEIRA) spectroscopy. **a**, Illustration of a resonant plasmonic nanoantenna designed for SEIRA spectroscopy applications. It highlights the electric near-field confinement provided by this nanoantenna, which is used to enhance the vibrational signature of molecules located in the near-field of the plasmonic nanoantenna. **b**, h-BN nanoribbon array without (top image) and with a layer of molecules above the array (bottom image). **c**, Vertical electric near-field distribution normalized to the incident field for a single h-BN ribbon nanostructure ($E_z/|E_0|$). **a** adapted from Ref. 108, **b** and **c** adapted from Ref. 13.

While SEIRA significantly enhances light-matter interaction, it generally does not reach the threshold for strong coupling. Strong coupling occurs when light and matter states converge to form new hybrid states [1], whose separation of energy levels is larger than the sum of their average linewidths (more detailed discussion about the strong coupling criterion in the Section 2.2). In this context, strong coupling between infrared light and molecular vibration (vibrational strong coupling, VSC) is notable for its potential to control and manipulate molecular chemical reactivity [5, 118]. This represents an advancement in the field, pushing the boundaries of what is achievable in terms of molecular manipulation and sensory technology.

An important development in this area is the emergence of vdW materials, particularly h-BN, which has garnered significant attention for its unique properties [52, 77, 119], such as strong PhP resonances and hyperbolic PhP dispersion due to its anisotropic dielectric properties (see detailed discussion in subsection *Hyperbolic phonon polaritons in the h-BN layer* on page 10). h-BN supports propagating PhPs, which are distinguished by their extended lifetimes and long propagation lengths. The utility of h-BN nanoribbon arrays for SEIRA spectroscopy is underscored by their capacity to confine electromagnetic fields at ultra-small scales (see Fig. 1.6b,c), enabling the analysis of nanometer-thin molecular layers [13] and enhancing mid-IR gas sensing capabilities [120].

The use of monoisotopic variants of h-BN has resulted in significant enhancements in both the lifetime and propagation length of these polaritons, consequently leading to increased quality factors of PhP resonances in h-BN nanoribbon arrays. This advancement allows one to achieve vibrational strong coupling of organic molecules with localized PhP modes [14]. The extended lifetime of PhPs in monoisotopic h-BN are pivotal in achieving this result. Looking beyond h-BN, other polar materials like MoO_3 and V_2O_5 , which exhibit long-lived PhPs, promise to expand the material basis and spectral ranges of phononic SEIRA spectroscopy and strong coupling experiments, paving the way for future advancements in this field.

In conclusion, the integration of vdW materials, such as h-BN, into the field of enhanced light-molecule interaction – driven by SEIRA and the exploration of strong coupling phenomena – has opened new avenues for enhancing light-molecule interactions. This integration promises significant advancements in material science, chemistry, and biological sensing. h-BN and similar vdW materials hold great potential for these fields, offering new tools for precise light manipulation at the nanoscale and enhancing spectroscopic analysis.

2

Experimental and theoretical methods

In this chapter, we briefly describe and summarize the key techniques and models used in this thesis. It begins with a description of a scattering-type scanning near-field optical microscopy (s-SNOM), an experimental technique that allows for high-resolution optical imaging beyond the diffraction limit and analysis at the nanoscale. Then we describe a classical coupled harmonic oscillators model, which is instrumental in analyzing and fitting experimental data, particularly in the context of strong coupling. Finally, we discuss the theoretical method to calculate the quasi-eigenmodes using the transfer matrix approach, which is crucial for interpreting how light interacts with various materials.

2.1 Scattering-type scanning near-field optical microscopy (s-SNOM)

Scattering-type scanning near-field optical microscopy (s-SNOM) is a powerful technique in the fields of nano-optics and nanophotonics, enabling high-resolution imaging and spectroscopy of areas beyond the diffraction limit. It is particularly effective for investigating nanoscale phenomena in a variety of materials and structures. s-SNOM has shown great potential for probing and mapping polaritons in different structures. For example, s-SNOM has been used to map the near-field distributions of phononic and plasmonic nanoantennas [82, 121–123], as well as to image graphene plasmons [19, 20], phonon polariton in different vdW crystals [22, 52, 53, 84], as well as ultra-confined plasmon polaritons in the anisotropic material [124, 125].

2.1.1 Working principle of s-SNOM

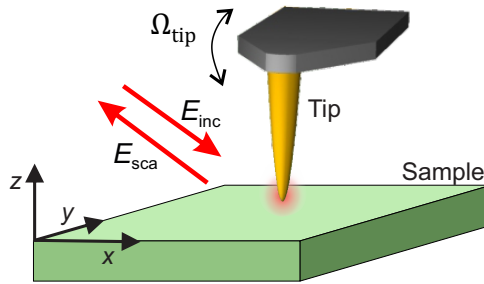


Figure 2.1: Working principle of s-SNOM and nano-FTIR. A laser beam of field E_{inc} illuminates a metallized AFM tip, which oscillates at the frequency Ω_{tip} . The tip acts as an optical antenna, concentrating the incident electric field into a nanoscale-sized electromagnetic hotspot directly beneath the tip apex, where the field enhancement is high. The field scattered by the tip, E_{sca} , depends on the sample region, which is located directly beneath the tip's apex. E_{sca} is collected as a function of the tip position.

s-SNOM operates on the principle of illuminating an oscillating sharp metallic tip with an incident light source, typically a laser, as shown in Fig. 2.1. This tip acts as an optical antenna, focusing the light into a small electromagnetic hotspot at the tip apex, primarily due to charge accumulation from the lightning rod effect [126]. When this tip, with its concentrated electromagnetic hotspot, is brought close to a sample, the near field of the tip interacts with the sample. This interaction depends on the local optical properties and the near field of the illuminated sample, changing the field scattered by the tip, denoted as E_{sca} , as shown in Fig. 2.1. By recording this tip-scattered field and suppressing background scattering — which mainly arises from the incident light scattering at the sample surface, the tip shaft, and the cantilever — optical images with sub-wavelength spatial resolution can be achieved. This spatial resolution is typically on the order of

the radius of the tip apex and independent of the wavelength of the light [127, 128]. The methods for suppressing background scattering, critical for isolating the near-field scattering by the tip, will be discussed further. The tip-scattered field, resulting from the tip-sample near-field interaction, is the useful signal collected in s-SNOM and will be referred to as the near-field signal.

In this thesis, we used two operational modes of s-SNOM: nanoimaging and nano-FTIR spectroscopy, each defined by its laser source. In nanoimaging, a monochromatic laser is used, enabling the capture of high-resolution images at the nanoscale. On the other hand, nano-FTIR spectroscopy employs a broadband laser, enabling us to measure mid-infrared (mid-IR) spectra (nano-FTIR spectra) and extending the functionality of s-SNOM beyond nanoimaging.

Background suppression

In s-SNOM, a critical challenge is the suppression of background scattering (background signal) that overshadows the useful near-field signal. The background signal, mainly originating from the scattering of the incident field at the sample surface, the tip shaft, and the cantilever, is significantly larger than the near-field signal. This is because the focus size of the incoming light is much larger than the tip apex, illuminating these additional areas.

The tip-scattered field, E_{sca} , can be represented as sum of the background field, E_{bg} , and the useful tip-scattered near field, E_{nf} :

$$E_{\text{sca}} = E_{\text{bg}} + E_{\text{nf}}. \quad (2.1)$$

The detector measures field intensity, and thus the detected intensity is given by:

$$\begin{aligned} I_{\text{photodetector}} \propto |E_{\text{sca}}|^2 &= |E_{\text{bg}} + E_{\text{nf}}|^2 = \\ &= (E_{\text{bg}} + E_{\text{nf}})(E_{\text{bg}} + E_{\text{nf}})^* = \\ &= E_{\text{bg}}^2 + E_{\text{nf}}^2 + E_{\text{bg}}E_{\text{nf}}^* + E_{\text{nf}}E_{\text{bg}}^*. \end{aligned} \quad (2.2)$$

Eq. 2.2 illustrates that the background significantly impacts the detector signal, both additively and multiplicatively. To fully suppress these background contributions, a combination of higher harmonic demodulation and interferometric detection is employed.

Before discussing the techniques for full-background suppression in s-SNOM nanoimaging and nano-FTIR spectroscopy, it is important to understand the higher harmonic demodulation technique, which plays a crucial role in background suppression. This technique relies on demodulating the detector signal at higher harmonic frequencies of the tip-oscillation frequency, Ω_{tip} (Fig. 2.1). The tip-scattered near field exhibits a strong nonlinear dependence on the tip-sample distance due to the exponential decay of the near

field beneath the tip apex. The tip-scattered field is large when the tip is at the sample surface, but almost zero at larger tip-sample distances. Because of this strong nonlinear dependence, signals at higher harmonics are obtained. In contrast, the background field changes less nonlinearly with the tip-sample distance, as it varies at the wavelength scale of the incident light. Consequently, the contribution of the background to higher harmonics is minimal. Therefore, by demodulating detector signal at higher harmonics, $n\Omega_{\text{tip}}$, with $n > 2$ being an integer, we essentially measure the tip-scattered near field and thus suppress the background.

In *s-SNOM nanoimaging*, the combination of higher harmonic demodulation and pseudo-heterodyne interferometric techniques is utilized for the background-free detection of the amplitude- and phase-resolved near-field signal [129, 130]. The pseudo-heterodyne scheme is based on a Michelson interferometer (illustrated on the left side in Fig. 2.2). The incoming light is split into two beams by a beamsplitter (BS). The reference beam is reflected at a reference mirror (RM_1) and the illumination beam is scattered at the AFM tip oscillating at frequency Ω_{tip} . At the detector, the light backscattered from the tip interferes with the backreflected reference beam. Importantly, the reference mirror, RM_1 , oscillates along the beam axis with an oscillation amplitude Δl and an oscillation frequency M (typically $M \approx 300$ Hz), leading to a phase modulation of the reference beam and subsequently to detector signal sidebands at frequencies $n\Omega_{\text{tip}} \pm mM$, where m is an integer value. The demodulation and analysis of the tip-scattered light at $n\Omega_{\text{tip}} \pm M$ and $n\Omega_{\text{tip}} \pm 2M$ yield background-free amplitude- and phase-resolved near-field signal (complex-valued near-field signal), typically for $n > 2$ [129, 130].

In *Nano-FTIR spectroscopy*, a Michelson interferometer (illustrated on the right side in Fig. 2.2) is utilized to record near-field interferograms, that is, the n -th order demodulated detector signal is recorded as a function of the position of the reference mirror (RM_2) that is linearly translated. The recorded interferograms are Fourier transformed (FT) to obtain nano-FTIR spectra. Since the tip is located in one of the interferometer arms, the FT yields both amplitude and phase spectra. Note that the multiplicative background manifests as a complex-valued offset to the interferograms, thus nano-FTIR spectra are free from multiplicative background for spectral frequencies larger than zero [131–134].

In summary, the combination of higher harmonic demodulation with interferometric detection plays a crucial role in s-SNOM nanoimaging and nano-FTIR spectroscopy, effectively suppressing background signal thereby ensuring the accuracy and clarity of the nanoscale imaging and spectroscopy. Importantly, interferometric detection facilitates the retrieval of complex-valued (amplitude and phase-resolved) near-field signal:

$$\sigma_n = s_n e^{i\varphi_n} \propto E_{\text{nf},n}, \quad (2.3)$$

where n denotes the demodulation order, s_n and φ_n are the amplitude and phase compo-

nents of the near-field signal, respectively.

2.1.2 Setup for s-SNOM and nano-FTIR spectroscopy

In this thesis, a commercial s-SNOM system (neaSNOM, Attocube AG) is used for infrared nanoimaging and nano-FTIR spectroscopy. The system includes a tunable quantum cascade laser (QCL) from Daylight Solutions for s-SNOM imaging, and a broadband infrared laser continuum, generated by difference frequency generation (DFG), for nano-FTIR spectroscopy. A parabolic mirror (PM) is used to focus these lasers on the tip of an atomic force microscope (AFM). Standard platinum-coated AFM tips (NCPt arrow tip from Nanoworld) with an apex radius of about 25 nm are used. The light that is backscattered from the AFM tip is collected by the same parabolic mirror. It is then detected by one of two asymmetric Michelson interferometers; one is designated for s-SNOM nanoimaging (left side of the setup) and the other for nano-FTIR spectroscopy (right side of the setup). In the asymmetric Michelson interferometer, the sample is placed in one of the interferometer arms (below the AFM tip), which allows for the measurement of amplitude and phase of the tip-scattered light, as it is discussed in Section 2.1.1. In both interferometers, an HgCdTe (MCT) infrared detector cooled by liquid nitrogen is utilized.

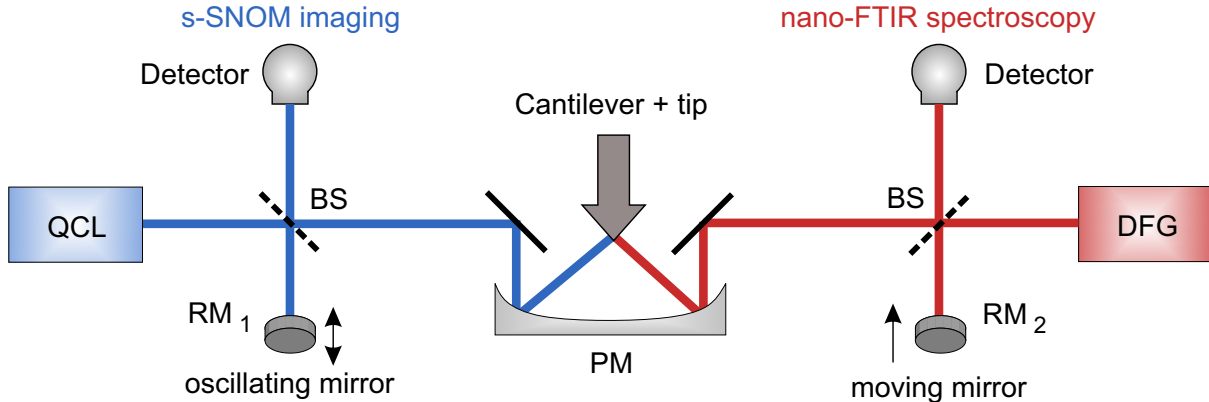


Figure 2.2: s-SNOM and nano-FTIR setup. Quantum cascade laser (QCL) being used for mid-IR s-SNOM imaging and an IR laser continuum based on difference frequency generation (DFG) being used for nano-FTIR spectroscopy. The laser radiation is focused onto the apex of a metallized AFM tip using a parabolic mirror (PM). This tip is in contact (tapping mode) with a sample (which is not shown in the figure). The same PM collects the light scattered from the tip. For detection, two distinct asymmetric Michelson interferometers are used, each consisting of a beam splitter (BS), a movable reference mirror (RM), and an infrared detector. In nano-FTIR spectroscopy, the reference mirror RM_2 moves linearly along the axis of the beam. In s-SNOM imaging, the reference mirror RM_1 oscillates at a frequency M with an oscillation amplitude Δl .

2.1.3 Imaging of ultra-confined polaritons (polariton interferometry)

s-SNOM is a highly effective tool for imaging ultra-confined polaritons, especially in thin layers of vdW materials [19, 20, 22, 52, 53]. The commonly used technique for imaging polaritons is known as polariton interferometry. The key of polariton interferometry lies in the ability of a metallic tip to efficiently launch propagating polaritonic modes, thanks to the confined hotspot at the tip apex. The confined hotspot provides the necessary momentum to radially launch a polariton mode that propagates outward from the tip, as illustrated in Fig. 2.3a. Sample edges act as a reflector of the propagating polariton mode, directing it back towards the tip where the electric field of the polariton mode, E_p , contributes to the tip-scattered light, E_{sca} . By scanning the tip towards the sample edge along the x -axis (perpendicular to the sample edge, see Fig. 2.3a), the amplitude and phase of the tip-scattered near field exhibit decaying oscillations (commonly referred to as ‘fringes’) with a periodicity of half the polariton wavelength, as shown in Fig. 2.3b. A more detailed discussion about polariton interferometry is presented in the following subsection *Complex representation and Fourier transform analysis of polariton interferometry experiments* on page 23. It is noteworthy that this polariton imaging technique is similar to the echolocation method used by bats.

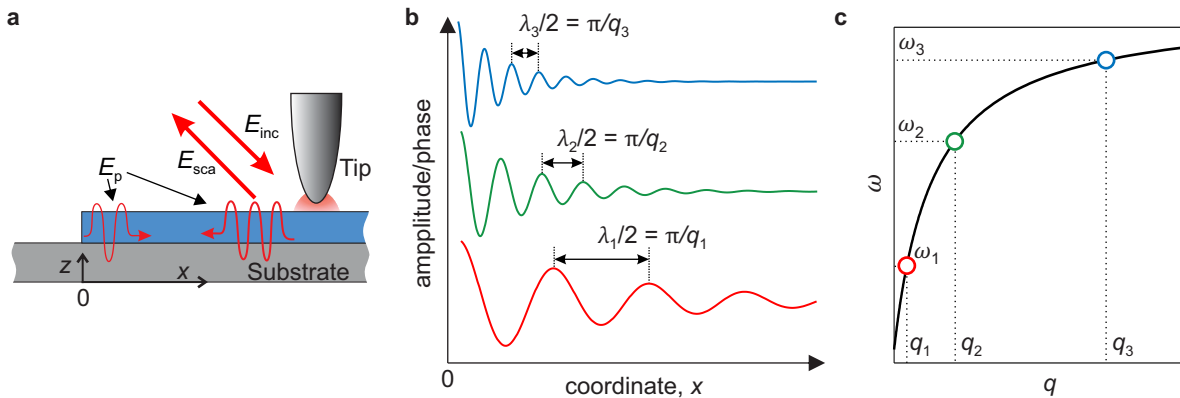


Figure 2.3: Polariton interferometry. **a**, Illustration of the polariton interferometry experiment. E_{inc} , E_{sca} and E_p denote the electric fields of the incident, tip-scattered and polariton mode field, respectively. **b**, Illustration of the amplitude (phase) of the tip-scattered near field as a function of the tip-edge distance (x coordinate) at three different frequencies, which are indicated on the dispersion curve in **c**. **c**, Illustration of the dispersion relation. Red, green, and blue circles indicate the frequencies at which the polariton interferometry experiments, shown in **b**, are illustrated.

Polariton interferometry is an important technique for exploring the polariton dispersion relationship, which connects their frequency (energy) and momentum (wavevector), essential for describing and understanding light-matter interaction. The idea of extracting the dispersion is that the decaying oscillations (fringes) contain the full information about

the complex-valued polariton momentum, $q_{p,c} = q_p + i\kappa_p$, where the real component is connected with the polariton wavelength, $q_p = 2\pi/\lambda_p$, and the imaginary component, κ_p , defines the amplitude decay of the polariton mode. Two typical methods are employed to extract the complex-valued polariton momentum from these fringes. The first approach involves fitting the fringes in real space with a decaying sinusoidal function, whereas the second approach involves analyzing these fringes in reciprocal space by performing a Fourier Transform (FT) of them. It's important to note that the FT of a complex decaying wave, which is a simple model for the fringes, has a straightforward analytical solution, as will be discussed in the subsection *Fourier transform of the complex decaying wave* on page 26. By performing polariton interferometry and extracting the polariton wavelength and decay at different frequencies, we can reconstruct the entire polariton dispersion, see Fig. 2.3c. This technique enables the real-space mapping of ultra-confined polaritons and the measurement of their dispersion, which is key to unlocking insights into nanoscale light-matter interactions.

Complex representation and Fourier transform analysis of polariton interferometry experiments

To explain and discuss the basics of polariton interferometry experiments, we particularly aim to explain the presence of decaying oscillations (fringes) in the amplitude and phase components of the tip-scattered near field. We begin by representing the tip-scattered field of the propagating polariton mode in the form of complex-valued decaying wave, $E_p(x) = A_c e^{iq_{p,c}2x}$, where A_c and $q_{p,c} = q_p + i\kappa_p$ are the complex-valued amplitude and polariton momentum, respectively. Here, x represents the distance between tip and edge (see Fig. 2.3a). For simplicity, and without loss of generality, we neglect the radial excitation of polariton waves, noting that this only influences the spatial decay of polaritons and the imaginary component of the polariton momentum.

The tip-scattered field, E_{sca} , originally defined in Eq. 2.1, requires modification to include the additional contribution from E_p , and is thus expressed as:

$$E_{sca} = E_{bg} + E_{nf} + E_p. \quad (2.4)$$

The polariton modes are confined to the interfaces between the polaritonic vdW material and a medium with positive dielectric function (as discussed in Section 1.2 and illustrated in Fig. 1.3). This confinement means that the field of the polariton mode exponentially decays along the z -axis, and thus E_p will not be suppressed by background suppression techniques. We note that E_p can be approximated as $E_p \propto e^{-q_p z}$ in the quasistatic limit when $q_0 \ll q_p$, where q_0 is the momentum of a free-space photon, with the condition that $z > 0$, where $z = 0$ represents the top interface of the polaritonic vdW material. As a result, after background suppression (details of which were previously discussed in the

subsection *Background Suppression* on page 19), the complex-valued demodulated near-field signal can be approximated as the sum of the demodulated tip-scattered near field and the polariton field:

$$\sigma_n(x) = s_n e^{i\varphi_n} \propto E_{\text{nf},n} + E_{\text{p},n}(x), \quad (2.5)$$

where n denotes the demodulation order, s_n and φ_n represent the amplitude and phase components of the near-field signal, respectively. Eq. 2.5 demonstrates how the tip-scattered polariton field manifests in the demodulated near field signal, which is generated in the s-SNOM microscope.

For further discussion of polariton interferometry experiments, we simplify the notation by omitting the indices of demodulation order. We assume that the near-field signal is proportional to the sum of the tip-scattered near field, E_{nf} , and the polariton field, $E_{\text{p}}(x)$, as shown in Eq 2.5. We further refer to this sum as the total tip-scattered near field, E_{t} , given by:

$$E_{\text{t}}(x) = E_{\text{nf}} + E_{\text{p}}(x) = E_{\text{nf}} + A e^{i\phi} e^{iq_{\text{p},c}2x}, \quad (2.6)$$

where we replace the complex-valued A_c with $A e^{i\phi}$, where A and ϕ are the initial real-valued amplitude and phase components, respectively. Notice, that E_{nf} represents a constant complex-valued offset field and can be expressed as $E_{\text{nf}} = a_{\text{off}} + ib_{\text{off}} = s_{\text{off}} e^{i\varphi_{\text{off}}}$.

The red curve in Fig. 2.4a illustrates the typical line profile of $E_{\text{t}}(x)$ as a parametric function of the tip-edge distance, x , plotted on the complex plane, assuming a large s_{off} , $\phi = 0.6\pi$ and moderate damping κ_{p} . The line profile of $E_{\text{t}}(x)$ forms a spiral on the complex plane with a shifted center due to E_{nf} . Fig. 2.4d-g show the real component, imaginary component, amplitude, and phase of the E_{t} line profile as a function of x showcasing decaying oscillations with a periodicity of half-polariton wavelength, $\lambda_{\text{p}}/2$. We note that these decaying oscillations not centered around zero but offset by corresponding values: real part around a_{off} , imaginary around b_{off} , amplitude around s_{off} , and phase around φ_{off} . The FT of these decaying oscillations results in a peak function with the peak position at $2q_{\text{p}}$, confirming the oscillatory behavior with the same real-valued momentum $2q_{\text{p}} = 4\pi/\lambda_{\text{p}}$ (see right panels in Fig. 2.4d-g). However, in cases of large spatial damping κ_{p} a complex-valued analysis of the line profile becomes essential for accurately extracting the complex-valued momentum [21, 124]. The reason for this is the presence of only one or fewer oscillations in both the amplitude and phase line profiles.

To illustrate how the small field offset s_{off} and $\phi = -0.9\pi$ affect the amplitude and phase of the line profile, we introduce a line profile which consist of the polariton field with a small field offset. This line profile is shown by the grey spiral in Fig. 2.4a. The amplitude and phase of this line profile (shown by grey curves in Fig. 2.4b,c, respectively) demonstrate nonlinear behavior, deviating from the decaying oscillations previously observed in the amplitude and phase of E_{t} line profile with the large field offset shown in Fig. 2.4f,g.

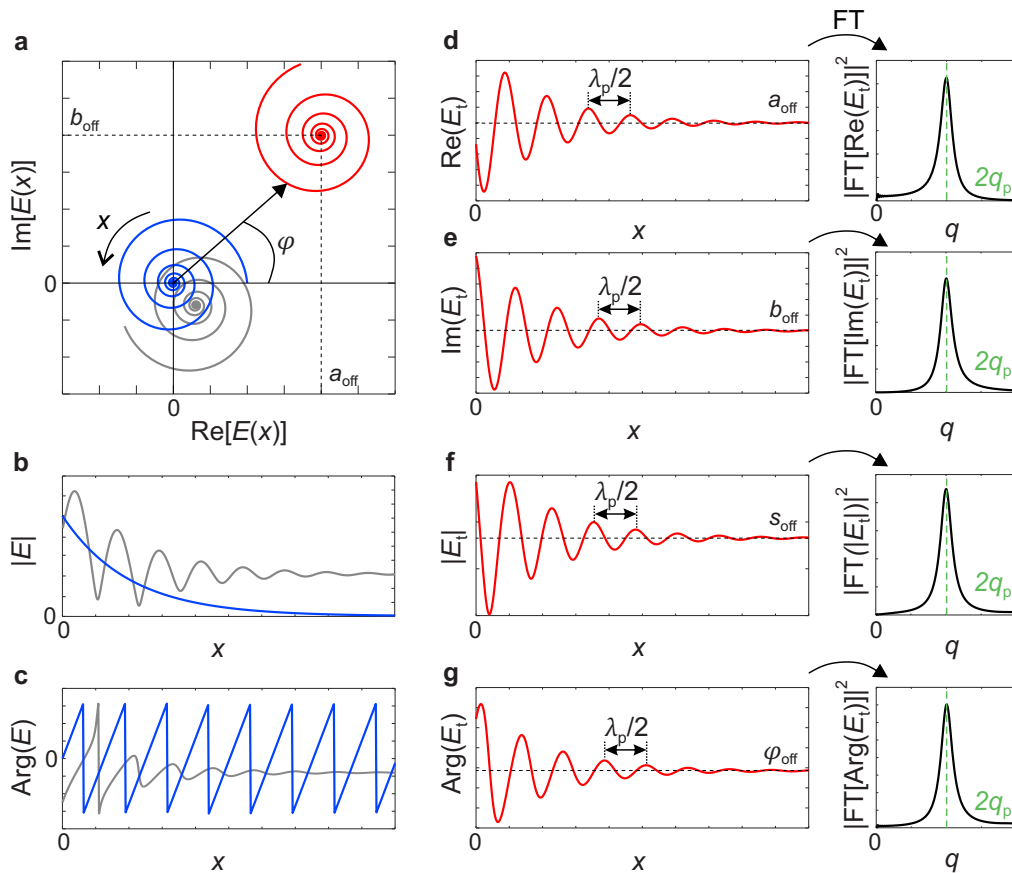


Figure 2.4: Complex representation. **a**, Representation of polariton interferometry line profiles on the complex plane: the blue curve for the offset-free line profile, the grey curve for a line profile with a small complex-valued offset, and the red curve for a line profile with a large complex-valued offset. **b,c**, Blue and grey curves show the amplitude and phase components of the line profiles shown by blue and grey in panel **a**, respectively. **d,e**, Real and imaginary components of line profile with large complex-valued offset (red spiral in panel **a**), respectively. **f,g**, Amplitude and phase components of the line profile with large complex-valued offset (red spiral in panel **a**), respectively. **d-g** Right panels show the corresponding Fourier transforms of the line profiles shown on the left panels, respectively.

By removing E_{nf} , we refine the total tip-scattered near field to exclusively represent the tip-scattered field of the polariton mode:

$$E_t^*(x) = E_p(x) = A_c e^{i2q_p \cdot x} = A e^{-2\kappa_p x} e^{i(\phi + 2q_p x)}. \quad (2.7)$$

Removing E_{nf} facilitates the distinct separation of the momentum's imaginary and real components into the amplitude and phase components of the line profile, respectively:

$$\begin{aligned} |E_t^*(x)| &= |E_p(x)| = A e^{-2\kappa_p x}, \\ \text{Arg}[E_t^*(x)] &= \text{Arg}[E_p(x)] = \phi + 2q_p x. \end{aligned} \quad (2.8)$$

The blue spiral shown in Fig. 2.4a illustrates the line profile of $E_p(x)$ with $\phi = 0$. The amplitude and phase components of this profile are represented by the blue curves in Fig. 2.4b,c, respectively. Specifically, the amplitude component exhibits only an expo-

ponential decay characterized by 2κ , whereas the phase component exhibits a linear growth with the derivative $2q_p$, as demonstrated by Eq 2.8. As a result, the approach of removing the complex-valued offset enables the quick and straightforward extraction of the complex-valued polariton momentum [124].

In summary, the analysis of polariton interferometry experiments should incorporate complex data, particularly in case of the high damping [21, 124]. Nevertheless, in situations involving large complex-valued offsets, which are common with vdW materials, the analysis of polariton wavelength (polariton dispersion) can also be effectively done using only solely amplitude or phase near-field line profiles, such as we performed in Section 3.4 of Chapter 3.

Fourier transform of the complex decaying wave

The Fourier transform (FT) of the complex-valued line profiles in polariton interferometry experiments represents a robust method for filtering the polariton field and extracting the complex polariton momentum, $q_{p,c}$ [22, 135]. We employed numerical FT of the complex-valued nano-FTIR line profiles in Section 3.3 of Chapter 3 for analyses of the phonon polariton dispersion and also for filtering the phonon polariton field (see details in subsections *Fourier Transform of the nano-FTIR Linescans* and *Inverse Fourier Transform of the Isolated M0 Mode* on pages 53 and 54, respectively), whereas in Section 3.4 of Chapter 3 we performed FT of the amplitude line profiles (see details in subsection *Fourier Transform of the Line Profiles of Fig. 3.3* on page 56). We note that the use of only amplitude line profiles is justified by the moderate damping and large offset (see discussion in *Complex Representation and Fourier Transform Analysis of Polariton Interferometry Experiments* on page 2.1.3). In the polariton interferometry experiments, the tip-scattered field of the polariton mode can be modeled by the complex-valued decaying wave, $E_p(x) = A_c e^{iq_{p,c}2x}$. For the sake of general discussion, here we aim to briefly explore a simple and useful example of the FT of an arbitrary complex-valued decaying wave, which can be analytically derived.

The arbitrary complex decaying wave, propagating along the x -axis, can be expressed as:

$$f(x) = A e^{i\phi} e^{-iq_{p,c}x} u(x) = A e^{i\phi} e^{i(q_p + i\kappa_p)x} u(x) = A e^{i\phi} e^{-\kappa_p x} e^{iq_p x} u(x), \quad (2.9)$$

where A and ϕ represent the real-valued initial amplitude and phase, respectively. The term q_c is a complex-valued momentum, given by $q_{p,c} = q_p + i\kappa_p$, where q_p and κ_p are its real and imaginary components, respectively. To limit the analysis to a specific region, we multiply the Heaviside step function $u(x)$ to $f(x)$, which is defined as:

$$\begin{aligned} u(x) &= 1, \quad x \geq 0 \\ u(x) &= 0, \quad x < 0. \end{aligned} \quad (2.10)$$

The Fourier transform of the function $f(x)$ is given by:

$$\tilde{f}(q) = e^{i\phi} \int_{-\infty}^{\infty} f(x) e^{-iqx} dx = \frac{Ae^{i\phi}}{i(q - q_p) + \kappa_p}. \quad (2.11)$$

It can be observed from Eq. 2.11 that the amplitude of $\tilde{f}(q)$ exhibits a peak at q_p with a FWHM of $\sqrt{3} \cdot 2\kappa_p$.

The square of the $\tilde{f}(q)$ is described by a Lorentzian peak function:

$$|\tilde{f}(q)|^2 = \frac{A^2}{(q - q_p)^2 + \kappa_p^2} = \frac{A^2}{(q - q_p)^2 + (\frac{\kappa_p^*}{2})^2} \propto L(q, q_p, \kappa_p^*), \quad (2.12)$$

where q_p is the peak position of $|\tilde{f}(q)|^2$ and $\kappa_p^* = 2\kappa_p$ represents a FWHM of $|\tilde{f}(q)|^2$.

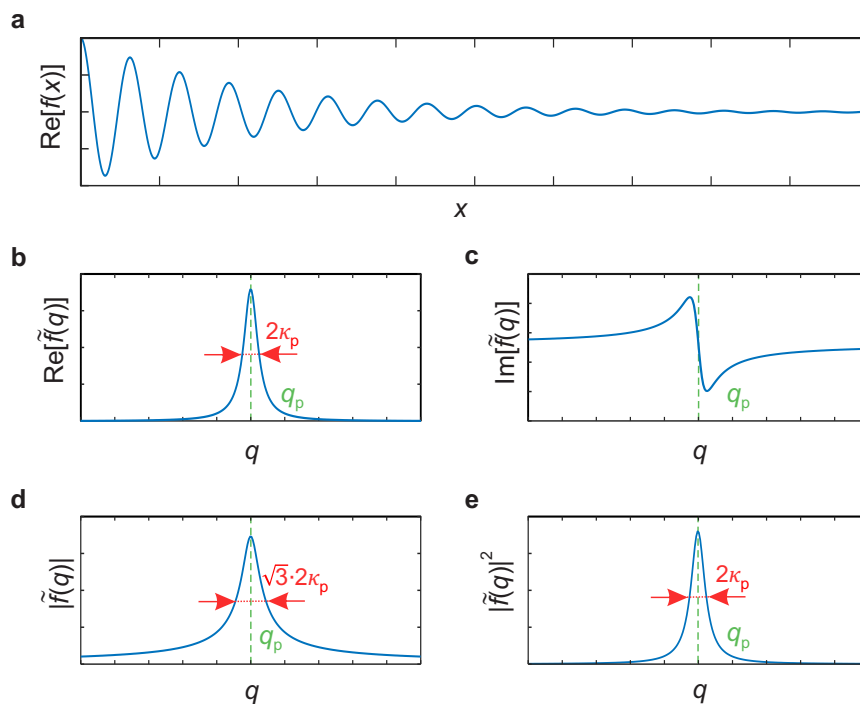


Figure 2.5: Illustrative example of FT of the complex decaying wave. **a**, Real part of $f(x)$ with $\phi = 0$. **b-d**, Real, imaginary, and amplitude components of $\tilde{f}(q)$, where $\tilde{f}(x)$ is the Fourier Transform (FT) of $f(x)$. **e**, The square of the amplitude of $\tilde{f}(x)$.

For illustrative purposes, the FT of the complex decaying wave, $f(x)$, assuming $\phi = 0$, was performed. Fig. 2.5a displays the real part of this wave. Figs. 2.5b-d illustrate the real part, imaginary part, and amplitude of $\tilde{f}(q)$, respectively. Fig. 2.5d demonstrates that the square of $\tilde{f}(q)$ is characterized by a Lorentzian peak function, $L(q, q_p, \kappa_p^*)$, with the FWHM $= 2\kappa_p = \kappa_p^*$. The amplitude $|\tilde{f}(q)|$ yields a peak with the FWHM $= \sqrt{3} \cdot 2\kappa_p = \sqrt{3}\kappa_p^*$. It is important to note that the shapes of $\text{Re}[\tilde{f}(q)]$ and $\text{Im}[\tilde{f}(q)]$ functions depend on ϕ , and only when $\phi = 0$ the real part of $\tilde{f}(q)$ represented by a symmetric Lorentzian peak function with the same FWHM $= 2\kappa_p = \kappa_p^*$ as the square of $\tilde{f}(q)$.

2.2 Two-coupled harmonic oscillators model

Two-coupled harmonic oscillators represent a simple theoretical model used for analyzing the interaction between light and matter [1, 136]. This model simplifies the understanding and interpretation of experimental data through the concept of harmonic oscillators, facilitating the analysis of light-matter interactions. It is particularly useful for clarifying and explaining the concepts of weakly and strongly coupled systems. In this model, the interacting entities are modeled as harmonic oscillators that are coupled via a coupling strength constant, g . We note that different models are commonly utilized for analysis in the literature [13, 136–138]. In our work, we have used two distinct models to analyze the coupling between polaritons and molecular excitations in Chapters 3 and 4. The specific models and their details will be discussed in more detail in Section 3.4.2 of Chapter 3 and Section 4.5.3 of Chapter 4. Importantly, since our analyses are limited to only the weakly and strongly coupled systems, the two models used in this thesis are essentially equivalent, as demonstrated and discussed in Ref. 139.

Here, we illustrate the model, which describes the interaction between light and matter in a specific manner. It can be shown that in this model, the displacement of one oscillator, $x_1(t)$, is related to the vector potential of the electromagnetic mode, whereas the displacement of the second oscillator, $x_2(t)$, is related to the induced dipole moment, characterizing the optical response of the dipolar matter excitation [139, 140]. The equation of motion of two coupled harmonic oscillators is [138, 141]:

$$\begin{cases} \ddot{x}_1(t) + \Gamma_1 \dot{x}_1(t) + \omega_1^2 x_1(t) - 2g\dot{x}_2(t) = F_1(t) \\ \ddot{x}_2(t) + \Gamma_2 \dot{x}_2(t) + \omega_2^2 x_2(t) + 2g\dot{x}_1(t) = F_2(t) \end{cases} \quad (2.13)$$

where the dots denote the time derivatives. In this model, g denotes the coupling strength, and $x_{1,2}(t)$, $\omega_{1,2}$, $\Gamma_{1,2}$ and $F_{1,2}(t)$ correspond to the displacement, resonance frequencies, linewidths (damping rates) and driving forces of the first and second oscillators, respectively.

The eigenmodes, or quasi-normal modes, are determined from the dispersion relation obtained by setting the determinant of the system in Eq. 2.13 to zero. With the assumption $\omega_j^2 - \omega^2 \approx 2\omega_j(\omega_j - \omega)$, where $j = 1, 2$, the eigenmodes are as follows:

$$\omega_{\pm} + i\frac{\Gamma_{\pm}}{2} = \frac{\omega_2 + \omega_1}{2} - i\frac{\Gamma_2 + \Gamma_1}{4} \pm \frac{1}{2}\sqrt{4g^2 + \left(\omega_2 - \omega_1 - i\frac{\Gamma_2 - \Gamma_1}{2}\right)^2}. \quad (2.14)$$

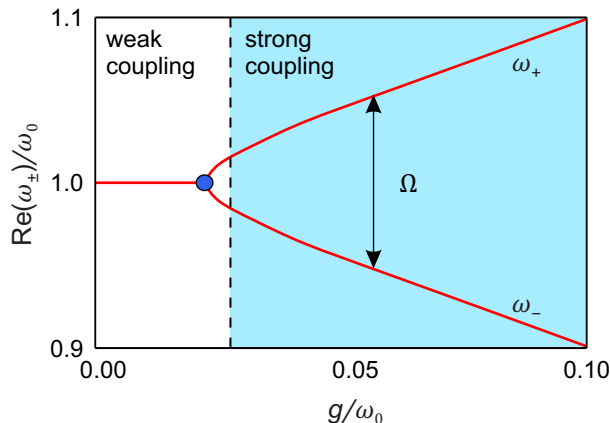


Figure 2.6: Real component of eigenmodes, ω_{\pm} , (Eq. 2.16) as a function of the coupling strength, g . The calculation is performed for two oscillators with the same resonant frequency $\omega_1 = \omega_2 = \omega_0$, and linewidths $\Gamma_1 = 0.1\omega_0$, $\Gamma_2 = 0.01\omega_0$. The blue point marks the point when mode splitting, Ω , becomes real. The vertical dashed black line marks the value $\Omega \approx 2g = (\Gamma_1 + \Gamma_2)/2$. Blue region indicates the strong coupling regime.

The model of two-coupled harmonic oscillators can be employed to determine the coupling strength, g , and the eigenmodes of a coupled electromagnetic system. The conventional approach for determining these parameters involves fitting the optical response of the electromagnetic system with a physical quantity derived from the two-coupled harmonic oscillators model. For instance, the extinction of the electromagnetic system, C_{ext} , can be correlated with the time-averaged power of the external force, $C_{\text{ext}} \propto P_{\text{av}}$ [138]. P_{av} for the coupled oscillators is given by:

$$P_{\text{av}} = \langle F_1(t)x_1(t) + F_2(t)x_2(t) \rangle = \frac{\omega}{2} \text{Im} \left[\frac{(\omega_2^2 - \omega^2 - i\Gamma_2\omega)F_1^2 + (\omega_1^2 - \omega^2 - i\Gamma_1\omega)F_2^2}{(\omega^2 - \omega_1^2 + i\Gamma_1\omega)(\omega^2 - \omega_2^2 + i\Gamma_2\omega) - \omega^2 g^2} \right]. \quad (2.15)$$

By fitting the extinction spectra using Eq. 2.15, one can determine the resonance frequencies ω_1 and ω_2 , as well as the coupling strength g . Then, by substituting these fitting values into Eq. 2.14, it is possible to calculate the eigenmodes ω_{\pm} . In Section 3.4.2 of Chapter 3 and Section 4.5.3 of Chapter 4, a similar fitting procedure is employed to determine the coupling strength and eigenmodes of polaritons coupled with molecular excitations.

Next, we will briefly discuss the behaviour of eigenmodes as a function of the coupling strength and a criterion typically used to distinguish between weak and strong light-matter interaction. At zero detuning, when $\omega_1 = \omega_2 = \omega_0$, Eq. 2.14 simplifies to:

$$\omega_{\pm} + i\frac{\Gamma_{\pm}}{2} = \omega_0 - i\frac{\Gamma_2 + \Gamma_1}{4} \pm \frac{1}{2}\sqrt{4g^2 - \frac{(\Gamma_2 - \Gamma_1)^2}{4}}, \quad (2.16)$$

where $\sqrt{4g^2 - \frac{(\Gamma_2 - \Gamma_1)^2}{4}}$ is often denoted as a mode splitting Ω , also known as Rabi splitting. It is often approximated as $\Omega \approx 2g$. To illustrate the behaviour of the eigenmodes from Eq. 2.16, we plot the $\text{Re}(\omega_{\pm})$ as a function of the coupling strength, g , in Fig. 2.6. The blue point marks the condition when $\sqrt{4g^2 - \frac{(\Gamma_2 - \Gamma_1)^2}{4}} > 0$, and thus the mode splitting becomes real, $\text{Re}(\Omega) > 0$. It is important to note that this condition only leads to the two modes having different real parts of the eigenmodes. However, for the mode splitting to be clearly visible, the difference between the real parts of the eigenmodes must be greater than the sum of the half linewidths of the new eigenmodes, i.e., $\sqrt{4g^2 - \frac{(\Gamma_2 - \Gamma_1)^2}{4}} > \frac{\Gamma_1 + \Gamma_2}{2}$. This leads to the strict strong coupling criterion $4g^2 > \frac{\Gamma_1^2 + \Gamma_2^2}{2}$. Often, this condition is expressed as $2g > \frac{\Gamma_2 + \Gamma_1}{2}$ (blue region in Fig. 2.6); which is equivalent to the previous condition if $\Gamma_1 \approx \Gamma_2$ [1]. This condition can be summarized as "the splitting has to exceed the sum of the half linewidths of the modes" or "the separation of energy levels has to be larger than the sum of their average linewidths".

In summary, the model of two coupled harmonic oscillators offers a simple approach for analyzing light-matter interactions. It enables the straightforward fitting of experimental spectra, like extinction spectra, facilitating the identification of critical parameters necessary for evaluating the strength of light-matter interactions. These parameters typically include the coupling strength, mode splitting and the linewidths of the eigenmodes.

2.3 Quasi-eigenmode analyses using transfer matrix approach

The quasi-eigenmode (eigenmode) analysis of complex continuous layered systems is important for understanding their optical properties and behaviors. The transfer matrix method is as an effective method for this purpose, enabling the precise determination of quasi-eigenmodes by analyzing the poles of reflectivity [23, 142]. In this section, we discuss the principles and application of the transfer matrix method for quasi-eigenmode analysis, which was performed in Chapter 3 and Chapter 4.

The transfer matrix method utilizes a total transfer matrix, \mathbf{T}_N , to connect the electric fields on opposite sides of a layered system (see Fig. 2.7). Specifically, it relates the field on the left side of the first interface, \vec{E}_0^- , to that on the right side of the last interface, \vec{E}_{N+1}^+ , as shown below:

$$\vec{E}_0^- = \mathbf{T}_N \vec{E}_{N+1}^+. \quad (2.17)$$

Here, N is the number of layers in the system, $\vec{E}_i^{-(+)}$ denotes the four-component electric

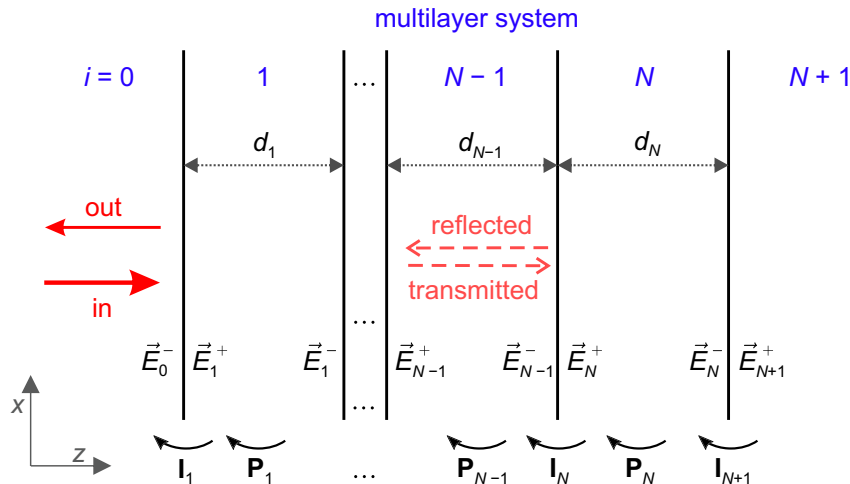


Figure 2.7: Transfer-matrix method. The electric field, \vec{E} , distribution throughout a multilayer system, comprising N layers, can be calculated at any point by starting with \vec{E}_{N+1}^+ . This method requires iterative multiplication by the interface matrices \mathbf{I}_i and propagation matrices \mathbf{P}_i .

field vector at the interface between layer i and $i - 1$, respectively. The vector \vec{E}_i is given by:

$$\vec{E}_i = \begin{pmatrix} E_{\text{trans}}^p \\ E_{\text{refl}}^p \\ E_{\text{trans}}^s \\ E_{\text{refl}}^p \end{pmatrix}, \quad (2.18)$$

where $E_{\text{trans}}^{p(s)}$ and $E_{\text{refl}}^{p(s)}$ represent the in-plane field amplitudes of the transmitted and reflected modes, respectively, for p - and s -polarizations.

The total transfer matrix, \mathbf{T}_N , is constructed by sequentially multiplying the interface matrices, \mathbf{I}_i , with the propagation matrices, \mathbf{P}_i , for each layers:

$$\mathbf{T}_N = \mathbf{I}_1 \mathbf{P}_1 \mathbf{I}_2 \mathbf{P}_2 \dots \mathbf{I}_N \mathbf{P}_N \mathbf{I}_{N+1}. \quad (2.19)$$

The detailed description of the interface matrices, \mathbf{I}_i , and propagation matrices, \mathbf{P}_i , can be found in the original paper 143. Utilizing the total transfer matrix for the entire multilayer system facilitates the precise calculation of reflection and transmission coefficients for both s - and p -polarized light, denoted as r_{ss} , r_{pp} , t_{ss} , and t_{pp} , respectively. Additionally, this framework allows for the determination of mode coupling coefficients, represented as r_{sp} , r_{ps} , t_{sp} , and t_{ps} , with the subscripts indicating the polarization states of incoming and outgoing light. We note that for the analysis of polariton dispersion, we focus on the reflection coefficient for p -polarized light, r_{pp} , which will henceforth be simplified to r_p in following discussions.

Next, the direct connections between the poles of the reflection coefficient, r_p , and the quasi-eigenmodes of the system will be discussed. Mathematically speaking, the reflection coefficient, r_p , represents the solution of the inhomogeneous system of linear equations (when the system includes sources, e.g., a plane wave), where D is the determinant of this system. Reflectivity is inversely proportional to the determinant of the system, $r_p \propto 1/D$, and proportional to the amplitude of the source. In turn, a non-trivial solution of the homogeneous system of linear equations can only exist when its determinant is equal to zero, $D = 0$. Thus, the condition $D = 0$ defines the quasi-eigenmodes. Since the determinant appears in the denominator, $r_p \propto 1/D$, the zeros of the determinant correspond to the poles of r_p and, in turn, correspond to the quasi-eigenmodes. In other words, the reflection coefficient represents the linear response of the system to external excitation. In any linear system, a resonant response indicates the excitation of a mode of the system. Therefore, setting the denominator of reflectivity to zero identifies the pole, which corresponds to the resonant conditions within the system and thus the signature of the quasi-eigenmodes of the system [23, 142].

It is important to note that D is, strictly speaking, an implicit function involving four components [144]: the real and imaginary parts of both the complex-valued momentum, $q_c = q + i\kappa$, and the complex-valued frequency, $\omega_c = \omega - i\gamma$. It is crucial for both κ and γ to be positive, ensuring the electromagnetic field of the mode, which is proportional to $e^{iq_c x - i\omega_c t}$, exhibits decay in both space and time, rather than any form of amplification. Positive values of κ and γ introduce an exponential decay factor along the spatial ($e^{-\kappa x}$) and temporal ($e^{-\gamma t}$) dimensions, respectively. This requirement is crucial for the physical realism of the model, preventing the unphysical growth of the mode in space or time, and aligning with principles of causality and energy conservation.

To facilitate the quasi-eigenmode analysis within the context of four-dimensional space, comprised of the real and imaginary components of both the complex-valued momentum, $q_c = q + i\kappa$, and the complex-valued frequency, $\omega_c = \omega - i\gamma$, it is a common approach to assume that either the frequency or the momentum is real, with the other quantity remaining complex. This analyses typically involve a real-valued frequency (ω) combined with a complex-valued momentum (q_c), or alternatively, a real-valued momentum (q) paired with a complex-valued frequency (ω_c). The framework of a complex-valued frequency is associated with quasinormal modes, which exhibit oscillatory behavior decaying over time with the amplitude time decay constant, γ , whereas a complex-valued momentum relates to propagating modes, characterized by oscillations decaying spatially with the amplitude decay constant, κ (Fig. 2.8f,g) [23, 142]. We note that the one of exemplary experiment for the complex-valued frequency framework involves pulse-probe techniques, enabling observation of the time evolution and decay of the modes, with the entire sample illuminated without concern for the spatial decay of the fields. Conversely, in the complex-valued momentum framework, a light source is utilized to monitor how

modes emanate from the illuminated area and decay in space, such as in the polariton interferometry experiments discussed in Section 2.1.3. This distinction might be critical for understanding and predicting the behavior of different types of modes in complex optical systems.

2.1. Note on propagation length and lifetime definitions

In this thesis, the definitions of the propagation length and lifetime are used in the context of amplitude decay. The propagation length, L , is defined as $L = \kappa^{-1}$, and the lifetime, τ , as $\tau = \gamma^{-1}$. It is important to note that, typically, both propagation length and lifetime are defined in terms of the intensity (power) decay of a signal. Since intensity is proportional to the square of the amplitude, the definitions in the context of intensity decay are given by $L_{\text{int}} = (2\kappa)^{-1}$ and $\tau_{\text{int}} = (2\gamma)^{-1}$ for the propagation length and lifetime, respectively. This distinction arises because the intensity, I , of a wave is related to its amplitude, A , through the relationship $I \propto A^2$. Consequently, when considering intensity decay as opposed to amplitude decay, a factor of 2 difference is observed in the expressions for both the propagation length and lifetime. This difference also explains why the linewidth Γ is connected with γ through the relationship $\Gamma = 2\gamma$. Understanding these distinctions is key to accurately analysing and comparing the propagation lengths and lifetimes.

Note that to calculate the intensity lifetime, denoted $\tau_{\text{int}} = \Gamma^{-1}$, in seconds from the linewidth, Γ , in cm^{-1} the factor 2π should be taken into account according to:

$$\tau_{\text{int}} [\text{s}] = \frac{1}{2\pi\Gamma [\text{cm}^{-1}] c [\text{cm/s}]} \quad (2.20)$$

As an illustrative example, we analyze an optical system that comprises a layer of h-BN above a molecular layer of organic semiconductor (CBP molecules) (see Fig. 2.8a, right sketch), which will be discussed in detail in Chapter 3. Our aim here is to highlight the differences in dispersion that can arise when assuming either complex-valued momentum or complex-valued frequency. We specifically focus on the analysis of the fundamental (M0) PhP mode in the h-BN layer (see discussion about PhP modes in the h-BN on page 10). The blue lines in Fig. 2.8b,c illustrate the PhP dispersion in the h-BN layer surrounded by air (Fig. 2.8a, left image), assuming complex-frequency and complex-momentum formalisms, respectively. We observe that both complex-frequency and complex-momentum formalisms yield the same dispersion for the PhP mode. Incorporating the dielectric layer with a dielectric function equals to the background dielectric

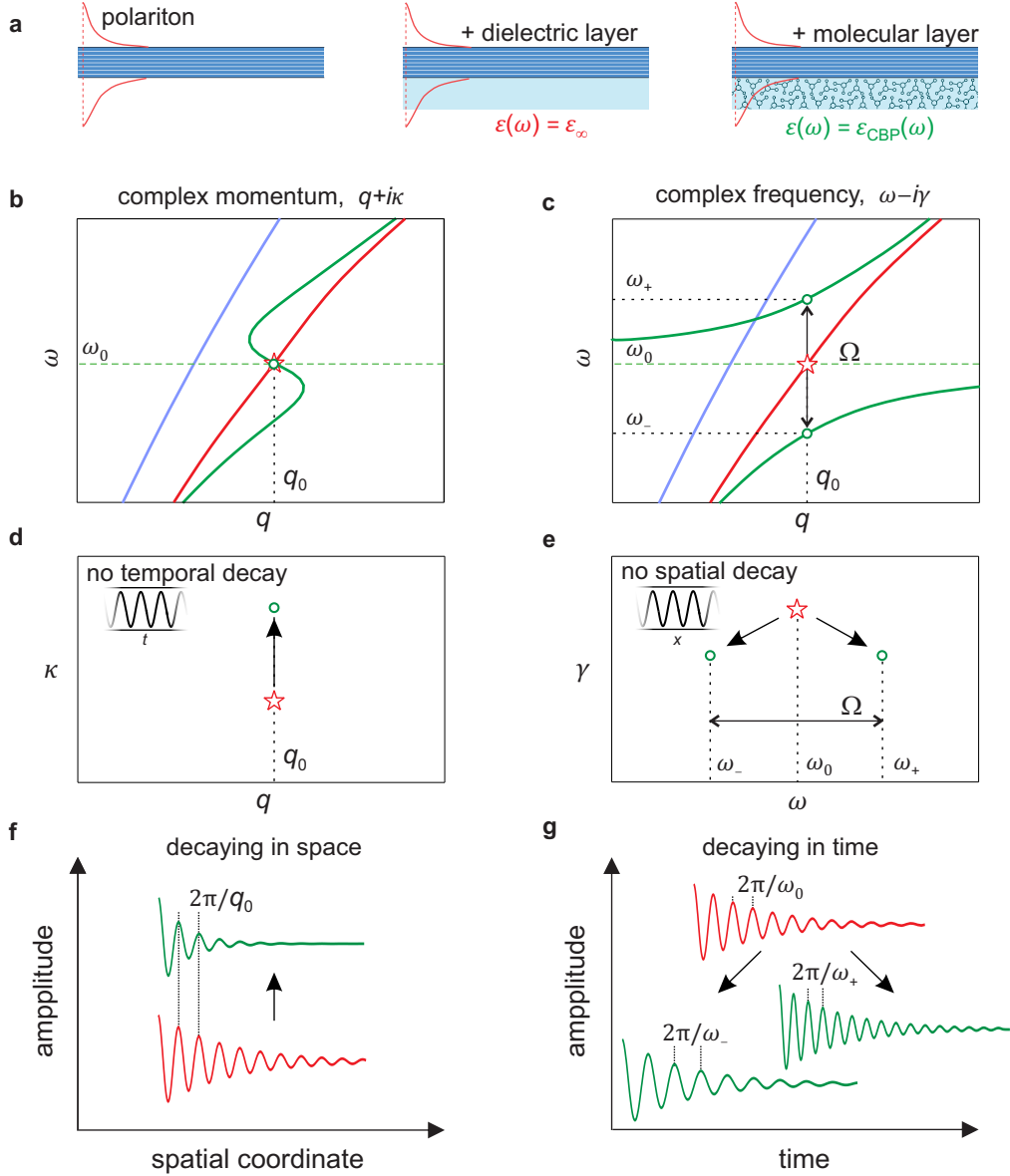


Figure 2.8: Eigenmode analysis. **a**, h-BN layers in different environments: alone in air, on a constant dielectric layer, $\epsilon(\omega) = \epsilon_\infty$, and above a molecular layer with vibrational resonance. Red lines illustrate PhP field decay outside h-BN. **b,c**, Polariton dispersions assuming complex-valued momentum and frequency, respectively. The horizontal green dashed line marks the molecular vibration frequency. Blue and red solid curves represent PhP dispersion in h-BN layer above the air and dielectric layer with $\epsilon(\omega) = \epsilon_\infty$, respectively. Red stars and green circles identify polariton quasi-eigenmodes with and without molecular vibration resonance. **c**, Black arrow indicates mode splitting, Ω . **d**, Red star and green circle show κ with/without molecular vibration resonance. **e**, Red star and green circles shows γ , with black arrow indicating the mode splitting, Ω . **f**, Illustrates spatial oscillation of quasi-eigenmodes marked by red star, green circle from **b,d**, decaying with different κ but propagating with the same q . **d**, Illustrates temporal oscillation of quasi-eigenmodes marked by red star, green circles from **c,e**, decaying with similar γ but oscillating with different ω .

function of CBP molecules $\epsilon(\omega) = \epsilon_\infty$ below the h-BN layer (Fig. 2.8a, middle sketch) also results in identical dispersions in both formalisms (red lines in Fig. 2.8b,c). However, employing the full dielectric function of CBP molecules reveals distinct behaviors in the dispersions: the green curve in Fig. 2.8b (complex-valued momentum) shows back-bending around the molecular vibration frequency (horizontal green dashed line), while the green

curves in Fig. 2.8c (complex-valued frequency) exhibits clear mode splitting (anti-crossing behavior) around this frequency. Furthermore, the presence of the molecular layer notably influences the imaginary part of the quasi-eigenmodes. In the complex-valued momentum formalism, the spatial decay rate of the PhP mode, κ , increases (Fig. 2.8d), indicating smaller decay distance, yet maintaining the same momentum, q_0 (illustrated in Fig. 2.8f). Conversely, in the complex-valued frequency formalism, the time decay rate of the PhP mode, γ , slightly decreases (Fig. 2.8e), indicating slower decay in time. Importantly, new eigenstates emerge at higher, ω_+ , and lower, ω_- , frequencies, indicating oscillation with different periodicity in time (illustrated in Fig. 2.8g).

In conclusion, the distinction between complex-valued frequency and momentum analyses is not only important for understanding of different types of modes in complex optical systems but also plays a crucial role in interpreting experimental results. Specifically, in the context of experimental approaches, the picture of complex frequencies is particularly relevant to spectroscopy and pump-probe experiments [13, 14, 145, 146]. These experiments are designed to observe the characteristics of the system as a function of frequency or time, which are directly linked to the concept of quasinormal modes described by complex frequencies. On the other hand, polariton interferometry experiments (discussed in Section 2.1.3) are more closely aligned with the concept of complex momentum [19, 20, 52]. In these experiments, the spatial propagation and interference patterns of polaritons are key observations, which correspond to the theoretical representation where momentum is treated as a complex quantity. Understanding these nuances might be crucial for correctly interpreting experimental data. Note that in the case of pulses limited in space, both representations can be used [142].

3

Vibrational strong coupling between phonon polaritons and molecules

In this chapter, we demonstrate by near-field nanoimaging techniques (i.e., s-SNOM and nano-FTIR spectroscopy) that vibrational strong coupling (VSC) can be achieved between propagating phonon polaritons (PhPs) in thin vdW crystals (h-BN) and molecular vibrations in adjacent thin molecular layers. We performed polariton interferometry using these near-field techniques, showing that VSC leads to the formation of a propagating hybrid mode with a pronounced anti-crossing region in its dispersion, in which propagation with negative group velocity is found. Numerical calculations support our findings and also predict VSC for nanometer-thin molecular layers and PhPs in few-layer vdW materials, which could make propagating PhPs a promising platform for ultra-sensitive on-chip spectroscopy and future strong coupling experiments.

The results discussed in this chapter have been published in the following paper:
A. Bylinkin *et al.* “Real-space observation of vibrational strong coupling between propagating phonon polaritons and molecules”, *Nat. Photonics* **15**, 197-202 (2021).

3.1 Introduction

Phonon polaritons (PhPs) – light coupled to lattice vibrations – in van der Waals (vdW) crystals open up new possibilities for infrared nanophotonics, owing to their strong infrared field confinement, picosecond-long lifetimes [17, 18, 22, 52, 53, 80, 147] and tunability via thickness and dielectric environment [21, 68, 148, 149]. Since PhPs in many vdW materials spectrally coincide with molecular vibrational resonances, which abound the mid-infrared spectral range, PhPs are thus promising candidates for achieving vibrational strong coupling (VSC) for developing ultrasensitive infrared spectroscopy and modification of chemical reactions by altering the vibrational energy of molecules [4, 118, 150–152]. Indeed, analogously to molecular vibrational infrared spectroscopy employing plasmons in graphene nanoribbons [114], localized PhPs in hexagonal boron nitride (h-BN) high-Q factor nanoresonators were recently coupled to molecular vibrations [13], allowing for ultra-sensitive far-field spectroscopy at the strong coupling limit. However, ultra-confined propagating PhPs in unstructured layers have neither experimentally nor theoretically been explored for field-enhanced molecular vibrational spectroscopy. More generally, none of the ultra-confined propagating polaritons in a 2D material has been exploited so far experimentally for field-enhanced molecular vibrational spectroscopy, although theoretical studies predict intriguing on-chip spectroscopy applications [153]. Further, real-space nanoimaging of the hybrid modes has been elusive, although it is of fundamental importance for in-depth experimental analysis of VSC exploiting PhPs.

Here, we perform mid-infrared nanoimaging experiments [22, 52, 53, 80, 147] as a test bench to study the interaction of ultra-confined propagating polaritons in vdW materials with molecular vibrations in sub-100 nm thick organic layers. Specifically, we perform phonon-polariton interferometry of PhPs in thin continuous h-BN layers interacting with 4,4'-Bis(N-carbazolyl)-1,1'-biphenyl (CBP) molecules. In contrast to typical strong coupling experiments, such as far-field spectroscopy in Kretschmann-Raether configuration or of polariton nanoresonators, we monitor in real space the effect of molecular absorption on PhPs, leading to dramatic modification of the PhP propagation length and anomalous dispersion with negative group velocity. We retrieve - in good agreement - experimentally and theoretically the quasi-normal modes of the CBP-PhP coupled system, revealing significant anti-crossing and mode splitting caused by strong coupling. A numerical study predicts that few-layer h-BN films may enable to reach strong coupling even in the case of atomically thin molecular layers, thus underlining the potential of PhPs to become a platform for ultra-sensitive on-chip spectroscopy devices.

3.2 Sample preparation

To fabricate h-BN/CBP and pure h-BN layers for nanoimaging experiments, we first prepared the Si/SiO₂ substrate, which was partially covered by a molecular layer. For this purpose, thin metallic wires (with a diameter of about 20-30 μm) were placed on top of the Si/SiO₂ substrate. These wires served as a mask during the following molecular evaporation process. Then we evaporated the molecular layer of the required thickness (see Molecular Deposition section below) and removed the wires. Finally, we transferred the thin layers of h-BN (see the h-BN crystals section below) onto the prepared Si/SiO₂/CBP substrate using the deterministic dry transfer technique, ensuring that the layers were positioned to partially lie on the clean areas of the substrate, previously protected by the thin metallic wires, and partially on the regions covered with CBP molecules.

Molecule deposition

4,4'-bis(N-carbazolyl)-1,1'-biphenyl with sublimed quality (99.9%) (Sigma-Aldrich, Saint Louis, MO, USA) was thermally evaporated on top of Si/SiO₂ substrates in an ultra-high vacuum evaporator chamber (base pressure $< 10^{-9}$ mbar), at a rate of 0.1 nm s⁻¹ using a Knudsen cell. Molecule deposition was done by Francesco Calavalle at CIC Nanogune BRTA (Donostia, Spain).

h-BN crystals

The h-BN crystals were grown from a metal flux at atmospheric pressure as described previously [92]. The thin layers used in this study were prepared by mechanical exfoliation with blue Nitto tape. Then we performed a second exfoliation of the h-BN flakes from the tape onto a transparent polydimethylsiloxane stamp. Using optical inspection of the h-BN flakes on the stamp, we identified high-quality flakes with appropriate thickness.

3.3 Hyperspectral phonon polariton interferometry

In Fig. 3.1a we illustrate the polariton interferometry experiment (see details in Section 2.1.3). We illuminate the metallic tip of a scattering-type scanning near-field optical microscope (s-SNOM) to launch PhP modes in a thin hexagonal boron nitride (h-BN) layer, which is placed above a thin layer of CBP molecules. The tip-launched PhPs propagate to the h-BN edge, reflect and propagate back to the tip. The resulting polariton interference is shown in Fig. 3.1b by a numerical simulation of the electric field distribu-

tion along the h-BN/CBP layer. Importantly, the PhP field penetrates into the molecular layer allowing for significant interaction between PhPs and molecular vibrations. By mapping and analyzing the polariton interference spectroscopically, we can study how the molecule-PhP interaction modifies the polariton wavelength λ_{PhP} and propagation length L_{PhP} .

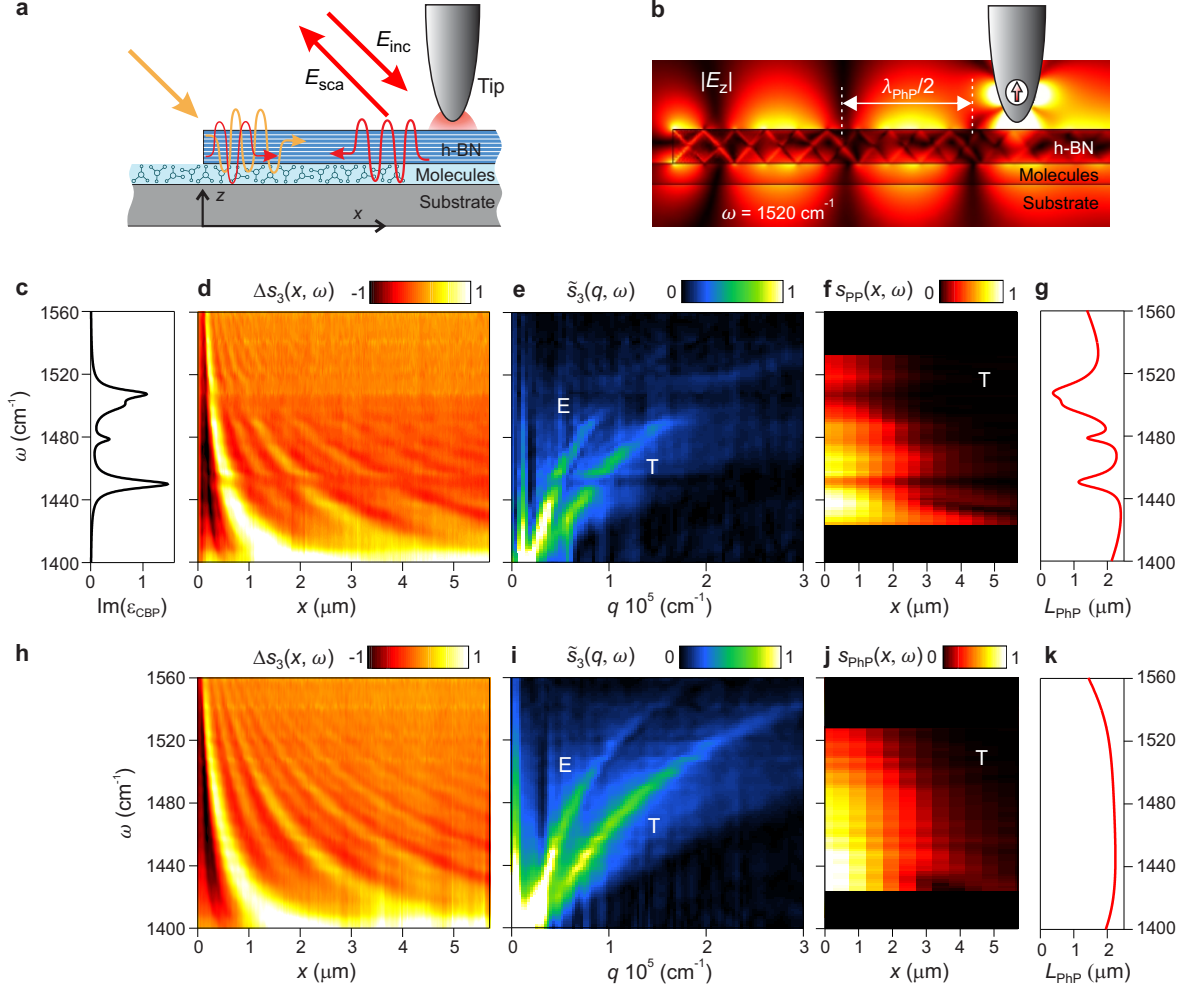


Figure 3.1: Phonon-polariton interferometry of molecular vibrations. **a**, Illustration of the nanoimaging experiment. **b**, Simulated near-field distribution (z -component), generated by a point dipole source (red arrow) mimicking the illuminated tip. Outside the h-BN slab, it reveals essentially the interference of the fundamental PhP slab mode (denoted M0), which is studied in this work. We note the appearance of a zig-zag pattern inside the h-BN slab. It is formed by superposition of higher order slab modes, which are typical for vdW polar crystals [17, 18, 22, 148]. They propagate with significantly larger momenta, and thus do not contribute to the coupling between the M0 mode and the molecular vibrations studied in this work. **c**, Imaginary part of the dielectric function ϵ_{CBP} of CBP molecules **d**, **h**, Baseline-subtracted nano-FTIR amplitude signal $\Delta s_3(x, \omega)$ as a function of tip-edge distance x for h-BN/CBP and pure h-BN layer. **e**, **i**, Amplitude of the Fourier transform of panel **d**, **h** along the x -axis. E and T mark the M0 mode excited by flake edge or tip, respectively. **f**, **j**, Isolated tip-scattered field of the M0 mode, obtained by inverse FT of the filtered T branches (Section 3.7.2). **g**, **k** Theoretical propagation length L_{PhP} of the M0 mode. **b-g**, h-BN thickness is 50 nm, CBP thickness is 40 nm and substrate is 150 nm SiO₂ on Si. **h-k** h-BN thickness is 50 nm and substrate is 150 nm SiO₂ on Si. Note: the spectral resolution was set to 6.25 cm⁻¹, which is the limit of the set-up. The spatial step (pixel) size in the nano-FTIR line scan in **d** is 20 nm, the total scan length is 6 μm and the number of pixels is 300. In **h** the pixel size is 27 nm, the total scan length is 8 μm and the number of pixels is 300.

In a first experiment, we recorded the tip-scattered field E_{sca} (which is governed by the polariton interference) as a function of frequency ω (using the nano-FTIR spectroscopy technique) and distance x between tip and h-BN edge (Fig. 3.1d). We observe the typical signal oscillations (fringes) arising from the polariton interference, whose period $\lambda_{\text{PhP}}/2$ decreases with frequency ω [22]. Importantly, our data reveal interruptions of the fringes (significant reduction of the amplitude signals) at the frequencies of the molecular vibrational resonances, which are absent in the data obtained on h-BN layers without molecules (Fig. 3.1h), clearly indicating significant interaction between PhPs and molecular vibrations.

To visualize the PhP dispersion, we performed a Fourier transform (FT) of the polariton interference pattern along the x -axis, revealing two bright branches in the momentum-frequency, $q-\omega$, domain (Fig. 3.1e and i for h-BN/CBP and pure h-BN layer, respectively, see Section 3.7.2 for data processing details). As in previous experiments [22], both branches (labeled E and T) can be attributed to the fundamental PhP slab mode (typically referred as to M0 mode) launched by either the h-BN edge or the tip, respectively. The E-branch directly reveals the momenta q of the M0 mode, in contrast to the T-branch revealing $2q$, as the M0 mode propagates twice the distance x between edge and tip. We clearly see interruptions at the spectral position of the molecular vibrations, manifesting strong damping of the PhPs by molecular absorption.

The significant interaction between molecular vibrations and PhPs could lead to highly-sensitive and ultra-compact IR spectroscopy devices. To briefly discuss this interesting aspect, we isolate the near-field signal of the tip-launched mode, $s_{\text{PhP}}(x, \omega)$, by filtering and directly reveal PhP attenuation for each frequency ω (Fig. 3.1f, see Section 3.7.2 for data processing details). We observe that the PhPs are less strongly excited and decay faster near the molecular vibrational resonances, demonstrating the possibility of detecting molecular vibrational signatures via the accumulated PhP losses. The numerically calculated propagation lengths of the M0 mode in the presence and absence of the CBP layer (red curves in Fig. 3.1g,k, respectively) corroborate our experimental results qualitatively. We find a reduced propagation length at the CBP absorption bands (e.g. $0.5 \mu\text{m}$ at 1510 cm^{-1}) compared to about $2 \mu\text{m}$ on pure h-BN.

To describe the E- and T-branches observed in the colour plots of $\tilde{s}_3(q, \omega)$ shown in Fig. 3.1i,e, we overlaid our calculated phonon polariton (PhP) dispersion for the fundamental PhP slab mode (M0 mode), $q_{\text{PhP}}(\omega)$. This dispersion was calculated considering complex-valued momenta and real frequencies (see Section 2.3). The overlay, shown in Fig. 3.2, reveals a good match between our calculated PhP dispersion and the observed E- and T-branches in the $\tilde{s}_3(q, \omega)$ data. Both branches correspond to the M0 PhP mode. The E-branch, excited at the h-BN flake edge and propagating once to the tip before scattering, corresponds exactly to our PhP dispersion, with $q_{\text{E}}(\omega) = q_{\text{PhP}}(\omega)$ (purple curves in Fig. 3.2a,b). Conversely, the T-branch, excited by the tip and traveling twice the distance

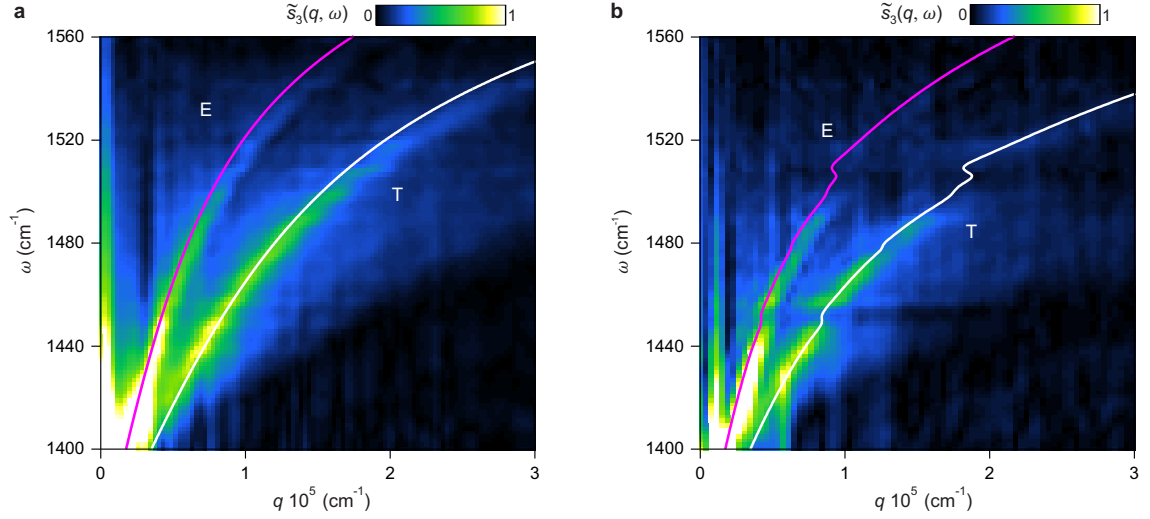


Figure 3.2: Verification of the PhP dispersion. **a,b** Colour plots show the same data as the panels **i,e** of Fig. 3.1. The magenta line shows the calculated PhP dispersion considering complex momenta, $q_E(\omega) = q_{\text{PhP}}(\omega)$, which matches to the E-branch. The white line shows the calculated PhP dispersion with doubled momenta, $q_T(\omega) = 2 \times q_{\text{PhP}}(\omega)$, which matches to the T-branch. Substrate is Si/SiO₂ with 150 nm-thick SiO₂. **a**, Pure 50 nm-thick h-BN flake. **b**, 50 nm-thick h-BN with 40 nm-thick CBP layer below.

between edge and tip, yields doubled PhP momenta, aligning with $q_T(\omega) = 2 \times q_{\text{PhP}}(\omega)$ (the white curves in Fig. 3.2a,b). This direct comparison directly relates the E- and T-branches with the calculated PhP dispersion.

3.4 Quantitative analysis of coupling between phonon polaritons and molecules

3.4.1 Nanoimaging in the region of anomalous dispersion

To quantify the coupling between molecule vibrations and PhPs, we performed a second experiment with improved signal-to-noise ratio and spectral resolution. To that end, we imaged PhPs on a 85 nm thick h-BN layer above a 100 nm thick CBP layer at various frequencies around the CBP vibration at 1450 cm^{-1} employing a quantum cascade laser (QCL). Fig. 3.3a (top panel) shows a representative near-field amplitude image, s_3 , at $\omega = 1460 \text{ cm}^{-1}$. From the images we extracted line profiles in direction perpendicular to the h-BN edge (Fig. 3.3a, bottom), which let us immediately recognize anomalous dispersion [154–157], near the CBP resonance. We clearly see that the PhP wavelength λ_{PhP} increases as the molecular resonance is crossed from 1446 to 1454 cm^{-1} (indicated by black dashed lines in Fig. 3.3a bottom panel).

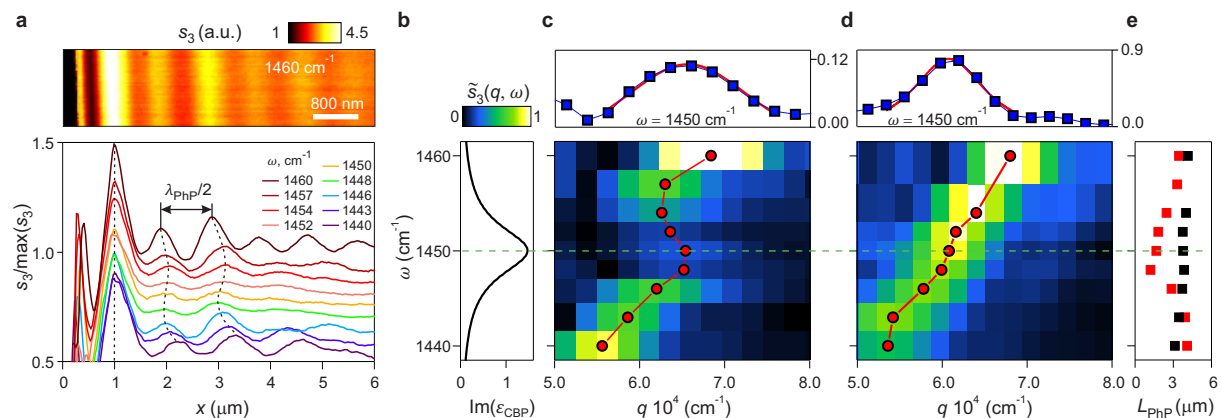


Figure 3.3: Real space imaging of PhPs on a h-BN/CBP layer in the region of anomalous dispersion. **a**, (top panel) Infrared near-field amplitude image of a 85-nm-thick h-BN flake above a 100-nm-thick CBP layer at 1460 cm^{-1} . (bottom panel) Normalized amplitude profile perpendicular to the edge at different frequencies, extracted from images such as the one shown in the top panel. **b**, Imaginary part of the dielectric function ϵ_{CBP} of CBP molecules. **c**, Color plot shows the amplitude of the FT of the line profiles shown in panel **a**. Blue symbols in the top panel show line profile along the dashed horizontal line. Red curve in top panel shows a Lorentzian function fit. Red symbols show the experimental dispersion extracted from the fits in q -direction using Lorentzian function. **e**, Experimental (symbols) and calculated (lines) propagation length L_{PhP} of PhPs on h-BN/CBP (red) and pure h-BN (black) layer. **d**, Analogous to **c** for h-BN layer without CBP molecules.

To analyze the corresponding PhP dispersion, we assembled FTs of the line profiles into a $\tilde{s}_3(q, \omega)$ plot (Fig. 3.3c see Section 3.7.2 for data processing details). By fitting the $\tilde{s}_3(q, \omega)$ in q -direction using Lorentzian function and marking the maxima (red symbols in

Fig. 3.3c), we clearly see that molecular absorption introduces a backbending in the PhP dispersion, in stark contrast to the PhP dispersion observed for h-BN without molecules (Fig. 3.3d, obtained analogously to Fig. 3.3c for pure h-BN layer). Further, the propagation length is significantly reduced by the presence of molecules (red symbols in Fig. 3.3e). Both observations represent a fundamental landmark feature of strong interaction between a propagating mode and a dipolar excitation, here, for the first time, observed in real space for ultra-confined phonon polaritons coupled to molecular vibrations.

3.4.2 Strong coupling analysis

The significant backbending of the dispersion indicates strong coupling between the PhPs and the molecular vibration of CBP, which in the following we corroborate by theoretical quasi-normal mode analysis in the Section 3.4.3. To this end, we extracted $\tilde{s}_3(\omega)$ line profiles from Fig. 3.3a for fixed momenta q and fitted the data with a coupled harmonic oscillators model [13, 136, 138], which was discussed in Section 2.2. The equation of motion for the two coupled harmonic oscillators are given by:

$$\begin{cases} \ddot{x}_{\text{PhP}}(t) + \Gamma_{\text{PhP}}\dot{x}_{\text{PhP}}(t) + \omega_{\text{PhP}}^2 x_{\text{PhP}}(t) - 2g\bar{\omega}x_{\text{CBP}}(t) = F_{\text{PhP}} \\ \ddot{x}_{\text{CBP}}(t) + \Gamma_{\text{CBP}}\dot{x}_{\text{CBP}}(t) + \omega_{\text{CBP}}^2 x_{\text{CBP}}(t) - 2g\bar{\omega}x_{\text{PhP}}(t) = F_{\text{CBP}} \end{cases} \quad (3.1)$$

In the model, we described the PhP mode by x_{PhP} , ω_{PhP} and Γ_{PhP} , which represent the displacement, frequency and linewidth of the PhP mode, respectively. The molecular vibration was described by x_{CBP} , ω_{CBP} and Γ_{CBP} , which represent the displacement, frequency and linewidth of the molecular vibration mode, respectively. F_{PhP} and F_{CBP} represented the effective external forces that drive the motion of oscillators. g represented the coupling strength and $\bar{\omega} = (\omega_{\text{PhP}} + \omega_{\text{CBP}})/2$. The extinction, C_{ext} , of such system can be calculated according to $C_{\text{ext}} \propto \langle F_{\text{PhP}}\dot{x}_{\text{PhP}} + F_{\text{CBP}}\dot{x}_{\text{CBP}} \rangle$ [138].

We fit C_{ext} to the vertical line profiles of $\tilde{s}_3(\omega)$ (line profiles at fixed momentum). In the fitting procedure, $\Gamma_{\text{CBP}} = 6.5 \text{ cm}^{-1}$ and $\Gamma_{\text{PhP}} = 8 \text{ cm}^{-1}$ were fixed according to the CBP dielectric function and eigenmode analysis (considering complex frequencies) of uncoupled PhP in the h-BN, which is separated from Si/SiO₂ substrate by 100 nm spacer (SiO₂ thickness is 150 nm). ω_{CBP} was limited within a few wavenumbers from its initial value ($\omega_{\text{CBP}} = 1450 \text{ cm}^{-1}$), to allow for an eventual Lamb shift of the molecular vibration [158, 159]. ω_{PhP} was considered as free parameters in all fits. The coupling strength g was considered as a free parameter in three fits at $q = (5.86, 6.12, 6.36) \times 10^4 \text{ cm}^{-1}$, which were shown by black curves in Fig. 3.4a. The extracted values of the coupling strength for each fits are plotted as black symbols in the Fig. 3.4b. Dashed black line in Fig. 3.4b indicates the average coupling strength of extracted values, $g_{\text{avg}} = 6.6 \text{ cm}^{-1}$. We fixed the coupling strength to $g = g_{\text{avg}} = 6.6 \text{ cm}^{-1}$ in the fits at $q = (5.62, 6.60) \times 10^4 \text{ cm}^{-1}$,

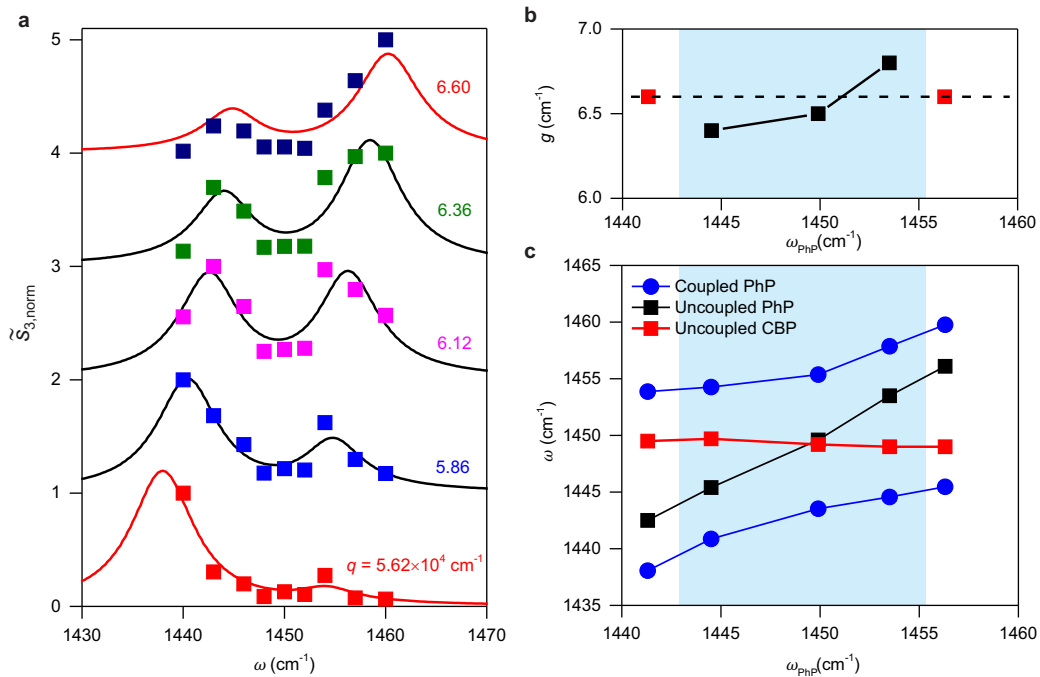


Figure 3.4: Coupled oscillators fit. **a**, Squares are normalized vertical line profiles of amplitude of FT, $\tilde{s}_{3,\text{norm}}(\omega) = \tilde{s}_3(\omega)/\max(\tilde{s}_3(\omega))$, from the Fig. 3.3. Black lines are fit of the coupled oscillators model with coupling strength, g , as a free parameter. Red lines are fit of the coupled oscillators model with fixed coupling, $g_{\text{avg}} = 6.6$. **b**, Black symbols show the coupling strength from the fits, black dashed line indicates the average coupling strength, $g_{\text{avg}} = 6.6$. **c**, Uncoupled frequencies of the PhP, ω_{PhP} , and CBP molecules, ω_{CBP} , as extracted from the fit. **b,c**, Blue region indicates the points of the fits with coupling strength, g , as a free parameter.

which are shown by red curves in Fig. 3.4a. With the parameters extracted from the fits we calculated the quasi-normal modes of the coupled system, according to [160]:

$$\omega_{\pm} + i\frac{\Gamma_{\pm}}{2} = \frac{\omega_{\text{PhP}} + \omega_{\text{CBP}}}{2} - i\frac{\Gamma_{\text{PhP}} + \Gamma_{\text{CBP}}}{4} \pm \frac{1}{2} \sqrt{4g^2 + \left(\omega_{\text{PhP}} - \omega_{\text{CBP}} - i\frac{\Gamma_{\text{PhP}} - \Gamma_{\text{CBP}}}{2} \right)^2}. \quad (3.2)$$

Fig. 3.4c shows the calculated quasi-normal modes ω_{\pm} as a function of ω_{PhP} . We clearly observe a mode splitting of $\Omega = 11 \text{ cm}^{-1}$ at $\omega_{\text{PhP}} = 1450 = \text{cm}^{-1}$ (the smallest vertical separation between real frequencies of the branches). With $\Gamma_{\text{CBP}} = 6.4 \text{ cm}^{-1}$ and $\Gamma_{\text{PhP}} = 8 \text{ cm}^{-1}$, the mathematical condition of strong coupling [1], $C \equiv \frac{\Omega^2}{\left(\frac{\Gamma_{\text{CBP}}^2}{2} + \frac{\Gamma_{\text{PhP}}^2}{2} \right)} = 2.3 > 1$, is fully fulfilled.

3.4.3 Theoretical eigenmode analysis

To interpret the $\tilde{s}_3(q, \omega)$ data shown in Fig. 3.3c,d and to verify the extracted experimental dispersions, we performed a theoretical eigenmode analysis (see Section 2.3). To that end, we calculated the Fresnel reflection coefficient, r_p , of h-BN/CBP and pure h-BN layers on the SiO₂/Si substrate employing the transfer matrix (TM) method [143]. We find that the $\text{Im}(r_p)$ plotted as a function of real q and ω (Fig. 3.5b,c) describes well the experimental data $\tilde{s}_3(q, \omega)$ (Fig. 3.3c,d), particularly peak positions, linewidths and the saddle point at the CBP resonance, demonstrating that spatially Fourier transformed spectral polariton interferometry can be interpreted analogously to momentum- and frequency-resolved surface plasmon resonance spectroscopy employing, for example, the classical Kretschmann-Raether configuration [1, 161–164].

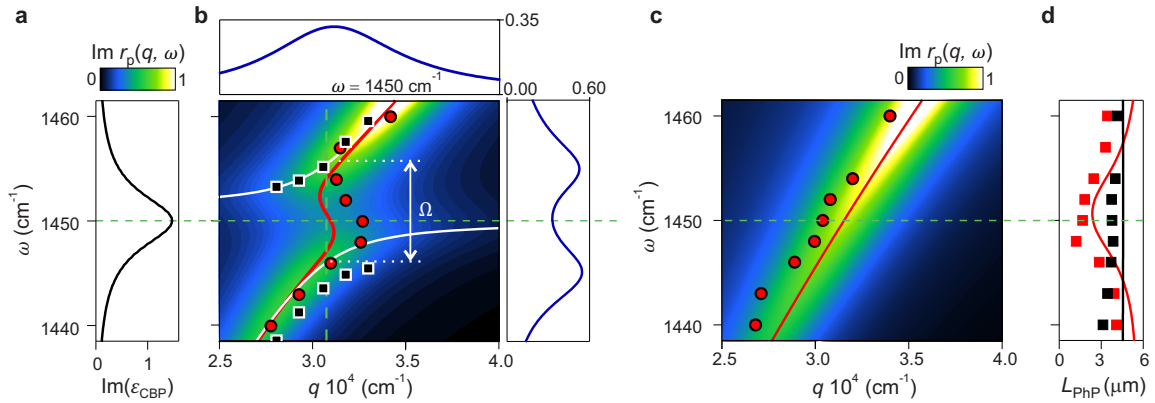


Figure 3.5: Quasi-normal mode analysis. **a**, Imaginary part of the dielectric function ε_{CBP} of CBP molecules. **b**, Color plot shows calculated imaginary part of Fresnel reflection coefficient. Curves inside colour plot show calculated dispersions assuming complex-valued momentum (red) or complex-valued frequency (white). White arrow indicates mode splitting Ω . Black symbols show the quasi-normal modes extracted from coupled oscillators fits in Fig. 3.4. Red symbols show the same experimental dispersion as in Fig. 3.3. Blue curves in the right and top panels show line profiles along the dashed vertical and horizontal lines, respectively. **c**, Analogous to **b** for h-BN layer without CBP.

To obtain the eigenmode dispersions, we determined the poles of r_p , assuming either complex momenta $q + i\kappa$ (corresponding to spatially decaying modes with propagation length $L_{\text{PhP}} = 1/\kappa$) or complex frequencies $\omega - i\gamma$ (corresponding to temporally decaying modes with lifetime $\tau = 1/\gamma$). For spatially decaying modes in h-BN/CBP layers, we find a continuous dispersion exhibiting backbending (compare red curve in Fig. 3.5b with red curve in Fig. 3.5d showing results for pure h-BN layer) and reduced propagation lengths L_{PhP} around the CBP resonance (compare red curve in Fig. 3.5c with black curve showing L_{PhP} for pure h-BN layer). In contrast, analysis of temporally decaying modes yields quasi-normal modes featuring anti-crossing (white curves in Fig. 3.5b) and mode splitting of $\Omega = 10 \text{ cm}^{-1}$, which according to $C = 1.9$ indicates strong coupling. The good agreement between experimental dispersions and propagation lengths (solid lines vs. symbols in Fig. 3.5b and Fig. 3.5c) clearly demonstrates the unique capability of polariton

interferometry for comprehensive and quantitative analysis of the coupling between ultra-confined propagating polaritons and dipolar excitations, here specifically revealing strong coupling between propagating phonon polaritons and molecular vibrations.

3.5 Influence of layer thickness on coupling

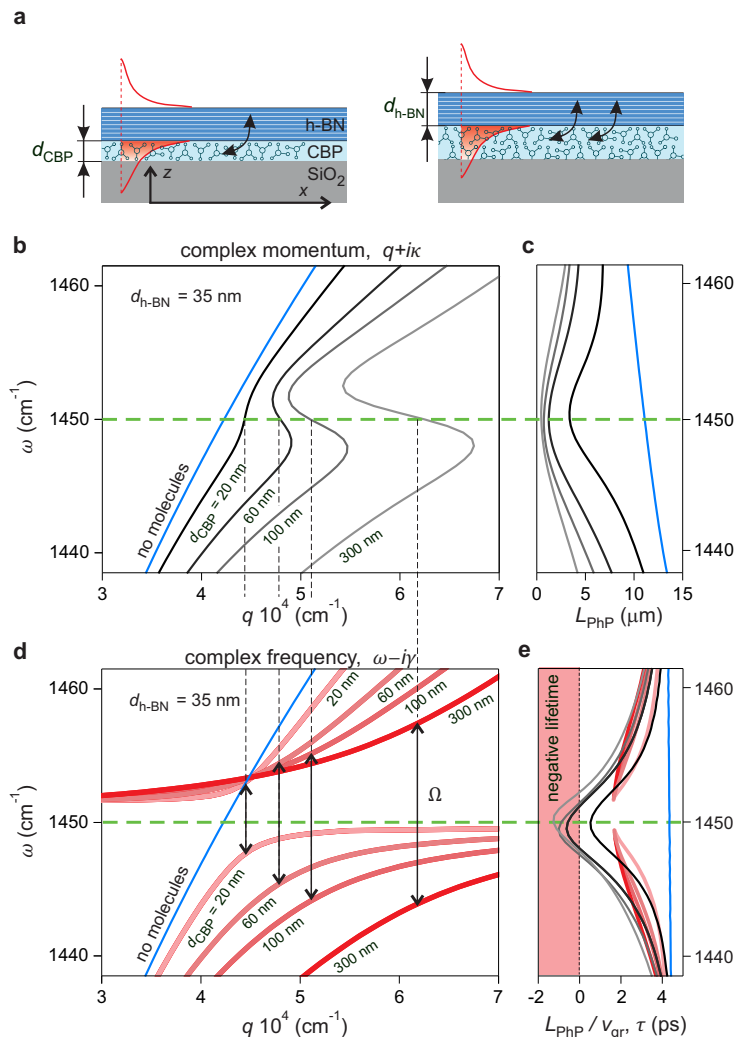


Figure 3.6: Dispersion and mode splitting. **a**, Illustration of PhPs on differently thick molecular layers. **b,e**, Dispersions of PhPs in a 35 nm-thick h-BN layer on CBP layers of various thicknesses d_{CBP} assuming complex momenta $q + ik$ (panel **b**) or complex frequencies $\omega - i\gamma$ (panel **e**). Horizontal green dashed line marks the frequency of the molecular vibrational resonance. **c**, PhP propagation length. **f**, Blue and red lines show PhP lifetime according to $\tau = 1/\gamma$. Black and gray lines show $L_{\text{PhP}}/v_{\text{gr}}$.

We deepen the insights into strong coupling between molecular vibrations and PhPs by an eigenmode analysis via TM calculations (analog to Fig. 3.5b) for various h-BN and CBP layer thicknesses. We first consider a variation of the CBP layer thickness d_{CBP} for a fixed h-BN thickness of 35 nm (Fig. 3.6b-e). We find that the region of anomalous dispersion widens when d_{CBP} is increased, which comes along with a reduction of the PhP propagation length L_{PhP} (i.e. increase of PhP damping) that reaches a finite minimum at the molecular resonance (Fig. 3.6c). Further, we find that with increasing d_{CBP} the mode

splitting Ω (the smallest vertical separation between the real frequency of the quasi-normal modes) and thus the coupling strength between PhPs and molecular vibrations increases (Fig. 3.6d), as simply more of the PhP fields lies inside the CBP layer (illustrated in Fig. 3.6a). Interestingly, the life times are rather large, about 2 ps, for all considered d_{CBP} (red curves in Fig. 3.6e), which is close to the molecular resonance lifetime of 1.7 ps and emphasizes that the coupled mode becomes more determined by the character of molecular absorption near the resonance. We note that the lifetime of the coupled mode being slightly longer than the lifetime of the bare molecular excitation has been also found by real-space observation of exciton polaritons [165]. In the region of anomalous dispersion PhPs propagate with negative group velocity, $v_g = d\omega/dq < 0$ (Fig. 3.3c and Fig. 3.6b), yet with finite propagation length (red symbols in Fig. 3.3d and Fig. 3.6c). Importantly, the negative group velocity yields negative values for the life time τ when calculated according to $\tau = L_{\text{PhP}}/v_g$ (black curves in Fig. 3.6e), implying that this lifetime determination – typically applied in polariton interferometry [22, 53, 80, 84, 166] – cannot be used in the case of anomalous dispersion. Instead, eigenmode analysis in the picture of a temporally decaying mode is required (red curves in Fig. 3.6e).

Plotting Ω as a function of d_{CBP} (red symbols in Fig. 3.7a), we find saturation at about 14 cm^{-1} for $d_{\text{CBP}} > 300 \text{ nm}$, where the whole PhP lies inside the CBP layer. Considering that the condition $C > 1$ in our simulations is fulfilled for $\Omega > 5 \text{ cm}^{-1}$, we find that strong coupling of CBP vibrations and PhPs in a 35 nm thick h-BN layer can be already achieved for $d_{\text{CBP}} > 20 \text{ nm}$. Remarkably, further numerical mode analysis for h-BN layers with reduced thickness of $d_{\text{h-BN}} = 5 \text{ nm}$ and 1 nm (green and black symbols in Fig. 3.7a, respectively) predicts that in future experiments strong coupling may be achieved with just a few CBP monolayers ($d_{\text{CBP}} < 2 \text{ nm}$). This can be explained by the extreme mode compression that comes along with the 100-fold reduced PhP wavelength compared to the photon wavelength ($\lambda_0 \approx 6.5 \mu\text{m}$) of the same energy (Fig. 3.7b) [21].

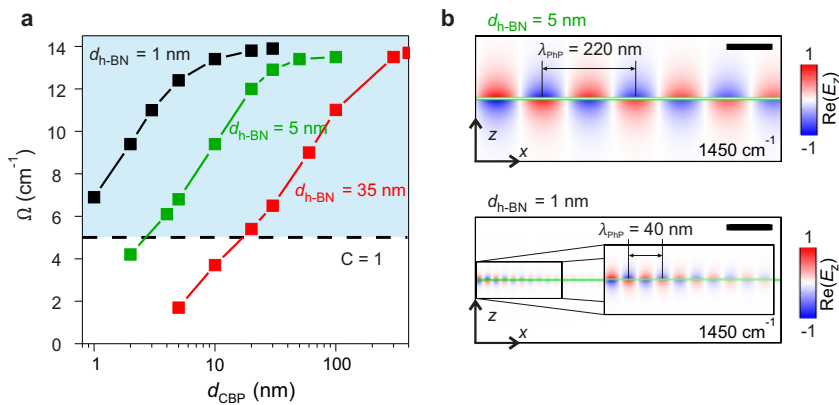


Figure 3.7: Mode splitting. **a**, Mode splitting Ω as a function of the molecular layer thickness d_{CBP} for h-BN layer with thickness $d_{\text{h-BN}}$ of 1 nm (black squares), 5 nm (green squares) and 35 nm (red squares). Horizontal black dashed line indicates the strong-coupling limit. **b**, Side view of the near-field distributions of the PhP mode propagating along h-BN layer, indicated by horizontal green lines, with thicknesses $d_{\text{h-BN}}$ of 5 nm (top) and 1 nm (bottom). Scale bar in both panels is 100 nm.

3.6 Conclusion

Our work demonstrates that propagating PhP in unstructured vdW materials can strongly couple to molecular vibrations, which could provide a platform for testing strong coupling and local controlling of chemical reactivity [4, 118, 150, 152]. In addition, it opens up possibility for ultracompact, on-chip spectroscopy [153]. A large variety of vdW materials are at the disposal to go beyond the spectral range of h-BN, as recently demonstrated by PhP observation on MoO₃ [53] and V₂O₅ [84]. In contrast to conventional polaritonic spectroscopy made with resonators (as, e.g. ribbons [13], cones [119] or hole arrays [167]) our work opens new avenues for studying strong-light matter interactions without the need of challenging sample structuring that typically comes along with additional losses from sample damage, inhomogeneities and scattering due to uncertainties in the sample fabrication process.

3.7 Supplementary information

3.7.1 Dielectric function of materials

CBP dielectric function

We measured the transmission spectrum of a 100 nm thick 4,4'-bis(Ncarbazolyl)-1,1'-biphenyl (CBP) layer evaporated on top of a CaF₂ substrate. To extract the dielectric function of the CBP molecules we used the following formula for thin films [13, 168]:

$$\frac{T}{T_0} = \frac{1}{\left|1 + \sigma(\omega) d_{\text{CBP}} \frac{Z_0}{n_{\text{sub}} + 1}\right|^2} \quad (3.3)$$

where d is the film thickness ($d_{\text{CBP}} = 100 \text{ nm} \ll \lambda_0 \approx 7 \text{ }\mu\text{m}$), n_{sub} is the refractive index of the substrate ($n_{\text{sub}} = 1.37$ for CaF₂ in the considered range), Z_0 is the impedance of free space ($377 \text{ }\Omega$) and $\sigma(\omega)$ is the complex conductivity of the thin film. $\sigma(\omega)$ is related to the permittivity, according to $\varepsilon(\omega) = 1 + \frac{i}{\omega\varepsilon_0}\sigma(\omega)$.

We modeled the dielectric function of the CBP molecules by the Drude-Lorentz model assuming 4 oscillators to describe the molecular vibrations as follows:

$$\varepsilon_{\text{CBP}}(\omega) = \varepsilon_{\infty} + \sum_k \frac{\omega_{p,k}^2}{\omega_{0,k}^2 - \omega^2 - i\Gamma_{\text{CBP},k}\omega}, k = 1 - 4 \quad (3.4)$$

where ε_{∞} is high-frequency dielectric constant, $\omega_{p,k}$, $\omega_{0,k}$ and $\Gamma_{\text{CBP},k}$ represent the plasma frequency, the resonance frequency and the linewidth of the k -th Lorentz oscillators, respectively. We assumed that $\varepsilon_{\infty} = 2.8$, which is consistent with ellipsometry measurements reported in the literature [169] and which allows for proper fitting. All fit parameters are shown in Table 3.1.

k	$\omega_{0,k}, \text{ cm}^{-1}$	$\omega_{p,k}, \text{ cm}^{-1}$	$\Gamma_{\text{CBP},k}, \text{ cm}^{-1}$
1	1450	128	6.4
2	1478.6	47	4.4
3	1500.1	91	9.4
4	1507.4	99	6.1

Table 3.1: Fit parameters of Eq. 3.3 of the CBP dielectric function.

h-BN dielectric function

We used the isotopically (^{10}B) enriched h-BN [80]. The dielectric permittivity tensor of h-BN is modeled according to the following formula:

$$\varepsilon_{\text{h-BN},j}(\omega) = \varepsilon_{\infty,j} \left(\frac{\omega_{\text{LO},j}^2 - \omega^2 - i\omega\Gamma_j}{\omega_{\text{TO},j}^2 - \omega^2 - i\omega\Gamma_j} \right), \quad (3.5)$$

where $j = \perp, \parallel$ indicates the component of the tensor perpendicular and parallel to the anisotropy axis. We took the parameters for the dielectric function of h-BN from ref. 80 except of ε_{∞} . We used $\varepsilon_{\infty} = 4.5$ instead of $\varepsilon_{\infty} = 5.1$ in ref. 80 for the best matching of our near-field experiments. We attribute the discrepancy to fabrication material parameter uncertainties. All parameters for the dielectric function, which were used in the simulation, are presented in the Table 3.2.

j	ε_{∞}	$\omega_{\text{TO}}, \text{cm}^{-1}$	$\omega_{\text{LO}}, \text{cm}^{-1}$	Γ, cm^{-1}
\perp	4.5	1394.5	1650	1.8
\parallel	2.5	785	845	1

Table 3.2: Parameters of the Eq. 3.5 of the dielectric function of h-BN.

Permittivity of the Si/SiO₂ substrate

We approximated the SiO₂ dielectric function taken data points from Palik [170], by following function:

$$\varepsilon_{\text{SiO}_2} = p_1\omega^4 + p_2\omega^3 + p_3\omega^2 + p_4\omega + p_5, \quad (3.6)$$

where ω is provided in units of wavenumbers. We took the following parameter: $p_1 = -2.27 \times 10^{-11} - 2.06 \times 10^{-12}i$, $p_2 = 1.50 \times 10^{-7} + 1.21 \times 10^{-8}i$, $p_3 = -3.74 \times 10^{-4} - 2.62 \times 10^{-5}i$, $p_4 = 0.42 + 0.025i$, $p_5 = -1.75 \times 10^2 - 8.816i$.

Simulations shown in Fig. 3.1, 3.2 and 3.5 consider the experimental Si/SiO₂ substrate, which is 150 nm-thick SiO₂ on highly doped Si ($\varepsilon_{\text{Si}^{++}} = -11.11 + 10.49i$). Note that the doped Si leads to the additional damping of PhPs. In future experiment the undoped Si should be used. Simulation shown in Fig. 3.6 and Fig. 3.7 consider a Si/SiO₂ substrate, which is 250 nm-thick SiO₂ on undoped Si ($\varepsilon_{\text{Si}} = 12$).

3.7.2 Data processing of the polariton interferometry experiments

Baseline subtraction from nano-FTIR line scans

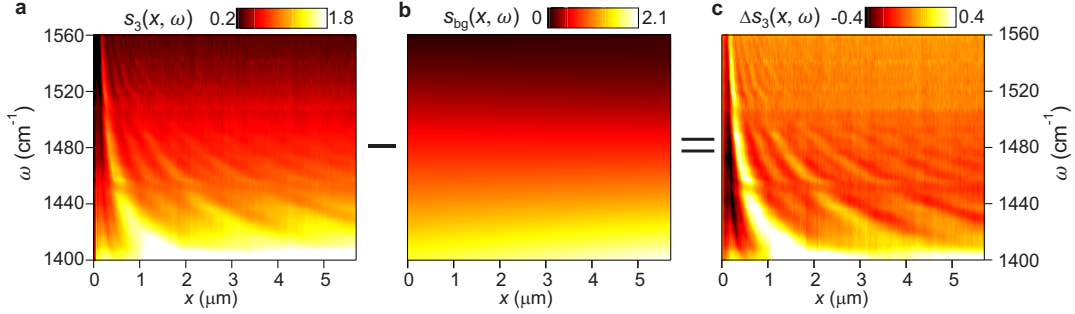


Figure 3.8: Polynomial baseline-subtraction. **a**, nano-FTIR amplitude signal $s_3(x, \omega)$ as a function of frequency and distance from the flake edge. **b**, Polynomial fit **c**, Baseline-subtracted nano-FTIR amplitude signal, $\Delta s_3(x, \omega)$.

In Section 3.3, we performed hyperspectral phonon polariton interferometry and analysed baseline-subtracted nano-FTIR line scans (Fig. 3.1d,h). We performed a baseline subtraction from the nano-FTIR line scans in the $q - \omega$ domain to highlight the signal oscillations due to polariton interference. Here, we explain the baseline subtraction procedure. Fig. 3.8a shows the amplitude of the original nano-FTIR line scan, $s_3(x, \omega)$, of the 50 nm-thick h-BN flake with 40 nm-thick molecular layer below. We fitted the data set of Fig. 3.8a by a polynomial function of the $n = 1$ order in horizontal x -axis) and $m = 2$ order in vertical (y -axis) directions, the fitted polynomial is:

$$\sum_{i=0}^n \sum_{k=0}^m a_{i,k} x^i y^k \quad (3.7)$$

We obtained the following parameter for the polynomial fit: $a_{0,0} = 2.14 \times 10^{-6}$, $a_{1,0} = -4.04 \times 10^{-3}$, $a_{0,1} = -0.04$, $a_{1,1} = 133.03$, $a_{0,2} = 196.58$, $a_{1,2} = -993.93 \times 10^3$. Fig. 3.8b shows the subtracted polynomial function, $s_{bg}(x, \omega)$. Fig. 3.8c shows the baseline-subtracted nano-FTIR amplitude signal, $\Delta s_3(x, \omega)$, which is also shown in Fig. 3.1d.

We performed the same baseline subtraction procedure for the nano-FTIR line scan without molecules. We obtained the following parameter for the polynomial fit: $a_{0,0} = 2 \times 10^{-6}$, $a_{1,0} = -8.21 \times 10^{-3}$, $a_{0,1} = -28.3 \times 10^{-3}$, $a_{1,1} = 213.85$, $a_{0,2} = 102.56$, $a_{1,2} = -1.41 \times 10^6$. Baseline-subtracted nano-FTIR line scan amplitude is shown in Fig. 3.1h.

Fourier transform of the nano-FTIR line scans

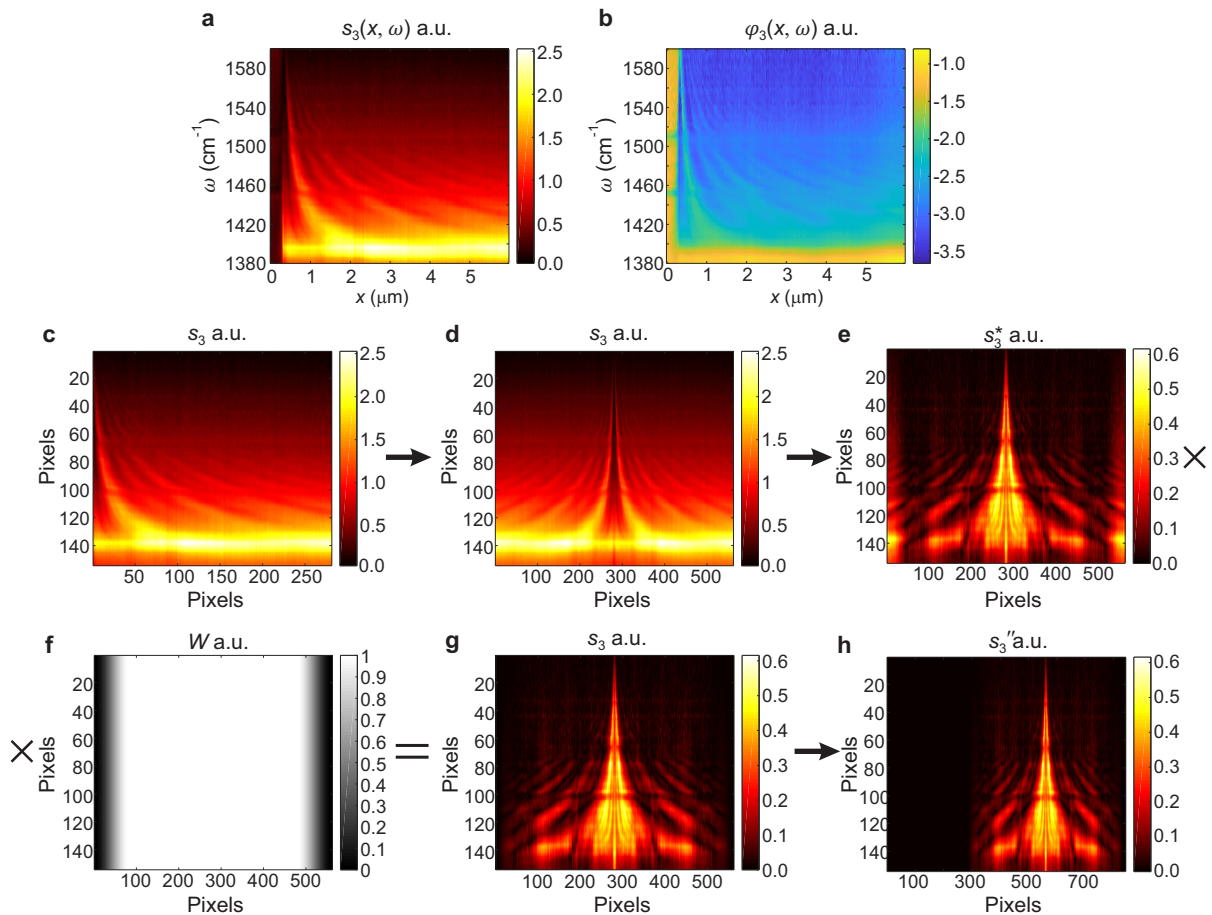


Figure 3.9: Preparation of nano-FTIR line scan for FT. **a**, Raw amplitude signal of the nano-FTIR line scan. **b**, Raw phase signal of the nano-FTIR line scan. **a,b**, Vertical dashed line indicates the h-BN flake edge. **c**, Amplitude signal of data set from only the h-BN/CBP layers structure. **d**, Amplitude signal of concatenated data set with mirrored data set. **e**, Baseline-subtracted amplitude signal of the data set. **f**, Window function. **g**, Amplitude signal of the data set after application of the window function. **h**, Final amplitude signal of the data set after zero padding.

In Section 3.3, we performed a Fourier transform (FT) on the nano-FTIR line scans to visualize and analyze the PhP dispersion. Here, we present the step-by-step data processing procedure that has been conducted. Fig. 3.9a,b show the raw amplitude, $s_3(x, \omega)$, and phase, $\phi_3(x, \omega)$, signals of the nano-FTIR line scan of the h-BN/CBP layers from Fig. 3.1. The raw data comprise 300 pixels along the x -axis (distance x axis) and 156 pixels along the y -axis (frequency axis). For the FT of the nano-FTIR line scan along the x -axis, we prepared the nano-FTIR line scan data set according to the following procedure (see Fig. 3.9):

1. Remove the part of the data set, which was measured outside the flake (data on the left side of the white dashed line in Fig. 3.9a,b, which indicates the edge of h-BN layer). Fig. 3.9c shows the amplitude signal of data set after this step.
2. Join the data set from Fig. 3.9c with its mirror image along the x -axis. Fig. 3.9d

shows the joint data set.

3. Perform baseline subtraction along the x -axis of the data set from Fig. 3.9d independently for each frequency. Fig. 3.9e shows the baseline-subtracted data set.
4. Apply window function (tukey window with cosine fraction 0.3, see Fig. 3.9f), W , to the data set from Fig. 3.9e. Fig. 3.9g shows the data set after windowing.
5. Zero-pad the data set from the Fig. 3.9g.

Fig. 3.9h shows the final data set after steps 1 to 5.

Note that in Fig. 3.9c-h we show only the amplitude of the nano-FTIR line scan, while data processing is done with the complex-valued data, that is, taking also into account the phase. The FT of the final data set yields Fig. 3.1e.

The raw complex-valued data set of the nano-FTIR line scan of h-BN without molecules was prepared in the same way before the FT. The FT of the final data set yields Fig. 3.1h.

Inverse Fourier transform of the isolated M0 mode

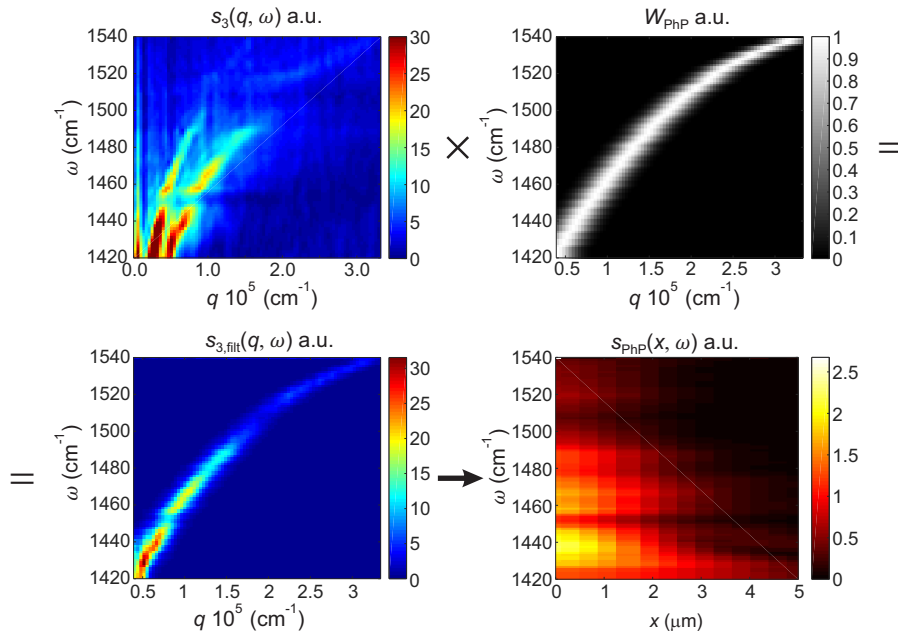


Figure 3.10: Filtering the T-branch in the $q - \omega$ domain. **a**, Amplitude of the FT in the $q - \omega$ domain. **b**, Filter function. **c**, Isolated T-branch after multiplication of panel **a** and panel **b**. **d**, Inverse FT of panel **c**, revealing the tip-scattered pure PP field as a function of x and ω .

In Section 3.3, we isolated and analyzed the tip-scattered phonon polariton (PhP) field, shown in Fig. 3.1f,j. Here, we outline the step-by-step data processing procedure that was conducted. To extract the tip-scattered PhP field, we apply a filter in the $q - \omega$ domain (Fourier space) to isolate the tip-launched mode (T-branch in Fig. 3.1e,i), and perform

an inverse Fourier transform (iFT) to obtain the tip-scattered field of the M0 mode in the $x - \omega$ domain [22]. This process is shown in Fig. 3.10, where the initial amplitude of the FT is shown in panel a, the applied filter function is shown in panel b, the filtered amplitude of the FT is shown in panel c, the result of the inverse FT is shown in panel d. The filter function $W_{\text{PhP}}(q, \omega)$ is a Gaussian function of the width $\Delta q = 0.4 \times 10^5 \text{ cm}^{-1}$.

Fouier transform of the line profiles of Fig. 3.3

In Section 3.4.1, we performed phonon polariton interferometry with improved signal-to-noise ratio and spectral resolution, and then analyzed the PhP dispersion in reciprocal space. Here, we outline the step-by-step procedures that were conducted. Firstly, we performed phonon polariton interferometry by s-SNOM employing a wavelength-tunable quantum cascade laser (QCL). By imaging the same sample area at various frequencies and averaging them in direction parallel to the h-BN edge, we obtained the line profiles for 85 nm-thick h-BN flakes with 100 nm thick layer of CBP molecules below (Fig. 3.3a) and pure 85 nm-thick h-BN without molecules.

Secondly, to prepare our amplitude line profiles for the FT, we first normalized each amplitude line profile to the amplitude signal far away from edge. In second step, we cut the first oscillation in the amplitude line profile (first fringe) to avoid contributions of edge modes [171] to our FT analysis. The remaining steps of the data preparation process for the FT were the same to the data preparation of the nano-FTIR data set (see Fourier transform of the nano-FTIR line scans section above). Fig. 3.3c,d show the result of the FT of the line profiles of h-BN/CBP and pure h-BN layers, respectively.

Phase velocity sign of the propagating molecule-coupled PhP mode

In Section 3.4.1, we studied the dispersion of PhP coupled with molecular vibration, which exhibits anomalous dispersion characterized by backbending. To confirm a negative group velocity of molecule-coupled PhP mode, it is important to verify the sign of phase velocity of PhPs. To check the sign of the PhPs phase velocities in the region of anomalous dispersion ($\omega = 1450 \text{ cm}^{-1}$) and compare with the phase velocities outside of the anomalous dispersion ($\omega = 1440 \text{ cm}^{-1}$, 1460 cm^{-1}), we plot in Fig. 3.11 the s-SNOM line profiles in the complex plane. We note that it is the same lineprofile, which were shown in Fig. 3.3a. We observe an anticlockwise rotating spiral at all frequencies, revealing positive phase velocities in these regions, which is consistent with the previous result for the PhPs [22].

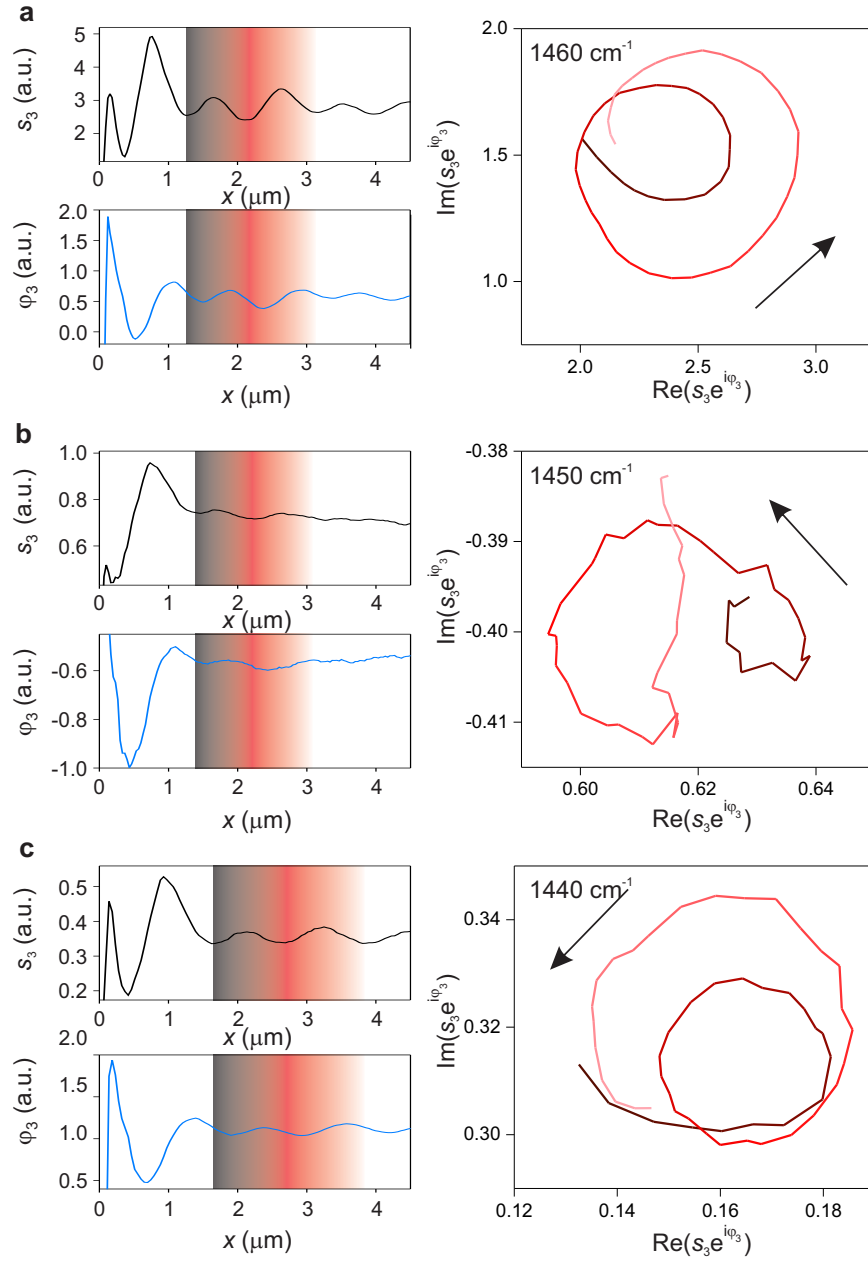


Figure 3.11: s-SNOM line profiles plotted in the complex plane. **a**, Black (blue) line shows the amplitude (phase) signal of the complex-valued s-SNOM signal as a function of the distance x . Gradient line (black-red-white) shows the signal in the complex plane corresponding the gradient area on the amplitude and phase line profiles. Black arrows indicate the anticlockwise direction of rotation, which corresponds to a positive phase velocity. **a**, $\omega = 1460 \text{ cm}^{-1}$, **b**, $\omega = 1450 \text{ cm}^{-1}$, **c**, $\omega = 1440 \text{ cm}^{-1}$.

4

Dual-band coupling of polaritons with vibrational and electronic excitations in molecules

In this chapter, we demonstrate by numerical simulations that strong coupling (SC) can be achieved simultaneously between surface plasmon polaritons (SPPs) and electronic transitions at visible frequencies and between phonon polaritons (PhPs) and molecular vibration at mid-IR frequencies. For an experimental study, we introduce a polaritonic nanoresonators (formed by h-BN layers on Al ribbons) hosting surface SPPs at visible frequencies and PhPs at mid-infrared (mid-IR) frequencies, which simultaneously couple to excitons and molecular vibrations in an adjacent molecular layer (CoPc). Employing near-field optical nanoscopy, we demonstrate the co-localization of confined near-fields at both visible and mid-IR frequencies. Far-field transmission spectroscopy of the nanoresonator structure covered with a layer of CoPc molecules shows clear mode splittings in both frequency ranges, revealing simultaneous SPP-exciton and PhP-vibron coupling. Dual-band SC may offer potential for manipulating exciton and molecular vibration coupling in future optoelectronics, nanophotonics, and quantum information applications.

The results discussed in this chapter have been published in the following paper:
A. Bylinkin *et al.* “Dual-band coupling of phonon and surface plasmon polaritons with vibrational and electronic excitations in molecules”, *Nano Lett.* **23.9**, 3985-3993 (2023).

4.1 Introduction

Strong coupling (SC) - light-matter interaction leading to the formation of new hybrid modes whose separation of energy levels is larger than the sum of their average linewidths - provides intriguing possibilities for controlling various material properties, such as e.g. carrier transport in organic semiconductors [2, 3], magnetotransport in two-dimensional electron gases [8], or chemical reactivity changes in microcavities [4–7]. Conventional optical resonators, such as Fabry-Perot microcavities, are typically used to couple matter excitations with light. An approach to explore SC at nanoscale is to use polariton resonators, enabling SC between excitons and surface plasmon polaritons (SPPs) at visible frequencies [12], or between molecular vibrations and phonon polaritons (PhPs) at mid-IR [13, 14] to THz frequencies [15, 16]. Interestingly, the interaction between excitons and molecular vibrations plays an important role in the optical properties of organic semiconductors [172–174], particularly in the singlet fission. Achieving dual-band SC, i.e. SC between polaritons and both excitons and molecular vibrations simultaneously could provide new opportunities for controlling the state of matter at the nanoscale. However, excitonic and vibrational resonances emerge at significantly different energy domains separated by orders of magnitude, thus challenging the creation of strongly confined electromagnetic fields (hotspots) at visible and infrared frequencies - an essential ingredient for achieving SC at the nanoscale - at the same spatial position and with a similar size. Metallic antennas have already been used to enhance the light-matter interaction in both visible and mid-IR frequency bands [175], in particular, to combine surface-enhanced Raman and infrared spectroscopy [176, 177]. However, although metallic antennas work relatively well in the visible range, it is desirable to find alternatives for achieving SC in the mid-IR frequency range due to their low quality factor at these frequencies.

Van der Waals (vdW) materials have recently emerged as a promising platform for exploring enhanced light-matter interactions at the nanoscale, as they support a large family of ultra-confined polaritons [17, 18] from visible to THz frequencies. In addition, these materials can be engineered with nanoscale precision, allowing precise control of light-matter interactions at subwavelength scales [77]. Furthermore, the combination of metal slabs or antennas with vdW materials can lead to hybrid heterostructures that support electromagnetic modes at different frequency ranges [178] and potentially allow the creation of co-located visible and infrared hotspots to achieve dual-band SC.

Here, we demonstrate by numerical simulations that SC can be achieved simultaneously between SPPs and electronic transitions at visible frequencies and between PhPs and molecular vibration at mid-IR frequencies. For an experimental study, we employed nanoresonators based on a heterostructures composed of metal (Al) ribbons and monoiso-

topic hexagonal boron nitride (h-BN) flakes, which support both SPPs at visible frequencies and PhPs at infrared frequencies. PhP resonances offer the advantage of being stronger and narrower as compared to SPP resonators [179], thus facilitating the achievement of nanoscale vibrational SC [13, 14]. We verify the two hotspots and their co-localization by scattering-type scanning near-field optical microscopy (s-SNOM). By placing molecules on the nanoresonators within the corresponding hotspots and performing visible and mid-IR far-field spectroscopy, we provide direct experimental evidence for large mode splitting in both frequency ranges.

4.2 Dual-band strong-coupling concept in a cavity-free structure

SC can be directly observed by visualizing the propagation of PhPs in a cavity-free (unpatterned) slab in contact with organic molecules [180, 181]. To explore the possibility of observing dual-band SC, we thus first perform a theoretical study considering a cavity-free heterostructure formed by a 50 nm-thick layer of CoPc between a 50 nm-thick Al layer and a 75 nm-thick h-BN slab (Fig. 1a). CoPc molecules support both a vibrational resonance at mid-IR frequencies (1525 cm^{-1}) and two excitonic resonances at visible frequencies (14400 cm^{-1} and 16200 cm^{-1}) (Fig. 4.1c,d). By placing the molecules between the two polaritonic materials (h-BN and Al) we expect to achieve highly confined mid-IR and visible electromagnetic fields inside the molecular layer (dashed lines in the left panel of Fig. 4.1a), thus guaranteeing a strong overlap of both fields and the molecules at the same spatial location. Since the plasma frequency of Al is $\omega_p = 10.83 \text{ eV} \approx 8.7 \times 10^4 \text{ cm}^{-1}$ [182, 183], the Al slab supports SPPs below $\omega_p/\sqrt{2} = 5.4 \text{ eV} \approx 1.4 \times 10^4 \text{ cm}^{-1}$, i.e. in the whole visible range. The field of these SPPs is vertically confined on a length scale of $1/q_{\text{SPP},z} \approx 100 \text{ nm}$ in the frequency range corresponding to the exciton resonances of CoPc. On the other hand, h-BN exhibits two mid-IR Reststrahlen bands - defined by the transverse (TO) and longitudinal (LO) optical phonons (785 to 845 cm^{-1} and 1394 to 1650 cm^{-1}) - where PhPs are supported [81]. Interestingly, since the out-of-plane and in-plane dielectric permittivities of h-BN differ in sign in both RBs, the h-BN slab supports a set of PhPs modes that are typically denoted M0, M1, etc. [52]. The fundamental M0 mode exhibits the longest wavelength and propagation length and thus is typically the dominating mode in h-BN nanoresonators [82, 119]. In the chosen structure, the momentum of the M0 mode at the molecular-vibrational resonance of CoPc is comparable to that of SPPs in the Al layer at the exciton resonance of CoPc. As a result, the vertical field confinement of the fundamental M0-PhP mode outside of the slab ($1/q_{\text{M0},z} \approx 80 \text{ nm}$) is comparable to that of the SPPs, indicating that a molecular layer with a thickness of a few dozens of nm should be sufficient to achieve SC in both frequency bands.

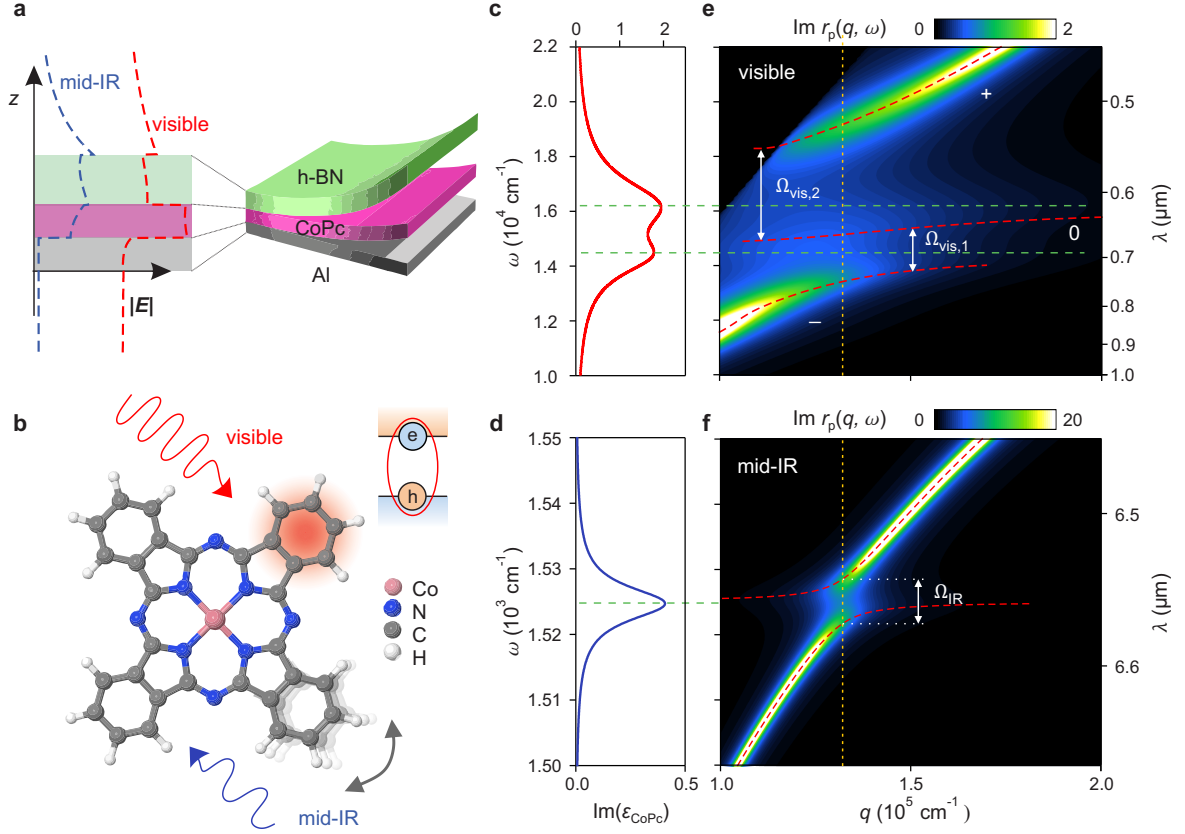


Figure 4.1: Dual-band SC between polaritons and molecular excitations at both visible and mid-IR frequencies **a**, Schematic of the three-layer structure considered (50nm-Al/50nm-CoPc/75nm-h-BN). Left panel: blue and red dashed lines show the mode profile of the polaritonic modes in the mid-IR and visible frequency ranges, respectively (blue line for $\omega = 1530 \text{ cm}^{-1}$, red line for $\omega = 19500 \text{ cm}^{-1}$). **b**, Schematic of the atomic structure of the molecule CoPc together with both the vibrational and excitonic resonances in it. **c,d**, Experimentally extracted $\text{Im}(\epsilon_{\text{CoPc}})$ in the visible and mid-IR frequency ranges, respectively. **e,f**, Colour plots showing the calculated imaginary part of the Fresnel reflection coefficient of the structure in both frequency ranges. Red dashed lines show the calculated dispersion of the quasi-normal modes, assuming complex-valued frequency and real-valued momentum. Horizontal green dashed lines indicate the resonance frequencies of the molecular excitations.

To explore the concept of simultaneous dual-band SC, we calculated the dispersion of the polaritons in the cavity-free (continuous) heterostructure, Fig. 4.1a. To that end, we plot the imaginary part of the Fresnel reflection coefficient, $\text{Im}[r_p(q, \omega)]$, at both visible and mid-IR frequencies (colour plots in Fig. 4.1e and 4.1f, respectively). The dashed red curves represent the dispersions of the quasi-normal polaritonic modes calculated from the poles of $r_p(q, \omega_c)$ in the plane of the complex-valued frequency $\omega_c = \omega - i\Gamma/2$, with Γ being the mode linewidth. Both colour plots and dispersion curves clearly reveal an anti-crossing (mode splitting) in both visible and mid-IR frequency ranges. To characterize the anti-crossing, we determine the mode splitting, Ω , as the minimum vertical distance between the real part of the complex frequencies. The comparison of Ω with half the sum of the linewidths of the upper, Γ_+ , and lower, Γ_- , coupled states determines whether the coupling between polaritons and molecular excitations is weak, $\Omega < (\Gamma_+ + \Gamma_-)/2$, or strong, $\Omega > (\Gamma_+ + \Gamma_-)/2$ [1]. In the mid-IR frequency range, our calculation yields $\Omega_{\text{IR}} = 6.8 \text{ cm}^{-1} \approx 8.4 \times 10^{-4} \text{ eV}$ and $\Gamma_{\text{IR},\pm} = 4 \text{ cm}^{-1} \approx 5 \times 10^{-4} \text{ eV}$, such that the SC

condition is well fulfilled. Although all Mn-PhP modes couple to the molecular vibration, we consider in the analysis shown in Fig. 1f only the M0 PhP mode, because it is dominant mode exhibiting the lowest q . In the visible range, the three initial excitations (SPP and two excitons) couple, leading to the formation of three hybrid states (red dashed lines in Fig.4.1e). By extracting the mode splitting as the minimum vertical distance between the real frequencies of the adjacent hybrid states, we obtain $\Omega_{\text{vis},1} = 1.6 \times 10^3 \text{ cm}^{-1} \approx 0.2$ eV (between the low “-” and middle “0” branches) and $\Omega_{\text{vis},2} = 3.9 \times 10^3 \text{ cm}^{-1} \approx 0.48$ eV (between the middle “0” and upper “+” branches). We found that the SC criterion is fulfilled for the split branches “0” and “+”, since $\Omega_{\text{vis},2} > (\Gamma_{\text{vis},2,+} + \Gamma_{\text{vis},2,0})/2$, where $\Gamma_{\text{vis},2,+0} \approx 1.6 \times 10^3 \text{ cm}^{-1} \approx 0.2$ eV is the linewidth of the middle and upper hybrid states, respectively. On the other hand, the SC criterion is not fulfilled for the split branches “-” and “0”. Altogether, our calculations reveal that the combination of different polaritonic materials in a single heterostructure can be used to achieve dual-band SC.

4.3 Sample preparation

To fabricate nanoresonator heterostructures for the experiments, we first fabricated Al metal ribbon arrays on a CaF_2 substrate (see Al metal ribbon arrays fabrication section below). Next, we transferred an exfoliated thin layer of h-BN onto these Al ribbon arrays (see h-BN crystal flake section below). Then we performed near- and far-field experiments without molecules (shown in Section 4.4.1). After that, we evaporated 80 nm of CoPc molecules on the nanoresonator heterostructure (see molecule deposition section below) to study the coupling between polaritons and molecular excitations (shown in Section 4.5.1).

Al metal ribbon arrays fabrication

Aluminium (Al) metal ribbon arrays (size of each array is $20 \mu\text{m} \times 20 \mu\text{m}$) with different width, w , of ribbons are fabricated using high-resolution electron beam (e-beam) lithography. The periods of the structures, p , were designed to be twice the width of the ribbons, $p = 2 \times w$. The 50 nm of Al layer was e-beam evaporated onto the CaF_2 substrate. Then negative resist (MA-N2401, 90 nm) was spin-coated followed by e-beam lithography of gratings (50 keV, 200 pA, dose $225 \div 375 \mu\text{C}/\text{cm}^2$) and resist development in AZ726 and reactive ion etching (RIE) of Al in BCl_3/Cl_2 plasma (pressure 40 mT, RIE power 100W). The resist was finally removed in O_2 plasma. Fig. 4.2 shows scanning electron microscope (SEM) images of the fabricated ribbon arrays. We extracted p and w from the measured SEM images and made sure that the filling factors, $f = w/p$, were indeed approximately 1/2 for all the fabricated structures. It is important to note that in all figures, to plot the quasi-normal modes of nanoresonator heterostructures we used doubled inverse period,

$2p^{-1}$, instead of the inverse ribbon width, w^{-1} . The extracted p , w and calculated f , p^{-1} parameters of the ribbon arrays are presented in Table 4.1.

p , nm	w , nm	$f = w/p$	$1/p$, 10^{-3} nm^{-1}
300	136	0.45	3.33
339	160	0.47	2.94
355	180	0.51	2.82
370	190	0.51	2.70
388	190	0.52	2.58
419	220	0.49	2.39
500	261	0.52	2.00

Table 4.1: Parameters of the fabricated arrays of Al ribbons, which are shown in Fig. 4.2.

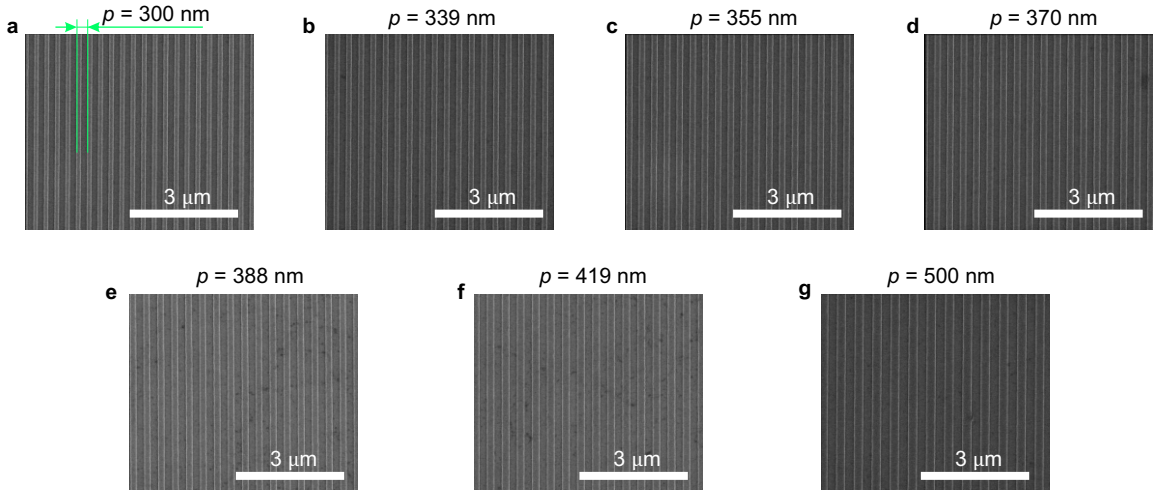


Figure 4.2: SEM images. SEM images of the fabricated arrays of Al ribbons, with the corresponding names of the arrays above the images. Fabrication of the Al ribbons was done by Roman Kirtaev at XPANCEO (Dubai, UAE).

h-BN crystal flake

The h-BN crystal flake was grown from a metal flux at atmospheric pressure as described previously [92]. The thin layer used in this study was prepared by mechanical exfoliation with blue Nitto tape. Then, we performed a second exfoliation of the h-BN flakes from the tape onto a transparent polydimethylsiloxane (PDMS) stamp. Using optical inspection of the h-BN flake on the stamp, we identified a high-quality flake with appropriate thickness. This flake was transferred onto a CaF_2/Al gratings substrate using the deterministic dry transfer technique. To pick up and transfer this flake to another set of Al gratings we used a PDMS stamp with polycarbonate film, following the procedure described in ref. 184.

Molecule deposition

Cobalt(II) Phthalocyanine, CoPc with sublimed quality (99.9%) (Sigma-Aldrich, Saint Louis, MO, USA) was thermally evaporated in an ultra-high-vacuum evaporator chamber (base pressure $< 10^{-9}$ mbar) at a rate of 0.2 nm s^{-1} using a Knudsen cell. Molecule deposition was done by Francesco Calavalle at CIC Nanogune BRTA (Donostia, Spain).

4.4 Polaritonic nanoresonators

4.4.1 Far- and Near-field characterization

To demonstrate experimentally the dual-band SC between polaritons and CoPc molecular excitations, we first have to consider the need to access the large intrinsic momenta of polaritons, which in the case of far-field illumination requires the presence of leaky modes in the heterostructure. The latter can arise in open Fabry-Perot (FP) nanoresonators, which can be fabricated by (i) nanostructuring the polaritonic slab, e.g. in the form of ribbons [13, 14, 60], or (ii) nanostructuring the substrate below the h-BN slab [63], i.e. by refractive index engineering. Importantly, the latter option allows the use of a pristine h-BN slab, thus preserving its crystal quality. Interestingly, by placing a 75 nm-thick h-BN flake on an Al grating (Fig. 4.3a), we can engineer FP nanoresonators by simultaneously applying concepts (i) and (ii). Indeed, while SPPs propagating across the Al ribbons (along the x -axis) in the visible range reflect directly at the Al edges (concept i), PhPs in the h-BN slab are reflected between the h-BN/air and h-BN/Al boundaries due to a refractive index step at mid-IR frequencies (concept ii). Fig. 4.3b,c show the normalised measured far-field extinction spectra of the nanoresonators in both frequency ranges. We can clearly recognize asymmetric peaks around $\omega_{\text{mid-IR}} = 1510 \text{ cm}^{-1}$ and $\omega_{\text{vis}} = 1.6 \times 10^4 \text{ cm}^{-1}$, which are identified (see Section 4.4.2) as Fano-type FP resonances and, partially, as Bragg resonances arising from the overlap between the electromagnetic fields of adjacent cavities. As the inverse width of the Al ribbons (w^{-1}) corresponds to an effective momentum of the resonating polaritons, we fabricated a set of structures with different w , in order to cover a wide range of momenta (see Section 4.3).

To corroborate our far-field spectroscopy experiments and to better understand the distribution of the near-field amplitude at the frequencies of the extinction peaks in Fig. 4.3b,c, we performed s-SNOM nanoimaging of the nanoresonator heterostructure (see schematics in Fig. 4.3g,h) at mid-IR and visible frequencies. In these nanoimaging experiments, the nanoresonators were illuminated with s -polarised light, whose electric field is perpendicular to the metal ribbons. The top panels in Fig. 4.3e,f show the resulting s-SNOM images for a nanoresonator when recording tip-scattered p -polarized light, which yields

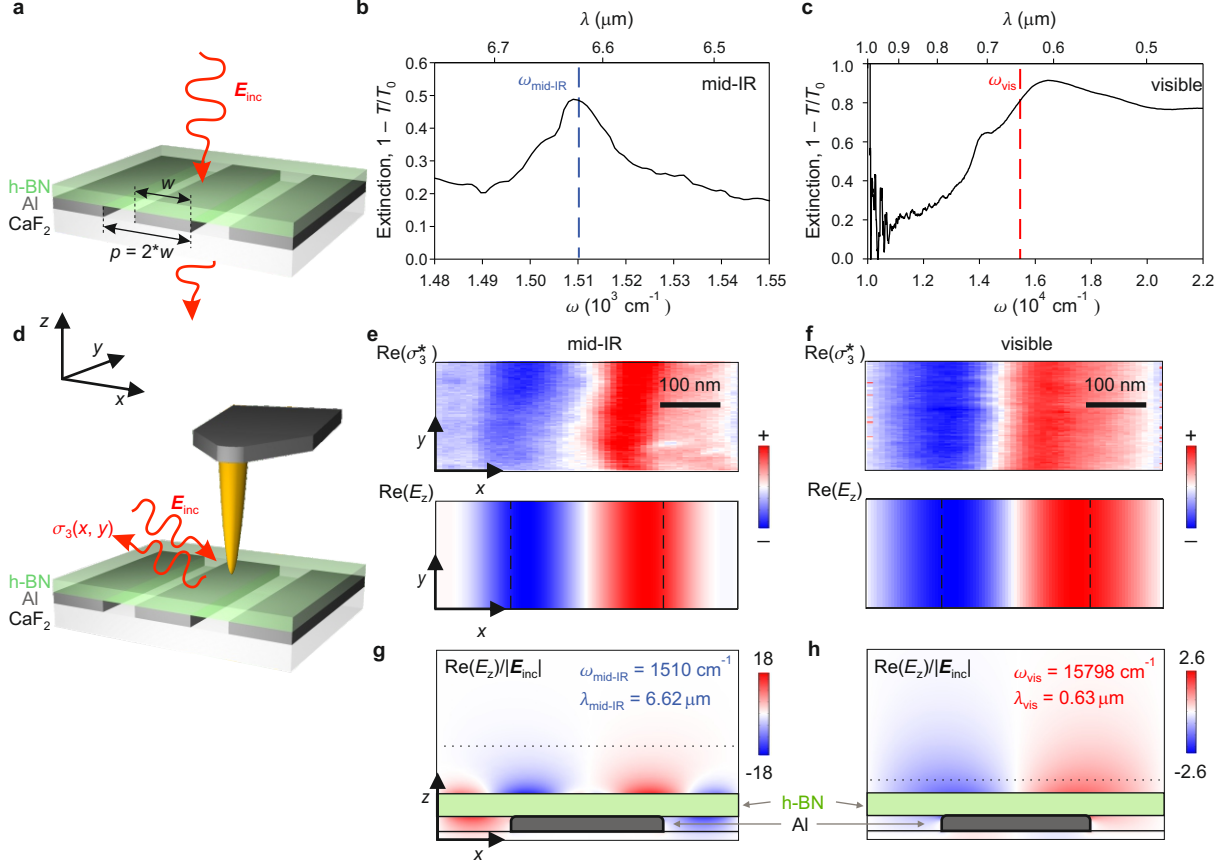


Figure 4.3: Experimental demonstration of dual-band polaritonic nanoresonators. **a,d** Schematics of the far-field experiments and s-SNOM optical characterization of the polaritonic nanoresonators. **b,c**, Experimental extinction spectrum of the nanoresonators created by employing an Al grating with period p 500 nm in the mid-IR and visible frequency ranges, respectively. **e,f**, (top panels) Near-field images of the nanoresonators in the mid-IR and visible frequency ranges, measured at $\omega_{\text{mid-IR}} = 1510 \text{ cm}^{-1}$ and $\omega_{\text{vis}} = 15798 \text{ cm}^{-1}$ as indicated by the blue and red dashed lines in **b,c**, respectively. A clear dipolar fundamental mode is observed in both cases. (Bottom panels) Simulated $\text{Re}(E_z)$ in the $x - y$ plane, extracted 80 and 20 nm above the structure as indicated by the vertical dashed lines in **g** and **h**, respectively. Vertical dashed lines indicate the edges of Al ribbon. **g,h**, Simulated $\text{Re}(E_z)/|\mathbf{E}_{\text{inc}}|$ in the $x - z$ plane at the same frequencies. The period of the Al grating, the width of the Al ribbon and the thickness of the h-BN slab employed in the bottom panels **e,f** and **g,h** are $p = 500 \text{ nm}$, $w = 250 \text{ nm}$, and $d_{\text{h-BN}} = 75 \text{ nm}$, respectively.

the z -component of the real part of the electric field at mid-IR ($\omega_{\text{mid-IR}} = 1510 \text{ cm}^{-1}$, $\lambda_{\text{mid-IR}} = 6.62 \mu\text{m}$) and visible ($\omega_{\text{vis}} = 15798 \text{ cm}^{-1}$, $\lambda_{\text{vis}} = 0.632 \mu\text{m}$) frequencies (data processing details in Section 4.8). Interestingly, despite the large difference in the wavelength of the incident light, we observe two bright areas with opposite polarity above the Al ribbons for both frequencies, revealing the excitation of transverse Fabry-Perot modes. To support these observations, we performed numerical simulations considering a nanoresonator with the experimental parameters and illuminating conditions. As can be clearly seen in the lower panels of Fig. 4.3e,f, excellent agreement is obtained between the simulated and experimental near-field distributions. In the normalized distributions of the vertical component of the electric fields (Fig. 4.3g,h), we identify strongly enhanced field amplitudes compared to the incident electric field, \mathbf{E}_{inc} , thus confirming the

formation of the hotspots. Therefore, we can conclude that the peaks observed in the far-field extinction spectra correspond to transverse Fabry-Perot resonances of PhPs at mid-IR frequencies and SPPs at visible frequencies. More importantly, the s-SNOM images in combination with the simulations confirm that both mid-IR and visible hotspots are spatially co-localized on the metal ribbons, thus potentially allowing for dual-band light-matter coupling involving the same molecules.

4.4.2 Theoretical analyses of the polaritonic modes

To study polaritonic modes in the nanoresonator heterostructure we performed the full-wave numerical simulation of electromagnetic fields using the finite-element method in frequency domain (COMSOL). We assumed a two dimensional (2D) geometry, namely an infinite number of infinitely long Al ribbons below the h-BN slab. We simulated transmission, reflection and scattering of a plane monochromatic wave normally incident onto the periodic array of nanoresonators. Fig. 4.4a shows the schematics of one period of the simulated structure.

The right panels of Fig. 4.4b,c show the calculated far-field extinction spectra, $1 - T$, where the T is the power transmission coefficient in the visible and mid-IR frequency ranges, respectively. The calculated extinction spectra in both frequency ranges reveal numerous peaks. In the visible frequency range, we can clearly recognize a sharp peak in the extinction spectrum around $\omega = 1.4 \times 10^4 \text{ cm}^{-1}$ followed by a broad peak around $\omega = 1.65 \times 10^4 \text{ cm}^{-1}$ (Fig. 4.4b, right panel). Both peaks form the so-called Wood-Rayleigh anomaly. Namely, the sharp peak (Rayleigh point) corresponds to the zero value of the z -component of the wavevector of the 1st order diffracted wave in the CaF_2 substrate. It takes place directly at the boundary between frequency regions where the 1st order diffracted wave has evanescent and propagating character. In contrast, the second peak (Wood anomaly) represents the first-order SPP Bragg resonance, corresponding to the pole in the transmission and reflection coefficients, and partially the Fabry-Perot (FP) resonance appearing as a result of multiple reflection of SPP mode (along the x -axis) from the edges of Al ribbons. In the mid-IR frequency range, the extinction spectrum manifests multiple peaks (Fig. 4.4c, right panel). We assume that the latter emerge due to FP resonances appearing as a result of multiple reflection of PhP waveguiding modes from their refractive index steps defined along the x -axis by Al ribbons. Notice that in the nanoresonators, the region of the h-BN slab above the Al ribbons supports all the propagating PhP modes M_n , with n starting from 1, and M1 mode possessing the lowest q . In contrast, the slab region above the air (in between of the Al ribbons) supports M_n modes with n starting from 0, and M0 mode having the lowest q . Our further analysis shows that the role of M1 mode in the whole nanostructure with the selected Al ribbon widths is dominating.

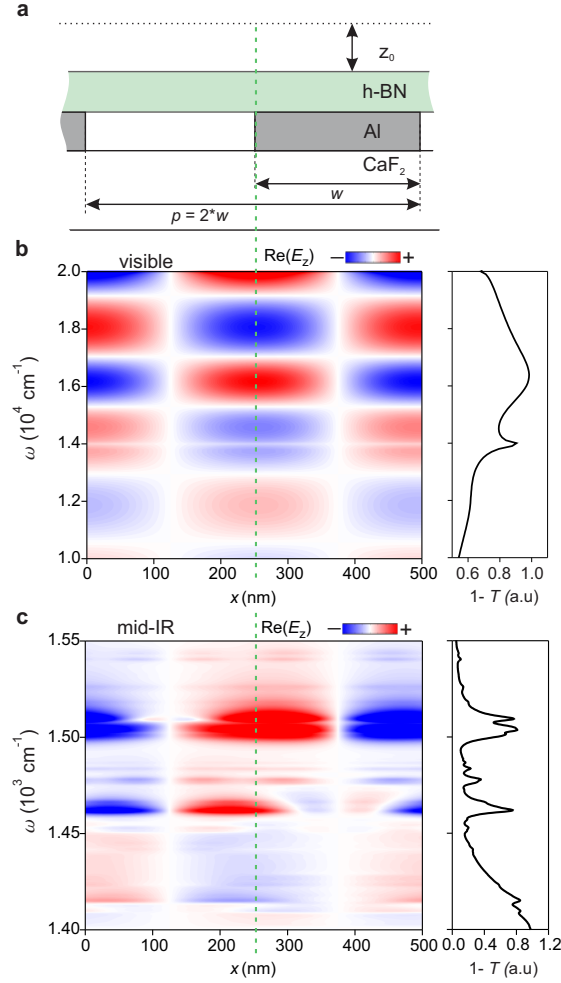


Figure 4.4: Analysis of the polaritonic resonances in the visible and mid-IR frequency ranges **a.** Schematics of one period of the nanoresonator heterostructure with the period, $p = 500$ nm, and Al ribbon width, $w = 250$ nm. **b,c,** (left panel) Simulated electric field at the height of $z_0 = 80$ nm above the h-BN layer as a function of ω and x coordinate in the visible and mid-IR frequency ranges, respectively. (right panel) Simulated extinction spectrum of the nanoresonator heterostructure in the visible and mid-IR frequency ranges, respectively.

To analyze and interpret these peaks we generate the colour plots (left panels of Fig. 4.4b,c), representing the z -component of the electric field above the h-BN slab as a function of the frequency, ω , and coordinate, x . In the visible frequency range, we observe the periodic field pattern along both the frequency and coordinate axes (Fig. 4.4b, left panel). We see two bright localized areas (“hotspots”) of different polarity along the coordinate axis, x , which can be explained by the presence of the transverse FP mode in the considered frequency range. We note that this FP mode can also be recognized in the simulated field distribution, $\text{Re}(E_z)/|\mathbf{E}_{\text{inc}}|$, in the x - z plane at $\omega_{\text{vis}} = 15798 \text{ cm}^{-1}$ (Fig. 4.3h). We speculate that the periodicity of the field pattern along the frequency axis arises due to the complex interference between the electromagnetic fields of the FP mode and the incident and reflected waves. In the mid-IR frequency range, we find two frequency regions around $\omega = 1460 \text{ cm}^{-1}$ and $\omega = 1510 \text{ cm}^{-1}$ with the bright localized areas of the different polarity along the coordinate axis. These bright areas arise due to the presence of transverse FP

resonances of PhP waveguiding modes at corresponding frequencies. These FP resonances can be characterized as “bright” modes since they have a nonzero in-plane dipole moment which can couple with propagating waves in free-space. As a result, these resonances appear as peaks in the far-field extinction spectrum (see the right panel of Fig. 4.4c). In the colour plot shown in the left panel of Fig. 4.4c, we see that at $\omega = 1460 \text{ cm}^{-1}$, a large portion of the mode volume is localized above the air region. In contrast, at $\omega = 1510 \text{ cm}^{-1}$ the electric field of the mode is mainly localized above the Al ribbon. These observations allow us to assign the resonance around $\omega = 1460 \text{ cm}^{-1}$ to the FP resonance of the M1 PhP mode in h-BN slab above the air region. In contrast, a multi-peak in the extinction spectrum around the $\omega = 1510 \text{ cm}^{-1}$ can be attributed to the FP resonances of the M1 PhP modes above the Al ribbons. We explain the multi-peak structure in the extinction spectrum of the resonance around $\omega = 1510 \text{ cm}^{-1}$ by the presence of higher-order PhP waveguiding modes in the h-BN layer. We finally identify the multi-peak resonance around $\omega = 1510 \text{ cm}^{-1}$ as FP resonances and, partially, as Bragg resonance arising from the overlap between the electromagnetic fields of adjacent air and Al regions.

Note that, in contrast to the simulation, the experimental extinction spectrum in Fig. 4.3b shows only the single resonant peak around $\omega = 1510 \text{ cm}^{-1}$. This discrepancy can be explained by the fabrication uncertainties of the Al ribbon width throughout the array and by quality of the Al edges that play a crucial role in the far-field excitation of the higher-order PhP waveguiding modes in the h-BN slab.

4.5 Coupling between polaritons and molecular excitations

4.5.1 Extinction spectra of the molecule covered nanoresonators

To study experimentally the frequency splitting of the hybridized modes, we evaporated an 80 nm thick layer of CoPc molecules - for practical reasons - on Al/h-BN nanoresonators with different ribbon widths, w (inset of Fig. 4.5), and measured the far-field extinction spectra in the mid-IR and visible frequency ranges (Fig. 4.5a,b).

In the mid-IR frequency range (Fig. 4.5a) we clearly observe peaks in the spectra that shift to higher frequencies as w^{-1} increases. The dashed black lines indicate the anti-crossing behavior of these peaks around the molecular vibration frequency at 1525 cm^{-1} (vertical green dashed line, Fig. 4.5a). This anti-crossing behavior reveals the coupling of PhPs with molecular vibration.

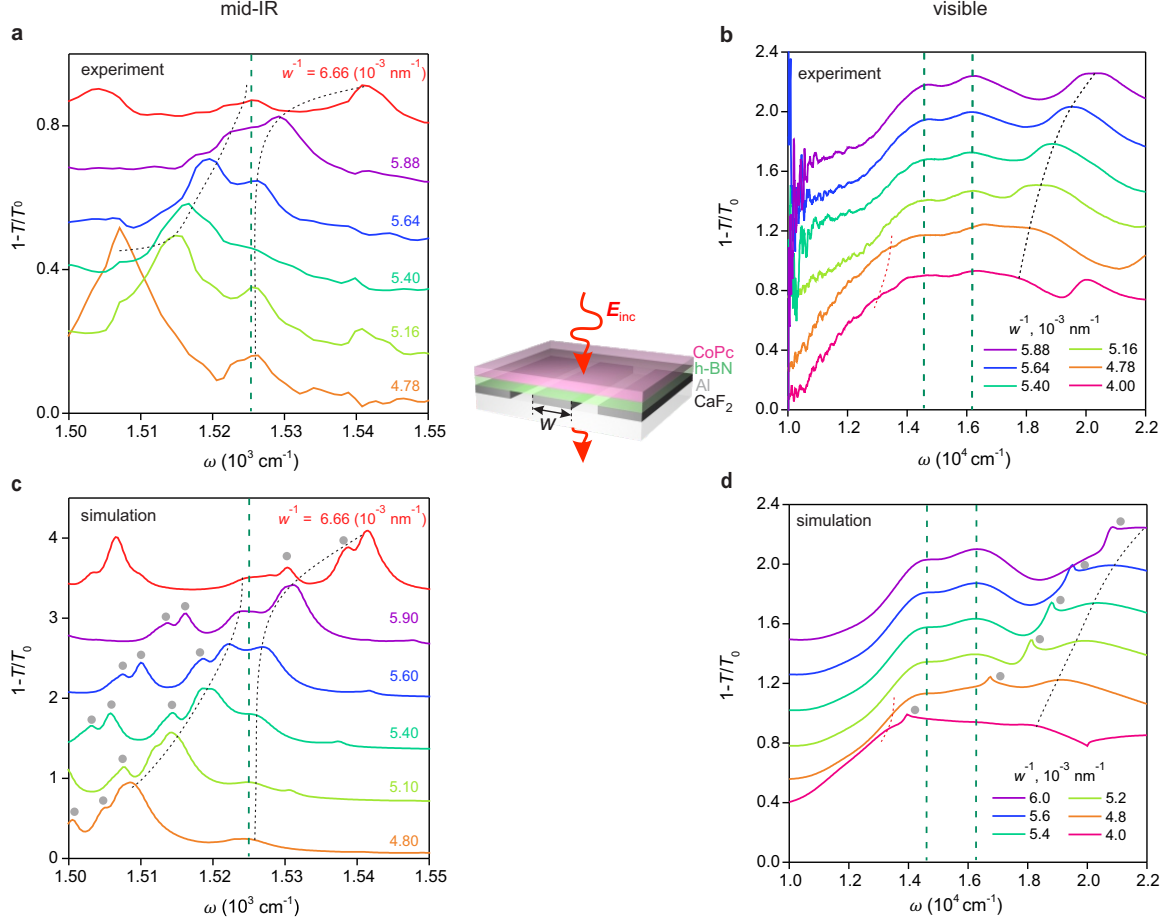


Figure 4.5: Extinction spectra of molecule-covered nanoresonators. **a,c** Experimental and simulated extinction spectra of the nanoresonators coated with a 80 nm thick CoPc layer in the mid-IR frequency range, respectively (see schematics). Vertical green dashed lines indicate the resonance frequency of the molecular vibration. Black dashed lines are guides to the eyes, indicating the peak position of the PhP mode coupled to the molecular vibration. Grey dots mark peaks, which correspond to the FP resonances of higher-order PhP waveguiding modes in the h-BN layer (see section 4.4.2). The spectral resolution is 1 cm^{-1} . **b,d**, Experimental and simulated extinction spectra of the nanoresonators coated with a 80 nm thick CoPc layer in the visible frequency range, respectively (see schematics). Vertical green dashed lines indicate the resonance frequencies of the molecular excitons. Red and black dashed lines are guides to the eyes, indicating the peak position of the SPP mode coupled to the molecular excitons. Grey dots mark peaks that correspond to the Rayleigh points, which occur at the frequencies where the 1st order diffracted wave changes its characteristic from evanescent to propagating (see section 4.4.2).

In the visible frequency range (Fig. 4.5b) we observe two peaks at the frequencies of the two molecular excitons (indicated by two vertical dashed green lines). These peaks reveal the absorption by the molecular excitons. Most importantly, in the frequency range above the molecular excitons we observe peaks (marked by a black dashed line) whose positions shift to higher frequencies as w^{-1} increases, whereas in the frequency range below the molecular excitons we find small shoulders (marked by a red dashed line) in the spectra for $w^{-1} = 4 \times 10^{-3}$ and $4.78 \times 10^{-3} \text{ nm}^{-1}$ (orange and pink curves). The red and black dashed lines show the anti-crossing behavior of these peaks and shoulders around the molecular excitons (two vertical dashed green lines, Fig. 4.5b). This anti-crossing behavior reveals the coupling between SPPs and molecular excitons.

To corroborate our experimental spectra, we simulated extinction spectra of the experimentally studied nanoresonators (Fig. 4.5c,d). We find that the simulated spectra reproduce well the experimental ones in both frequency ranges. We also find good agreement between the peak positions of the simulated and experimental spectra in both frequency ranges, particularly for the peaks marked by the black dashed lines. Most importantly, the simulated spectra exhibit an anti-crossing behavior similar to the one observed in the experimental spectra.

We note that we also find peaks in the simulated spectra that are not observed in the experimental spectral. In the mid-IR frequency range (Fig. 4.5c), the gray dots mark peaks that correspond to FP resonances of higher-order PhP waveguiding modes in the h-BN layer (see Section 4.4.2). In the visible frequency range (Fig. 4.5d), the gray dots mark peaks that correspond to the Rayleigh points, which occur at the frequencies where the 1st order diffracted wave changes its characteristic from evanescent to propagating (see Section 4.4.2). We explain the absence of these peaks in the experimental spectra by irregularities in the Al ribbon width and the quality of the Al edges, which may lead to additional scattering and thus damping of polaritons. Polaritons of stronger confinement, such as higher order modes, are typically stronger affected and eventually disappear [14].

4.5.2 Quasi-normal mode analysis

To theoretically quantify the mode splitting, we performed a quasi-normal polaritonic mode analysis for a three-layer CoPc/h-BN/Al continuous heterostructure on top of CaF₂ substrate. In contrast to the analysis shown in Fig. 4.1f, we now consider the M1 PhP mode in the mid-infrared spectral range, since the M0 PhP mode is absent when the h-BN layer is directly on top of a metal (Al). The calculated dispersions of the quasi-normal modes, $\omega(q)$, are shown on top of the simulated extinction spectra in Fig. 4.6b,d (dashed red lines). To compare the mode dispersion and the simulated extinction spectra, we related the real-valued in-plane polariton momenta, q , with the width of the grating, w , for each frequency range, $w^{-1} = 2q/(\pi - \alpha_{\text{vis,IR}})$, where $\alpha_{\text{vis}} = -0.12\pi$, $\alpha_{\text{IR}} = -0.3\pi$ are fit constants for the visible and mid-IR ranges, respectively. According to a simple FP model, the extracted values of the parameter $\alpha_{\text{vis,IR}}$ can be interpreted as the phase acquired by the polaritonic modes under reflection from the Al ribbon edges (SPP modes) and refraction index step in h-BN slab (PhP modes). We find excellent agreement between the calculated dispersions of the polaritons and the positions of the peaks in the extinction spectra in both spectral ranges. This agreement demonstrates that the interaction between polaritons and matter excitations in the continuous heterostructure is approximately equivalent to that in the nanoresonator heterostructure, which justifies that the analysis of a continuous heterostructure can be used to characterize the coupling parameters in the nanoresonator heterostructure. From the quasi-normal mode analysis we extract a mode splitting at mid-IR frequencies of $\Omega_{\text{IR}} = 5.9 \text{ cm}^{-1} \approx 7.3 \times 10^{-4} \text{ eV}$, and

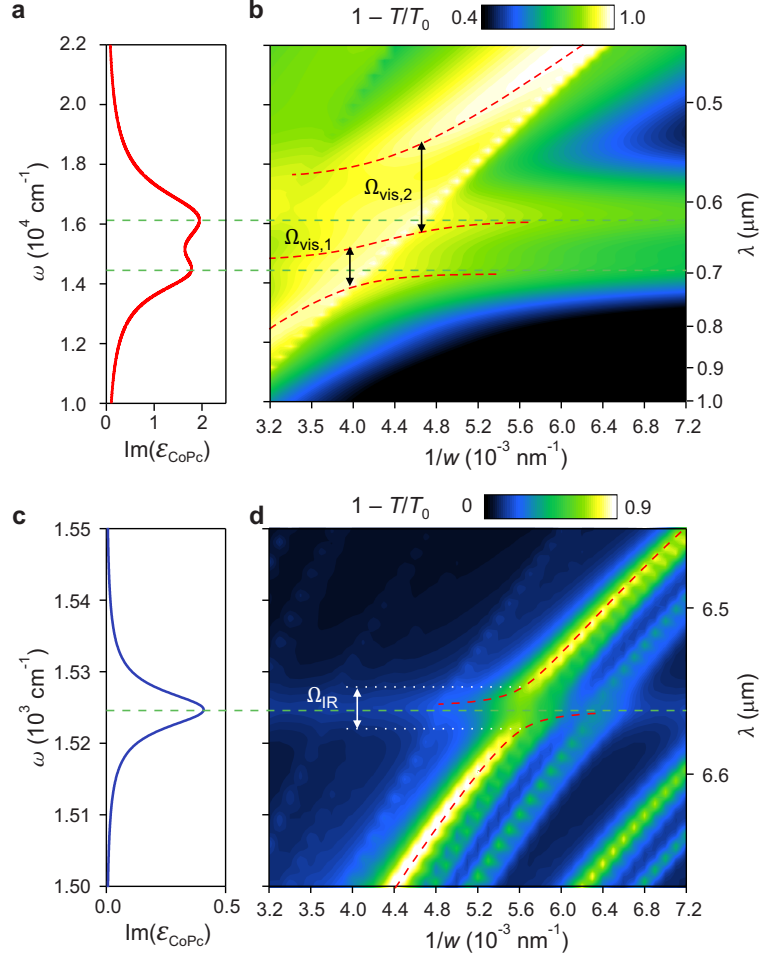


Figure 4.6: Quasi-normal polaritonic mode analysis. **a,c** Imaginary part of the permittivity of CoPc molecules $\text{Im}(\epsilon_{\text{CoPc}})$ experimentally extracted in the visible and mid-IR frequency ranges, respectively. **b,d**, Colour plots showing the simulated extinction of the nanoresonators in the visible and infrared frequency ranges, respectively. Red lines indicate the calculated dispersion assuming complex-valued frequency where $w^{-1} = 2q/(\pi - \alpha_{\text{vis,IR}})$ and $\alpha_{\text{vis}} = -0.12\pi$, $\alpha_{\text{IR}} = -0.3\pi$.

a mode splitting at visible frequencies of $\Omega_{\text{vis},1} = 1.1 \times 10^3 \text{ cm}^{-1} \approx 0.14 \text{ eV}$ (between the lower and middle polariton branches) and $\Omega_{\text{vis},2} = 3 \times 10^3 \text{ cm}^{-1} \approx 0.37 \text{ eV}$ (between the middle and upper polariton branches). Considering the linewidths of the coupled states in the mid-IR frequency range, $\Gamma_{\text{IR},+,-} = 4 \text{ cm}^{-1} \approx 5 \times 10^{-4} \text{ eV}$, and the linewidths in the visible frequency range, $\Gamma_{\text{vis},1,-,0} = 1.5 \times 10^3 \text{ cm}^{-1} \approx 0.19 \text{ eV}$ and $\Gamma_{\text{vis},2,0,+} = 1.7 \times 10^3 \text{ cm}^{-1} \approx 0.21 \text{ eV}$, we find that the strong coupling criterion, $\Omega > (\Gamma_+ + \Gamma_-)/2$, is fulfilled both at mid-IR frequencies and for the “0” and “+” branches at visible frequencies.

4.5.3 Mode splitting from experimental extinction spectra

To determine the dispersion of the quasi-normal modes and extract the value of the mode splitting from the experimental data, we fitted our extinction spectra in Fig. 4.5b,e using a classical model of coupled harmonic oscillators (see Section 2.2): two coupled oscillators in the mid-IR frequency range and three coupled oscillators in the visible frequency range, respectively. We note, that in the mid-IR frequency range two oscillators represent the PhP and molecular vibration, and in the visible frequency range the three oscillators represent the SPP and two excitons. The coupled harmonic oscillator models allows us to reproduce the experimental extinction spectra by fitting the parameters of the uncoupled oscillators and the coupling strengths for each nanoresonator structure. With the parameters extracted from the fits we can calculate the dispersion of the quasi-normal modes of the coupled system and extract the mode splitting. The comparison between experimental and calculated dispersions in Section 4.5.2 is shown further in Fig. 4.9.

Mid-IR frequency range

In order to analyze the extinction spectra shown in Fig. 4.5a, we phenomenologically described the coupling between the molecular vibration and the phonon polaritons via a model of classical coupled harmonic oscillators [13, 136, 185]. The equations describing the motion of two coupled harmonic oscillators are given by:

$$\begin{cases} \ddot{x}_1(t) + \Gamma_1 \dot{x}_1(t) + \omega_1^2 x_1(t) - 2g \dot{x}_{\text{PhP}}(t) = F_1(t) \\ \ddot{x}_{\text{PhP}}(t) + \Gamma_{\text{PhP}} \dot{x}_{\text{PhP}}(t) + \omega_{\text{PhP}}^2 x_{\text{PhP}}(t) + 2g \dot{x}_1(t) = F_{\text{PhP}}(t) \end{cases} \quad (4.1)$$

where x_{PhP} , ω_{PhP} and Γ_{PhP} represent the displacement, frequency and linewidth of the PhP mode, respectively. x_1 , ω_1 and Γ_1 represent the displacement, frequency and linewidth of the molecular vibration of CoPc, respectively. F_{PhP} and F_1 represent the effective external forces that drive the motion of the oscillators. In the realistic electromagnetic problem the external electromagnetic field is the analog of the effective forces. g represents the coupling strength between PhP mode and CoPc molecular vibration. From the oscillators model we can construct a quantity equivalent to the extinction, C_{ext} , of the analogous electromagnetic problem. It can be calculated as the average power from the external forces according to $C_{\text{ext}} \propto \langle F_{\text{PhP}}(t) \dot{x}_{\text{PhP}}(t) + F_1(t) \dot{x}_1(t) \rangle$ [13, 138].

We fit C_{ext} to the measured extinction spectra of nanoresonator heterostructure with different ribbon width. Fits were performed according to $1 - \frac{T}{T_0} = C_{\text{ext}} + \text{Offset}$. In the fitting procedure, we take the same value of $\Gamma_1 = 6 \text{ cm}^{-1}$ as we used in the CoPc dielectric function. ω_1 was limited within a few wavenumbers from its initial value according to the

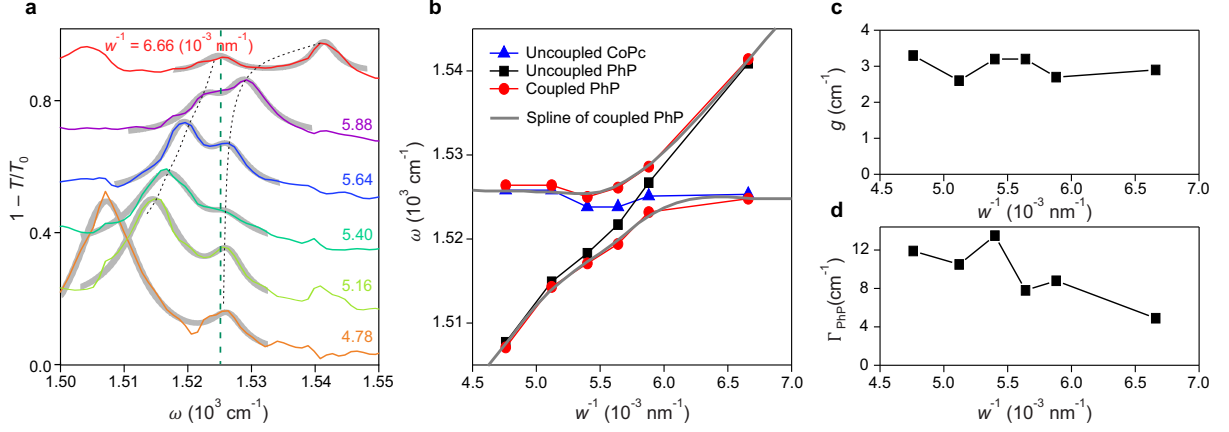


Figure 4.7: Coupled oscillators fit: mid-IR range. **a**, Experimental extinction spectra of the polaritonic nanoresonators loaded with the molecular layer. Green dashed line indicates the resonance frequency of the molecular vibration. Black dashed lines are guides to the eyes indicating the resonance features in the extinction spectra corresponding to the coupled polaritonic mode. Thick grey lines in **a** represent fits using a three and two coupled harmonic oscillators model, respectively. **b**, Uncoupled frequencies of PhPs: ω_{PhP} , and CoPc: ω_1 (blue triangles and black squares, respectively), as extracted from the fits. Frequencies of the quasi-normal modes calculated according to Eq. 4.2 (red circles). Grey solid lines show the spline of the eigenmodes frequencies as a function of inverse width of ribbons **c**, Black symbols show the coupling strength from the fits. **d**, The linewidth of uncoupled PhPs from the fits.

CoPc dielectric function ($\omega_1 = \omega_{\text{CoPc}} = 1524.8 \text{ cm}^{-1}$), to allow for an eventual Lamb shift of the molecular vibration [158, 159]. ω_{PhP} , g , $F_{1,\text{PhP}}$ and Γ_{PhP} were considered as free parameters in all fits. The extracted values of the coupling strength for each fits are plotted as black symbols in the Fig. 4.7c. With the parameters extracted from the fits we calculated the frequencies of the quasi-normal modes of the coupled system. The eigenfrequencies can be found from the dispersion relation, which arises from equaling the determinant of the system 4.1 to zero [160] (assuming the harmonic time-dependence of the displacements, $e^{-i\omega t}$):

$$\omega_{\pm} + i\frac{\Gamma_{\pm}}{2} = \frac{\omega_{\text{PhP}} + \omega_1}{2} - i\frac{\Gamma_{\text{PhP}} + \Gamma_1}{4} \pm \frac{1}{2} \sqrt{4g^2 + \left(\omega_{\text{PhP}} - \omega_1 - i\frac{\Gamma_{\text{PhP}} - \Gamma_1}{2} \right)^2}. \quad (4.2)$$

We have used the approximation $\omega - \omega_j \ll \omega_j$, so that $\omega^2 - \omega_j^2 = 2\omega_j(\omega - \omega_j)$, with $j=1$, PhP. Fig. 4.7a shows the calculated frequencies quasi-normal modes ω_{\pm} as a function of inverse width of nanoresonators, $1/w$. To find the mode splitting we first splined the real part of the calculated frequency of the quasi-normal modes (gray lines in Fig. 4.7b) and then found the smallest vertical separation between the splined branches, $\Omega_{\text{IR}} = 5.9 \text{ cm}^{-1}$. All the fitting parameters are presented in Table 4.2.

$1/w, 10^{-3}$ nm^{-1}	$\omega_1,$ cm^{-1}	$F_1,$ cm^{-2}	$\omega_{\text{PhP}},$ cm^{-1}	$\Gamma_{\text{PhP}},$ cm^{-1}	$F_{\text{PhP}},$ cm^{-2}	$g,$ cm^{-1}	<i>Offset</i>
4.8	1525.8	1.13	1507.7	11.9	2.16	3.3	-0.38
5.2	1525.8	1.21	1514.9	10.5	1.54	2.6	-0.19
5.4	1523.8	0.06	1518.3	13.5	1.82	3.2	0.07
5.6	1523.8	0	1521.7	7.8	1.46	3.2	0.09
5.9	1525.1	0	1526.7	8.8	1.37	2.7	0.1
6.7	1525.3	0.4	1540.9	4.9	0.75	2.9	0.1

Table 4.2: Parameters of the coupled oscillators model to fit the experimental extinctions spectra in the mid-IR frequency range.

Visible frequency range

In order to analyze the extinction spectra in the visible frequency range in Fig. 4.5a, we phenomenologically described the coupling of the excitons and the SPPs via a classical model of three coupled harmonic oscillators, where we considered the coupling only between the SPP and two excitons. The equations of motion for the three coupled harmonic oscillators are given by:

$$\begin{cases} \ddot{x}_1(t) + \Gamma_1 \dot{x}_1(t) + \omega_1^2 x_1(t) - 2g_1 \dot{x}_{\text{PhP}}(t) = F_1(t) \\ \ddot{x}_2(t) + \Gamma_2 \dot{x}_2(t) + \omega_2^2 x_2(t) - 2g_2 \dot{x}_{\text{PhP}}(t) = F_2(t) \\ \ddot{x}_{\text{PhP}}(t) + \Gamma_{\text{PhP}} \dot{x}_{\text{PhP}}(t) + \omega_{\text{PhP}}^2 x_{\text{PhP}}(t) + 2g_1 \dot{x}_1(t) + 2g_2 \dot{x}_2(t) = F_{\text{PhP}}(t) \end{cases} \quad (4.3)$$

where $x_{\text{SPP}}, \omega_{\text{SPP}}$ and Γ_{SPP} represent the displacement, frequency and linewidth of the SPP mode, respectively. $x_{1,2}, \omega_{1,2}$ and $\Gamma_{1,2}$ represent the displacement, frequency and linewidth of the “1” and “2” excitons of CoPc, respectively. F_{SPP} and $F_{1,2}$ represent the effective forces that drive their motions. g_1 represents the coupling strength between SPP mode and CoPc exciton “1”, g_2 represents the coupling strength between SPP mode and CoPc exciton “2”. Analogously to the mid-IR range, from the oscillators model we can construct a quantity equivalent to the extinction, C_{ext} , that can be calculated according to $C_{\text{ext}} \propto \langle F_{\text{SPP}}(t) \dot{x}_{\text{SPP}}(t) + F_1(t) \dot{x}_1(t) + F_2(t) \dot{x}_2(t) \rangle$.

We fit C_{ext} to the measured extinction spectra of nanoresonator heterostructures with different ribbon width. Fits were performed according to $1 - \frac{T}{T_0} = C_{\text{ext}} + \text{Offset}$. In the fitting procedure, we take the same value of $\Gamma_{\text{CoPc},1} = 1739 \text{ cm}^{-1}$ and $\Gamma_{\text{CoPc},2} = 2369 \text{ cm}^{-1}$ as we used in the CoPc dielectric function. To minimize the number of fitting parameters in the visible frequency range, we fix the uncoupled frequencies of excitons $\omega_1 = \omega_{0,1} = 14402 \text{ cm}^{-1}$ and $\omega_2 = \omega_{0,2} = 16264 \text{ cm}^{-1}$ according to the CoPc dielectric function. $\omega_{\text{SPP}},$

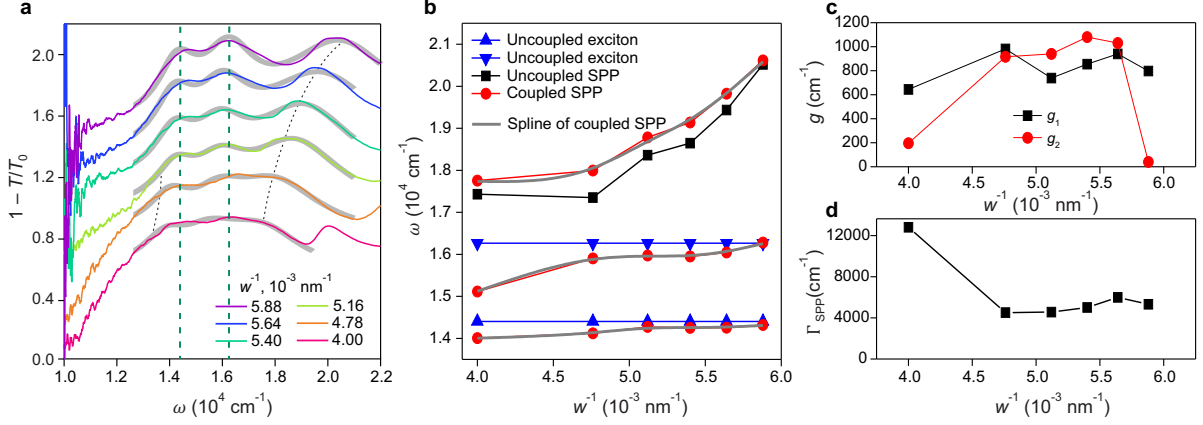


Figure 4.8: Coupled oscillators fit: visible range. **a**, Experimental extinction spectra of the polaritonic nanoresonators loaded with the molecular layer. Green dashed lines indicate the resonance frequencies of the molecular excitons. Black dashed lines are guides to the eyes indicating the resonance features in the extinction spectra corresponding to the coupled polaritonic modes. Thick grey lines in **a** represent fits using a three and two coupled harmonic oscillators model, respectively. **b**, Uncoupled frequencies of SPPs, ω_{SPP} , and CoPc excitons, $\omega_{1,2}$, (black squares and blue triangles, respectively) as extracted from the fits. Red circles show the eigenmode frequencies. Grey solid lines show the spline of the eigenmode frequencies as a function of inverse width of ribbons **c**, Black symbols show the coupling strength from the fits. **d**, The linewidth of uncoupled SPPs from the fits.

$g_{1,2}$, $F_{1,2,\text{SPP}}$ and Γ_{SPP} were considered as free parameters in all fits. The extracted values of the coupling strengths for each fits are plotted as black and red symbols in the Fig. 4.8c.

$1/w, 10^{-3} \text{ nm}^{-1}$	$F_1, \text{ cm}^{-2}$	$F_2, \text{ cm}^{-2}$	$\omega_{\text{SPP}}, \text{ cm}^{-1}$	$\Gamma_{\text{SPP}}, \text{ cm}^{-1}$	$F_{\text{SPP}}, \text{ cm}^{-2}$	$g_1, \text{ cm}^{-1}$	$g_2, \text{ cm}^{-1}$	<i>Offset</i>
4.0	1600.7	100.2	17430	12801	15999	644.3	196.4	-0.25
4.8	1668.5	3000	17352	4515	5335	982	915.9	0.54
5.2	1969.2	3073.7	18360	4552.7	6323	739.3	940	0.45
5.4	2100.3	3504.3	18646	5006.3	7190	854.4	1080.3	0.35
5.6	2397.8	3947.8	19434	5987.8	8430	939.9	1030.6	0.25
5.9	2857	3997	20523	5317.9	7878	797.3	40	0.24

Table 4.3: Parameters of the coupled oscillators model to fit the experimental extinctions spectra in the visible frequency range.

With the parameters extracted from the fits we numerically calculated the three frequencies of the quasi-normal modes of the coupled system. The eigenfrequencies can be found from the dispersion relation, which arises from equaling the determinant of the system 4.3 to zero (assuming the harmonic time-dependence of the displacements, $e^{-i\omega t}$). Fig. 4.8b shows the three branches (red circles) of the real part of calculated frequencies of quasi-normal modes as a function of inverse width of the nanoresonators, $1/w$. To find the mode splitting, analogously to the mid-IR range, we first splined the real part of calculated frequencies of quasi-normal modes (gray lines in Fig. 4.8b) and then extracted the

smallest vertical separation between the adjacent splined branches $\Omega_{\text{vis},1} = 1.1 \times 10^3 \text{ cm}^{-1}$ (between the lower and middle polariton branches) and $\Omega_{\text{vis},2} = 3 \times 10^3 \text{ cm}^{-1}$ (between the middle and upper polariton branches). All the fitting parameters are presented in Table 4.3.

Comparison of experimental and calculated mode splitting

In both spectral ranges, we find that the dispersion of the quasi-normal modes exhibits anti-crossing, as clearly shown by the squares in Fig. 4.9a,b. In the mid-IR range, the minimum vertical distance between the dispersion branches of the modes yields a mode splitting of $\Omega_{\text{IR}} = 6.0 \text{ cm}^{-1} \approx 7.3 \times 10^{-4} \text{ eV}$. In the visible spectral range, we find two mode splittings of $\Omega_{\text{vis},1} = 1.1 \times 10^3 \text{ cm}^{-1} \approx 0.14 \text{ eV}$ (between the lower and middle polariton branches) and $\Omega_{\text{vis},2} = 2.1 \times 10^3 \text{ cm}^{-1} \approx 0.26 \text{ eV}$ (between the middle and upper polariton branches). Thus, the extracted dispersions of the quasi-normal modes and the values of the mode splittings are in good agreement with the corresponding theoretical values for the continuous heterostructure in the mid-IR and visible spectral ranges (dashed red lines in Fig. 4.9a,b) at the values of w^{-1} corresponding to the fabricated structures (white vertical dashed lines in Fig. 4.9a,b). We note that the linewidths of the quasi-normal modes extracted from the fits in both frequency ranges are about 2 – 6 times larger than those calculated theoretically and vary for different structures, so that only the SC onset is reached. We explain this discrepancy by fabrication uncertainties and width variation along the Al ribbons, fabrication-induced roughness, defects, and the presence of higher order PhP modes in h-BN slab.

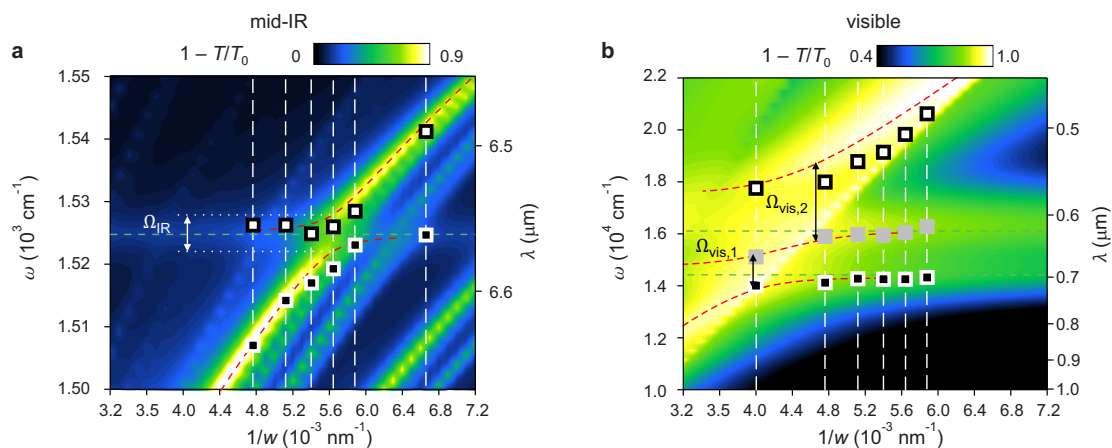


Figure 4.9: Comparison between experimental and calculated quasi-normal modes. **a,b**, Colour plots showing the simulated extinction of the nanoresonators in the mid-IR and visible frequency ranges, respectively (the same as in the Fig. 4.6). Red lines indicate the calculated dispersion assuming complex-valued frequency where $w^{-1} = 2q/(\pi - \alpha_{\text{vis,IR}})$ and $\alpha_{\text{vis}} = -0.12\pi$, $\alpha_{\text{IR}} = -0.3\pi$. **a** The white and black squares represent the dispersion of the quasi-normal modes of the nanoresonators calculated using parameters obtained from the coupled oscillators fit in Fig. 4.7. **b** The white, grey and black squares represent the dispersion of the quasi-normal modes of the nanoresonators calculated using parameters obtained from the coupled oscillators fit in Fig. 4.8.

4.6 Mode splitting dependence on molecular layer thickness

Finally, we analyze theoretically the coupling strength between the M1 PhP mode and the molecular vibrations, as well as between the SPP mode and the excitons. To that end, we extracted the mode splitting Ω for continuous heterostructures with different molecular layer thickness d_{CoPc} from the previously developed quasi-normal analysis. We find that the mode splitting, and thus the coupling strength between polaritons and molecular excitations, increases with d_{CoPc} in both visible and mid-IR frequency ranges (Fig. 4.10b,c). This result is explained by a larger portion of the electromagnetic field of the polaritonic modes inside the molecular layer for larger thicknesses (Fig. 4.10a) [186, 187]. Furthermore, we find that the mode splitting reaches saturation for a thickness of 60 nm, which is due to the full confinement of the PhP field inside the molecular layer (the field does not reach the air region). Interestingly, in the visible frequency range, the SC criterion is not fulfilled for the first exciton excitation even for a molecular layer thickness of 100 nm, while for the second excitonic excitation, the SC criterion is fulfilled for molecule layers thicker than 20 nm. In contrast, in the mid-IR range, the numerical calculations predict the observation of SC already for molecule layers as thin as 15 nm.

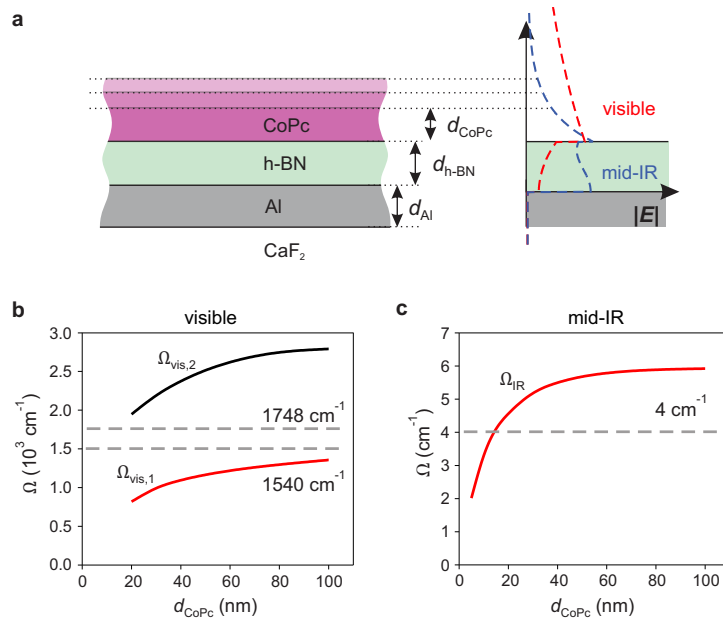


Figure 4.10: Mode splitting dependence on molecular layer thickness. **a**, Schematic illustration of the Al/h-BN/CoPc heterostructure. Right: calculated electric field distribution in the heterostructure at $\omega = 1530 \text{ cm}^{-1}$ (blue dashed curve) and $\omega = 19500 \text{ cm}^{-1}$ (red dashed curve). **b,c**, Calculated mode splitting as a function of the molecular layer thickness in the visible and mid-IR frequency ranges. The square symbols in **c** are mode splitting extracted from the measured spectra. The Al and h-BN thicknesses are $d_{\text{Al}} = 50 \text{ nm}$, and $d_{\text{h-BN}} = 75$. Horizontal dashed lines separate the regions of the strong and weak coupling. SC in both bands is observed for CoPc thicknesses larger than about 15 nm.

4.7 Conclusion

Our work demonstrates that engineering a heterostructure composed of plasmonic and phononic materials allows simultaneous access to light-matter interactions in the visible and mid-IR frequencies. Such heterostructure can be exploited to achieve dual-band strong light matter coupling, namely between nanoscale confined polaritons (SPPs and PhPs) and electronic or vibrational excitations of molecules. Momentum-energy coupling between excitations and polaritons can be achieved by tuning the dispersion of the latter through the thickness of the layers in the heterostructure. Future dual-band SC experiments may offer novel opportunities for manipulating chemical reactions, advanced optical imaging and sensing, or optomechanical up-conversion.

4.8 Supplementary information

4.8.1 Dielectric function of materials

CoPc dielectric function in the infrared frequency range

We measured the relative infrared transmission spectrum of a 100 nm thick Cobalt(II) Phthalocyanine (CoPc) layer evaporated on top of a CaF₂ substrate. To extract the dielectric function of the CoPc molecules we calculate the relative transmission spectra, T/T_0 , for the three layer system, using Fresnel coefficients, where T is transmission through CaF₂/CoPc and T_0 is transmission through the CaF₂ substrate ($\epsilon_{\text{CaF}_2} = 1.37$ in the considered infrared frequency range).

We modeled the dielectric function of the CoPc molecules by the Drude-Lorentz model assuming one classical harmonic oscillator to describe molecular vibrations in the considered infrared frequency range, as follows:

$$\epsilon_{\text{CoPc}}(\omega) = \epsilon_{\infty, \text{IR}} + \frac{S}{\omega_0^2 - \omega^2 - i\Gamma_{\text{CoPc}}\omega}, \quad (4.4)$$

where $\epsilon_{\infty, \text{IR}}$ is a high-frequency dielectric constant, S is a constant that is proportional to the effective strength of the Lorentz oscillator, ω_0 and Γ_{CoPc} represent the central frequency and the linewidth of the Lorentz oscillator, respectively. Fit yields $\epsilon_{\infty, \text{IR}} = 2.8 \text{ cm}^{-1}$, $S = 3600 \text{ cm}^{-2}$, $\omega_0 = 1524.8 \text{ cm}^{-1}$, $\Gamma_{\text{CoPc}} = 6 \text{ cm}^{-1}$. With the parameters extracted from the fit, we are able to calculate the dielectric permittivity of CoPc molecules in the infrared frequency range, according to Eq. 4.4.

CoPc dielectric function in the visible frequency range

Following the same procedure as in the infrared frequency range, we measured the relative transmission spectrum for 20, 30, 50 and 100 nm thick Cobalt(II) Phthalocyanine (CoPc) layers evaporated on top of a CaF₂ substrate ($\epsilon_{\text{CaF}_2} = 1.43$ in the considered visible frequency range). To extract the dielectric function of the CoPc molecules we used relative transmission spectra, T/T_0 calculated with the help of Fresnel coefficients.

We fit the dielectric function of the CoPc molecules by the Drude-Lorentz model assuming two classical harmonic oscillators to describe electronic transitions in visible frequency range, as follows:

$$\varepsilon_{\text{CoPc}}(\omega) = \varepsilon_{\infty,\text{vis}} + \frac{S_1}{\omega_{0,1}^2 - \omega^2 - i\Gamma_{\text{CoPc},1}\omega} + \frac{S_2}{\omega_{0,2}^2 - \omega^2 - i\Gamma_{\text{CoPc},2}\omega}, \quad (4.5)$$

where $\varepsilon_{\infty,\text{vis}}$ is a high-frequency dielectric constant, S_k ($k = 1, 2$) are constants proportional to the effective strength of the k th Lorentz oscillator, $\omega_{0,k}$ and $\Gamma_{\text{CoPc},k}$ represent the central frequency and the linewidth of the k th Lorentz oscillator, respectively.

We fitted the relative transmission spectrum for each thickness of the molecular layer independently and then averaged the extracted fit parameters. The averaged fit parameters: $\varepsilon_{\infty,\text{vis}} = 1.6 \text{ cm}^{-1}$, $\omega_{0,1} = 14402 \text{ cm}^{-1}$, $S_1 = 31539456 \text{ cm}^{-2}$, $\Gamma_{\text{CoPc},1} = 1739 \text{ cm}^{-1}$, $\omega_{0,2} = 16264 \text{ cm}^{-1}$, $S_2 = 65755881 \text{ cm}^{-2}$, $\Gamma_{\text{CoPc},2} = 2369 \text{ cm}^{-1}$.

h-BN dielectric function

We used the isotopically (^{10}B) enriched h-BN [80]. The dielectric permittivity tensor of h-BN is modeled according to the following formula:

$$\varepsilon_{\text{h-BN},j}(\omega) = \varepsilon_{\infty,j} \left(\frac{\omega_{\text{LO},j}^2 - \omega^2 - i\omega\Gamma_j}{\omega_{\text{TO},j}^2 - \omega^2 - i\omega\Gamma_j} \right), \quad (4.6)$$

where $j = \perp, \parallel$ indicates the component of the tensor perpendicular and parallel to the anisotropy axis. We took the parameters for the dielectric function of h-BN from ref. 80 except of ε_{∞} . For the best matching of our near-field and far-field experiments we took $\varepsilon_{\infty} = 4$ instead of $\varepsilon_{\infty} = 5.1$ in ref. 80. We attribute the discrepancy to fabrication material parameter uncertainties. All parameters for the dielectric function, which were used in the simulation, are presented in the Table 4.4.

j	ε_{∞}	$\omega_{\text{TO}}, \text{ cm}^{-1}$	$\omega_{\text{LO}}, \text{ cm}^{-1}$	$\Gamma, \text{ cm}^{-1}$
\perp	4	1394.5	1650	1.8
\parallel	2.5	785	845	1

Table 4.4: Parameters of the Eq. 4.6 of the dielectric function of h-BN.

Al dielectric function

We modelled the Al dielectric function as a sum of Drude and Lorentz terms using parameters from the ref. 183.

4.8.2 Data processing of the nanoimaging experiments

Mid-IR frequency range

In Section 4.4.1, we performed nanoimaging experiments of the nanoresonator heterostructure. In the top panel in Fig. 4.3e in Section 4.4.1, we showed the near-field image post data processing. Here, we detail the data processing procedure that was conducted. Fig. 4.11c,e,g show the raw amplitude, phase and real part (calculated using the amplitude and phase) of the complex-valued s-SNOM signal, σ_3 . The data is represented as near-field images – the signal as a function of the tip position above the sample – of the set of 4 nanoresonators, which is schematically shown in Fig. 4.11a,b. In order to reveal the mode field pattern above the nanoresonators, we subtracted the mean value of both the real and imaginary parts of signal for each horizontal line profile at the fixed y coordinate. Fig. 4.11d,f,g show the final data set of amplitude, phase and real part of the near-field images, $\sigma_3^*(x, y)$, after the subtraction of the mean values. The top panel in Fig. 4.3e in Section 4.4.1 shows the final data of real part of the first resonator of Fig. 4.11h, for $x \in [0 : 0.5] \mu\text{m}$.

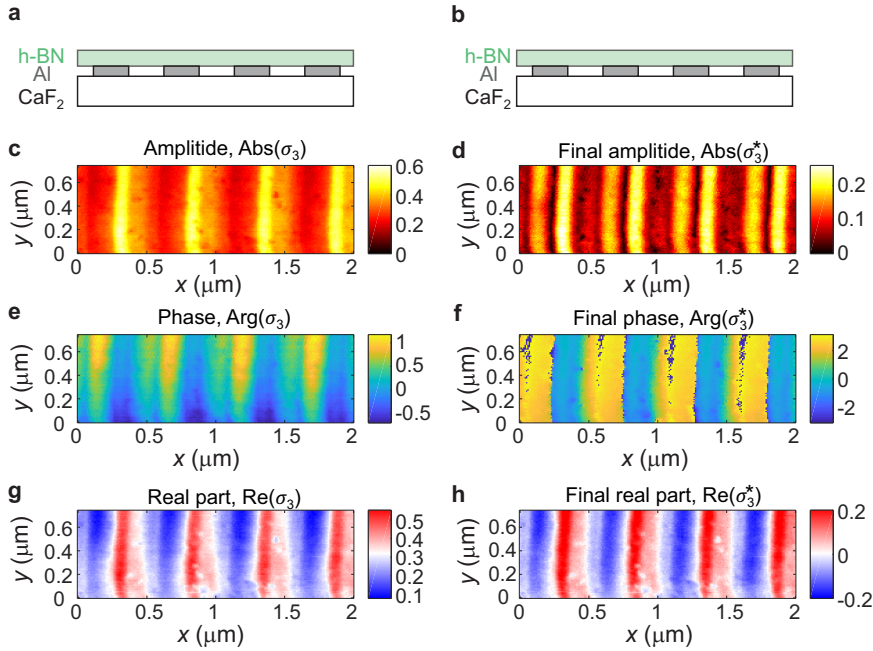


Figure 4.11: Mean value subtraction from the near-field data in the mid-IR frequency range. **a,b**, Schematics of the measured nanoresonator heterostructure. **c,e,g**, Raw amplitude, phase and real part of the near-field images of 4 nanoresonators, as indicated in the panels **a,b** in the mid-IR frequency range, measured at $\omega_{\text{mid-IR}} = 1510 \text{ cm}^{-1}$, respectively. **d,f,h**, The resulting amplitude, phase and real part of the near-field images after the mean value subtraction, respectively.

Visible frequency range

In Section 4.4.1, we performed nanoimaging experiments of the nanoresonator heterostructure. In the top panel in Fig. 4.3f in Section 4.4.1, we showed the near-field image post data processing. Here, we detail the data processing procedure that was conducted. Fig. 4.12c,e,g show the raw amplitude, phase and real part (calculated using the amplitude and phase images) of the complex-valued s-SNOM signal, σ_3 . Analogously to the mid-IR range, the near-field images are shown for the set of 4 nanoresonators, which is schematically shown in Fig. 4.12a,b. We also analogously subtracted the mean value of both the real and imaginary parts of signal for each horizontal line profile at the fixed y coordinate. Then we removed the propagating SPP Bloch mode by subtraction the complex signal $\sigma_B(x) = A_B e^{iGx + \varphi_B}$ for each y coordinate, where $A_B = 0.075$, $\varphi_B = 0.25\pi$ are real-valued fitting parameters and $G = \frac{2\pi}{p}$ is the Bragg vector of the array of Al ribbons with the period $p = 500$ nm. Fig. 4.12d,f,g show the final data set of the amplitude, phase and real part of the near-field images, $\sigma_3^*(x, y)$, after the subtraction of the mean values and propagating SPP Bloch mode. The top panel in Fig. 4.3f in Section 4.4.1 shows the final data of the real part of the first resonator of Fig. 4.12h, for $x \in [0 : 0.5] \mu\text{m}$.

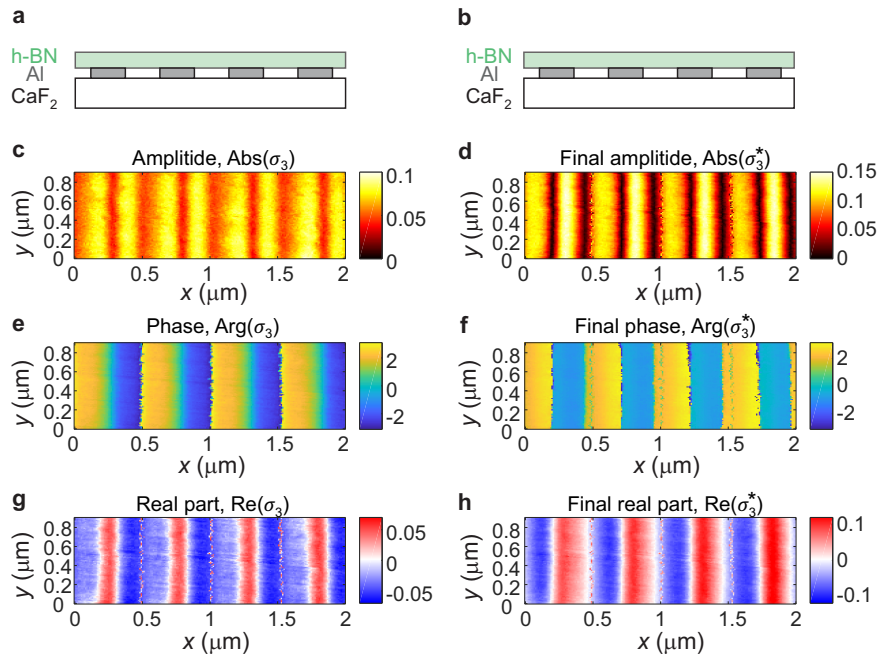


Figure 4.12: Mean value and SPP Bloch mode subtraction from the near-field data in the visible frequency range. **a,b**, Schematics of the measured nanoresonator heterostructure. **c,e,g**, Raw amplitude, phase and real part of the near-field images of 4 nanoresonators, as indicated in the panels **a,b** in the visible frequency range, measured at $\omega_{\text{vis}} = 15798 \text{ cm}^{-1}$, respectively. **d,f,h**, The resulting amplitude, phase and real part of the near-field images, respectively.

List of Publications

This thesis is based on the following publications:

1. **A. Bylinkin**, M. Schnell, M. Autore, F. Calavalle, P. Li, J. Taboada-Gutitiérrez, S. Liu, J. H. Edgar, F. Casanova, L. E. Hueso, P. Alonso-González, A. Y. Nikitin and R. Hillenbrand. “Real-space observation of vibrational strong coupling between propagating phonon polaritons and organic molecules”, *Nat. Photonics* **15**, 197–202 (2021).

<https://doi.org/10.1038/s41566-020-00725-3>

2. **A. Bylinkin**, F. Calavalle, M. Barra-Burillo, R. V. Kirtaev, E. Nikulina, E. Modin, E. Janzen, J. H. Edgar, F. Casanova, L. E. Hueso, V. S. Volkov, P. Vavassori, I. Aharonovich, P. Alonso-González, R. Hillenbrand and A. Y. Nikitin. “Dual-band coupling of phonon and surface plasmon polaritons with vibrational and electronic excitations in molecules”, *Nano Lett.* **23.9**, 3985-3993 (2023).

<https://doi.org/10.1021/acs.nanolett.3c00768>

Other relevant publications that are not included in the text:

3. **A. Bylinkin**, S. Castilla, T. M. Slipchenko, K. L. Domina, F. Calavalle, V. Pusapati, M. Autore¹, F. Casanova, L. E. Hueso, L. Martín-Moreno, A. Y. Nikitin, F. Koppens and R. Hillenbrand. “On-chip phonon-enhanced IR near-field detection of molecular vibrations”. *Submitted*.
4. E. Calandrini, K. Voronin, O. Balci, M. B. Burillo, **A. Bylinkin**, S. M. Shinde, S. Sharma, F. Casanova, L. E. Hueso, A. Chuvilin, C. McAleese, B. R. Conran, X. Wang, T. Kenneth, V. S. Volkov, A. C. Ferrari, A. Y. Nikitin and R. Hillenbrand. “Near- and far-field Observation of phonon polaritons in wafer-scale multilayer hexagonal boron nitride prepared by chemical vapor deposition”, *Advanced Materials*, 2302045 (2023)

<https://doi.org/10.1002/adma.202302045>.

-
5. I. Dolado, C. Maciel-Escudero, E. Nikulina, E. Modin, F. Calavalle, S. Chen, **A. Bylinkin**, F. J. Alfaro-Mozaz, J. Li, J. H. Edgar, F. Casanova, S. Vélez, L. E. Hueso, R. Esteban, J. Aizpurua and R. Hillenbrand. “Remote near-field spectroscopy of vibrational strong coupling between organic molecules and phononic nanoresonators”, *Nat. Commun.* **13**, 6850 (2022)
<https://doi.org/10.1038/s41467-022-34393-4>
 6. S. Chen, **A. Bylinkin**, Z. Wang, M. Schnell, G. Chandan, P. Li, A. Y. Nikitin, S. Law and R. Hillenbrand. “Real-space nanoimaging of THz polaritons in the topological insulator Bi₂Se₃”, *Nat. Commun.* **13**, 1374 (2022)
<https://doi.org/10.1038/s41467-022-28791-x>
 7. J. Duan, F. J. Alfaro-Mozaz, J. Taboada-Gutiérrez, I. Dolado, G. Álvarez-Pérez, E. Titova, **A. Bylinkin**, A. I.F. Tresguerres-Mata, J. Martín-Sánchez, S. Liu, J. H. Edgar, D. A. Bandurin, P. Jarillo-Herrero, A. Y. Nikitin and P. Alonso-González. “Active and passive tuning of ultranarrow resonances in polaritonic nanoantennas”, *Advanced Materials* **34.10**, 2104954 (2022)
<https://doi.org/10.1002/adma.202104954>
 8. D. Virmani, **A. Bylinkin**, I. Dolado, E. Janzen, J. H. Edgar and R. Hillenbrand. “Amplitude- and Phase-Resolved Infrared Nanoimaging and Nanospectroscopy of Polaritons in a Liquid Environment”, *Nano Lett.* **21.3**, 1360–1367 (2021)
<https://doi.org/10.1021/acs.nanolett.0c04108>
 9. J. Duan, G. Álvarez-Pérez, A. I.F. Tresguerres-Mata, J. Taboada-Gutiérrez, K. V. Voronin, **A. Bylinkin**, B. Chang, S. Xiao, S. Liu, J. H. Edgar, J. I. Martín, V. S. Volkov, R. Hillenbrand, J. Martín-Sánchez, R. Hillenbrand, A. Y. Nikitin and P. Alonso-González. “Planar refraction and lensing of highly confined polaritons in anisotropic media”, *Nat. Commun.* **12**, 4325 (2021)
<https://doi.org/10.1038/s41467-021-24599-3>
 10. G. A. Ermolaev, D. V. Grudin, Y. V. Stebunov, K. V. Voronin, V. G. Kravets, J. Duan, A. B. Mazitov, G. I. Tselikov, **A. Bylinkin**, D. I. Yakubovsky, S. M. Novikov, D. G. Baranov, A. Y. Nikitin, I. A. Kruglov, T. Shegai, P. Alonso-González, A. N. Grigorenko, A. V. Arsenin, K. S. Novoselov and V. S. Volkov. “Giant optical anisotropy in transition metal dichalcogenides for next-generation photonics”, *Nat. Commun.* **12**, 854 (2021)
<https://doi.org/10.1038/s41467-021-21139-x>

11. J. Taboada-Gutiérrez, G. Álvarez-Pérez, J. Duan, W. Ma, K. Crowley, I. Prieto, **A. Bylinkin**, M. Autore, H. Volkova, K. Kimura, T. Kimura, M.-H. Berger, S. Li, Q. Bao, X. P.A. Gao, I. Errea, A. Y. Nikitin, R. Hillenbrand., J. Martín-Sánchez and P. Alonso-González. “Broad spectral tuning of ultra-low-loss polaritons in a van der Waals crystal by intercalation”, *Nat. Mater.* **19**, 964–968 (2020)
<https://doi.org/10.1038/s41563-020-0665-0>.
12. G. Álvarez-Pérez, T. G Folland, I. Errea, J. Taboada-Gutiérrez, J. Duan, J. Martín-Sánchez, A. I.F. Tresguerres-Mata, J. R. Matson, **A. Bylinkin**, M. He, W. Ma, Q. Bao, J. I. Martín, J. D. Caldwell, A. Y. Nikitin and P. Alonso-González. “Infrared permittivity of the biaxial van der Waals semiconductor α -MoO₃ from near- and far-field correlative studies”, *Advanced Materials* **32.29**, 1908176 (2020)
<https://doi.org/10.1002/adma.201908176>
13. I. Dolado, F. J. Alfaro-Mozaz, P. Li, E. Nikulina, **A. Bylinkin**, S. Liu, J. H. Edgar, F. Casanova, L. E. Hueso, P. Alonso-González, S. Vélez, A. Nikitin and R. Hillenbrand. “Nanoscale guiding of infrared light with hyperbolic volume and surface polaritons in van der Waals material ribbons”, *Advanced Materials* **32.9**, 1906530 (2020)
<https://doi.org/10.1002/adma.201906530>
14. **A. Bylinkin**, E. Titova, V. Mikheev, E. Zhukova, S. Zhukov, M. Belyanchikov, M. Kashchenko, A. Miakonkikh and D. Svintsov. “Tight-binding berahertz blasmons in chemical-vapor-deposited graphene”, *Phys. Rev. Applied* **11**, 054017 (2019).
<https://doi.org/10.1103/PhysRevApplied.11.054017>

Bibliography

- [1] P. Törmä and W. L. Barnes, “Strong coupling between surface plasmon polaritons and emitters: a review,” *Reports on Progress in Physics*, vol. 78, no. 1, p. 013901, 2014.
- [2] E. Orgiu, J. George, J. Hutchison, E. Devaux, J. Dayen, B. Doudin, F. Stellacci, C. Genet, J. Schachenmayer, C. Genes, *et al.*, “Conductivity in organic semiconductors hybridized with the vacuum field,” *Nature Materials*, vol. 14, no. 11, pp. 1123–1129, 2015.
- [3] D. Hagenmüller, J. Schachenmayer, S. Schütz, C. Genes, and G. Pupillo, “Cavity-enhanced transport of charge,” *Physical review letters*, vol. 119, no. 22, p. 223601, 2017.
- [4] A. Thomas, L. Lethuillier-Karl, K. Nagarajan, R. M. Vergauwe, J. George, T. Chervy, A. Shalabney, E. Devaux, C. Genet, J. Moran, *et al.*, “Tilting a ground-state reactivity landscape by vibrational strong coupling,” *Science*, vol. 363, no. 6427, pp. 615–619, 2019.
- [5] J. A. Hutchison, T. Schwartz, C. Genet, E. Devaux, and T. W. Ebbesen, “Modifying chemical landscapes by coupling to vacuum fields,” *Angewandte Chemie International Edition*, vol. 51, no. 7, pp. 1592–1596, 2012.
- [6] B. Xiang, R. F. Ribeiro, M. Du, L. Chen, Z. Yang, J. Wang, J. Yuen-Zhou, and W. Xiong, “Intermolecular vibrational energy transfer enabled by microcavity strong light–matter coupling,” *Science*, vol. 368, no. 6491, pp. 665–667, 2020.
- [7] J. Yuen-Zhou, W. Xiong, and T. Shegai, “Polariton chemistry: Molecules in cavities and plasmonic media,” *The Journal of Chemical Physics*, vol. 156, no. 3, 2022.
- [8] G. L. Paravicini-Bagliani, F. Appugliese, E. Richter, F. Valmorra, J. Keller, M. Beck, N. Bartolo, C. Rössler, T. Ihn, K. Ensslin, *et al.*, “Magneto-transport controlled by landau polariton states,” *Nature Physics*, vol. 15, no. 2, pp. 186–190, 2019.

-
- [9] R. Ameling and H. Giessen, “Microcavity plasmonics: strong coupling of photonic cavities and plasmons,” *Laser & photonics reviews*, vol. 7, no. 2, pp. 141–169, 2013.
- [10] M. L. Tseng, H.-H. Hsiao, C. H. Chu, M. K. Chen, G. Sun, A.-Q. Liu, and D. P. Tsai, “Metalenses: advances and applications,” *Advanced Optical Materials*, vol. 6, no. 18, p. 1800554, 2018.
- [11] A. John-Herpin, A. Tittl, L. Kühner, F. Richter, S. H. Huang, G. Shvets, S.-H. Oh, and H. Altug, “Metasurface-enhanced infrared spectroscopy: An abundance of materials and functionalities,” *Advanced Materials*, vol. 35, no. 34, p. 2110163, 2023.
- [12] W. Ji, H. Zhao, H. Yang, and F. Zhu, “Effect of coupling between excitons and gold nanoparticle surface plasmons on emission behavior of phosphorescent organic light-emitting diodes,” *Organic Electronics*, vol. 22, pp. 154–159, 2015.
- [13] M. Autore, P. Li, I. Dolado, F. J. Alfaro-Mozaz, R. Esteban, A. Atxabal, F. Casanova, L. E. Hueso, P. Alonso-González, J. Aizpurua, A. Y. Nikitin, *et al.*, “Boron nitride nanoresonators for phonon-enhanced molecular vibrational spectroscopy at the strong coupling limit,” *Light: Science & Applications*, vol. 7, no. 4, pp. 17172–17172, 2018.
- [14] M. Autore, I. Dolado, P. Li, R. Esteban, F. J. Alfaro-Mozaz, A. Atxabal, S. Liu, J. H. Edgar, S. Vélez, F. Casanova, *et al.*, “Enhanced light–matter interaction in 10b monoisotopic boron nitride infrared nanoresonators,” *Advanced Optical Materials*, vol. 9, no. 5, p. 2001958, 2021.
- [15] R. Damari, O. Weinberg, D. Krotkov, N. Demina, K. Akulov, A. Golombek, T. Schwartz, and S. Fleischer, “Strong coupling of collective intermolecular vibrations in organic materials at terahertz frequencies,” *Nature Communications*, vol. 10, no. 1, p. 3248, 2019.
- [16] M. Kaeek, R. Damari, M. Roth, S. Fleischer, and T. Schwartz, “Strong coupling in a self-coupled terahertz photonic crystal,” *ACS Photonics*, vol. 8, no. 7, pp. 1881–1888, 2021.
- [17] D. N. Basov, M. M. Fogler, and J. García de Abajo, “Polaritons in van der waals materials,” *Science*, vol. 354, no. 6309, p. aag1992, 2016.
- [18] T. Low, A. Chaves, J. D. Caldwell, A. Kumar, N. X. Fang, P. Avouris, T. F. Heinz, F. Guinea, L. Martin-Moreno, and F. Koppens, “Polaritons in layered two-dimensional materials,” *Nat. Mater.*, vol. 16, pp. 182–194, 2017.
- [19] Z. Fei, A. Rodin, G. O. Andreev, W. Bao, A. McLeod, M. Wagner, L. Zhang, Z. Zhao, M. Thiemens, G. Dominguez, *et al.*, “Gate-tuning of graphene plasmons

- revealed by infrared nano-imaging,” *Nature*, vol. 487, no. 7405, pp. 82–85, 2012.
- [20] J. Chen, M. Badioli, P. Alonso-González, S. Thongrattanasiri, F. Huth, J. Osmond, M. Spasenović, A. Centeno, A. Pesquera, P. Godignon, *et al.*, “Optical nano-imaging of gate-tunable graphene plasmons,” *Nature*, vol. 487, no. 7405, pp. 77–81, 2012.
- [21] S. Dai, W. Fang, N. Rivera, Y. Stehle, B.-Y. Jiang, J. Shen, R. Y. Tay, C. J. Ciccarino, Q. Ma, D. Rodan-Legrain, *et al.*, “Phonon polaritons in monolayers of hexagonal boron nitride,” *Advanced materials*, vol. 31, no. 37, p. 1806603, 2019.
- [22] E. Yoxall, M. Schnell, A. Y. Nikitin, O. Txoperena, A. Woessner, M. B. Lundeberg, F. Casanova, L. E. Hueso, F. H. Koppens, and R. Hillenbrand, “Direct observation of ultraslow hyperbolic polariton propagation with negative phase velocity,” *Nature Photonics*, vol. 9, no. 10, pp. 674–678, 2015.
- [23] H. Benisty, J. Greffet, and P. Lalanne, *Introduction to Nanophotonics*. Oxford graduate texts, Oxford University Press, 2022.
- [24] C. Kittel, *Introduction to Solid State Physics*. Wiley, 8 ed., 2004.
- [25] M. Born and E. Wolf, *Principles of Optics: Electromagnetic Theory of Propagation, Interference and Diffraction of Light (7th Edition)*. Cambridge University Press, 7th ed., 1999.
- [26] D. Mills and E. Burstein, “Polaritons: the electromagnetic modes of media,” *Reports on Progress in Physics*, vol. 37, no. 7, p. 817, 1974.
- [27] J. Nkoma, R. Loudon, and D. Tilley, “Elementary properties of surface polaritons,” *Journal of Physics C: Solid State Physics*, vol. 7, no. 19, p. 3547, 1974.
- [28] S. A. Maier, “Plasmonics: The promise of highly integrated optical devices,” *IEEE Journal of selected topics in Quantum Electronics*, vol. 12, no. 6, pp. 1671–1677, 2006.
- [29] Z. Han, L. Liu, and E. Forsberg, “Ultra-compact directional couplers and mach-zehnder interferometers employing surface plasmon polaritons,” *Optics communications*, vol. 259, no. 2, pp. 690–695, 2006.
- [30] A. Majumder, B. Shen, R. Polson, and R. Menon, “Ultra-compact polarization rotation in integrated silicon photonics using digital metamaterials,” *Optics express*, vol. 25, no. 17, pp. 19721–19731, 2017.
- [31] J. Zhang, L. Zhang, and W. Xu, “Surface plasmon polaritons: physics and applications,” *Journal of Physics D: Applied Physics*, vol. 45, no. 11, p. 113001, 2012.
- [32] A. B. Taylor and P. Zijlstra, “Single-molecule plasmon sensing: current status and

- future prospects,” *ACS sensors*, vol. 2, no. 8, pp. 1103–1122, 2017.
- [33] M. Li, S. K. Cushing, and N. Wu, “Plasmon-enhanced optical sensors: a review,” *Analyst*, vol. 140, no. 2, pp. 386–406, 2015.
- [34] A. K. Geim and I. V. Grigorieva, “Van der waals heterostructures,” *Nature*, vol. 499, no. 7459, pp. 419–425, 2013.
- [35] V. W. Brar, M. S. Jang, M. Sherrott, S. Kim, J. J. Lopez, L. B. Kim, M. Choi, and H. Atwater, “Hybrid surface-phonon-plasmon polariton modes in graphene/monolayer h-bn heterostructures,” *Nano letters*, vol. 14, no. 7, pp. 3876–3880, 2014.
- [36] Z. Fei, G. O. Andreev, W. Bao, L. M. Zhang, A. S. McLeod, C. Wang, M. K. Stewart, Z. Zhao, G. Dominguez, M. Thiemens, *et al.*, “Infrared nanoscopy of dirac plasmons at the graphene–sio2 interface,” *Nano letters*, vol. 11, no. 11, pp. 4701–4705, 2011.
- [37] A. Kumar, T. Low, K. H. Fung, P. Avouris, and N. X. Fang, “Tunable light–matter interaction and the role of hyperbolicity in graphene–hbn system,” *Nano letters*, vol. 15, no. 5, pp. 3172–3180, 2015.
- [38] J. D. Caldwell, I. Vurgaftman, J. G. Tischler, O. J. Glembocki, J. C. Owrutsky, and T. L. Reinecke, “Atomic-scale photonic hybrids for mid-infrared and terahertz nanophotonics,” *Nature nanotechnology*, vol. 11, no. 1, pp. 9–15, 2016.
- [39] C.-J. Kim, A. Sánchez-Castillo, Z. Ziegler, Y. Ogawa, C. Noguez, and J. Park, “Chiral atomically thin films,” *Nature nanotechnology*, vol. 11, no. 6, pp. 520–524, 2016.
- [40] J. Duan, N. Capote-Robayna, J. Taboada-Gutiérrez, G. Álvarez-Pérez, I. Prieto, J. Martín-Sánchez, A. Y. Nikitin, and P. Alonso-González, “Twisted nano-optics: manipulating light at the nanoscale with twisted phonon polaritonic slabs,” *Nano Letters*, vol. 20, no. 7, pp. 5323–5329, 2020.
- [41] G. Hu, Q. Ou, G. Si, Y. Wu, J. Wu, Z. Dai, A. Krasnok, Y. Mazor, Q. Zhang, Q. Bao, *et al.*, “Topological polaritons and photonic magic angles in twisted α -moo3 bilayers,” *Nature*, vol. 582, no. 7811, pp. 209–213, 2020.
- [42] M. Chen, X. Lin, T. H. Dinh, Z. Zheng, J. Shen, Q. Ma, H. Chen, P. Jarillo-Herrero, and S. Dai, “Configurable phonon polaritons in twisted α -moo3,” *Nature materials*, vol. 19, no. 12, pp. 1307–1311, 2020.
- [43] P.-C. Yeh, W. Jin, N. Zaki, J. Kunstmann, D. Chenet, G. Arefe, J. T. Sadowski, J. I. Dadap, P. Sutter, J. Hone, *et al.*, “Direct measurement of the tunable electronic structure of bilayer mos2 by interlayer twist,” *Nano letters*, vol. 16, no. 2, pp. 953–

- 959, 2016.
- [44] A. Woessner, M. B. Lundberg, Y. Gao, A. Principi, P. Alonso-González, M. Carrega, K. Watanabe, T. Taniguchi, G. Vignale, M. Polini, *et al.*, “Highly confined low-loss plasmons in graphene–boron nitride heterostructures,” *Nature materials*, vol. 14, no. 4, pp. 421–425, 2015.
- [45] G. Ni, H. Wang, J. Wu, Z. Fei, M. Goldflam, F. Keilmann, B. Özyilmaz, A. Castro Neto, X. Xie, M. Fogler, *et al.*, “Plasmons in graphene moiré superlattices,” *Nature materials*, vol. 14, no. 12, pp. 1217–1222, 2015.
- [46] A. Woessner, P. Alonso-González, M. B. Lundberg, Y. Gao, J. E. Barrios-Vargas, G. Navickaite, Q. Ma, D. Janner, K. Watanabe, A. W. Cummings, *et al.*, “Near-field photocurrent nanoscopy on bare and encapsulated graphene,” *Nature communications*, vol. 7, no. 1, p. 10783, 2016.
- [47] Z. Shi, X. Hong, H. A. Bechtel, B. Zeng, M. C. Martin, K. Watanabe, T. Taniguchi, Y.-R. Shen, and F. Wang, “Observation of a luttinger-liquid plasmon in metallic single-walled carbon nanotubes,” *Nature Photonics*, vol. 9, no. 8, pp. 515–519, 2015.
- [48] X. G. Xu, A. E. Tanur, and G. C. Walker, “Phase controlled homodyne infrared near-field microscopy and spectroscopy reveal inhomogeneity within and among individual boron nitride nanotubes,” *The Journal of Physical Chemistry A*, vol. 117, no. 16, pp. 3348–3354, 2013.
- [49] A. Chernikov, C. Ruppert, H. M. Hill, A. F. Rigosi, and T. F. Heinz, “Population inversion and giant bandgap renormalization in atomically thin ws₂ layers,” *Nature Photonics*, vol. 9, no. 7, pp. 466–470, 2015.
- [50] E. Van Veen, A. Nemilentsau, A. Kumar, R. Roldán, M. I. Katsnelson, T. Low, and S. Yuan, “Tuning two-dimensional hyperbolic plasmons in black phosphorus,” *Physical Review Applied*, vol. 12, no. 1, p. 014011, 2019.
- [51] T. Low, R. Roldán, H. Wang, F. Xia, P. Avouris, L. M. Moreno, and F. Guinea, “Plasmons and screening in monolayer and multilayer black phosphorus,” *Physical review letters*, vol. 113, no. 10, p. 106802, 2014.
- [52] S. Dai, Z. Fei, Q. Ma, A. Rodin, M. Wagner, A. McLeod, M. Liu, W. Gannett, W. Regan, K. Watanabe, *et al.*, “Tunable phonon polaritons in atomically thin van der waals crystals of boron nitride,” *Science*, vol. 343, no. 6175, pp. 1125–1129, 2014.
- [53] W. Ma, P. Alonso-González, S. Li, A. Y. Nikitin, J. Yuan, J. Martín-Sánchez, J. Taboada-Gutiérrez, I. Amenabar, P. Li, S. Vélez, *et al.*, “In-plane anisotropic and ultra-low-loss polaritons in a natural van der waals crystal,” *Nature*, vol. 562,

- no. 7728, pp. 557–562, 2018.
- [54] A. Ramasubramaniam, “Large excitonic effects in monolayers of molybdenum and tungsten dichalcogenides,” *Physical Review B*, vol. 86, no. 11, p. 115409, 2012.
- [55] A. Tsiatmas, V. A. Fedotov, F. J. G. de Abajo, and N. I. Zheludev, “Low-loss terahertz superconducting plasmonics,” *New Journal of Physics*, vol. 14, no. 11, p. 115006, 2012.
- [56] A. Hartstein, E. Burstein, A. Maradudin, R. Brewer, and R. Wallis, “Surface polaritons on semi-infinite gyromagnetic media,” *Journal of Physics C: Solid State Physics*, vol. 6, no. 7, p. 1266, 1973.
- [57] G. Álvarez-Pérez, J. Duan, J. Taboada-Gutiérrez, Q. Ou, E. Nikulina, S. Liu, J. H. Edgar, Q. Bao, V. Giannini, R. Hillenbrand, *et al.*, “Negative reflection of nanoscale-confined polaritons in a low-loss natural medium,” *Science advances*, vol. 8, no. 29, p. eabp8486, 2022.
- [58] B. Chang, S. Xiao, *et al.*, “Planar refraction and lensing of highly confined polaritons in anisotropic media,” *Nature Communications*, vol. 12, no. 1, p. 4325, 2021.
- [59] G. Álvarez-Pérez, K. V. Voronin, V. S. Volkov, P. Alonso-González, and A. Y. Nikitin, “Analytical approximations for the dispersion of electromagnetic modes in slabs of biaxial crystals,” *Physical Review B*, vol. 100, no. 23, p. 235408, 2019.
- [60] L. Ju, B. Geng, J. Horng, C. Girit, M. Martin, Z. Hao, H. A. Bechtel, X. Liang, A. Zettl, Y. R. Shen, *et al.*, “Graphene plasmonics for tunable terahertz metamaterials,” *Nature nanotechnology*, vol. 6, no. 10, pp. 630–634, 2011.
- [61] P. Alonso-González, A. Y. Nikitin, F. Golmar, A. Centeno, A. Pesquera, S. Vélez, J. Chen, G. Navickaite, F. Koppens, A. Zurutuza, F. Casanova, L. E. Hueso, and R. Hillenbrand, “Controlling graphene plasmons with resonant metal antennas and spatial conductivity patterns,” *Science*, vol. 344, p. 1369–1373, June 2014.
- [62] P. Pons-Valencia, F. J. Alfaro-Mozaz, M. M. Wiecha, V. Bielek, I. Dolado, S. Vélez, P. Li, P. Alonso-González, F. Casanova, L. E. Hueso, L. Martín-Moreno, R. Hillenbrand, and A. Y. Nikitin, “Launching of hyperbolic phonon-polaritons in h-bn slabs by resonant metal plasmonic antennas,” *Nature Communications*, vol. 10, July 2019.
- [63] I.-H. Lee, D. Yoo, P. Avouris, T. Low, and S.-H. Oh, “Graphene acoustic plasmon resonator for ultrasensitive infrared spectroscopy,” *Nature nanotechnology*, vol. 14, no. 4, pp. 313–319, 2019.
- [64] H. Herzig Sheinfux, L. Orsini, M. Jung, I. Torre, M. Ceccanti, S. Marconi, R. Maniara, D. Barcons Ruiz, A. Hötger, R. Bertini, *et al.*, “High-quality nanocavities

- through multimodal confinement of hyperbolic polaritons in hexagonal boron nitride,” *Nature Materials*, pp. 1–7, 2024.
- [65] A. A. Govyadinov, A. Konečná, A. Chuvilin, S. Vélez, I. Dolado, A. Y. Nikitin, S. Lopatin, F. Casanova, L. E. Hueso, J. Aizpurua, *et al.*, “Probing low-energy hyperbolic polaritons in van der waals crystals with an electron microscope,” *Nature Communications*, vol. 8, no. 1, p. 95, 2017.
- [66] N. Li, X. Guo, X. Yang, R. Qi, T. Qiao, Y. Li, R. Shi, Y. Li, K. Liu, Z. Xu, *et al.*, “Direct observation of highly confined phonon polaritons in suspended monolayer hexagonal boron nitride,” *Nature Materials*, vol. 20, no. 1, pp. 43–48, 2021.
- [67] F. J. Garcia de Abajo and V. Di Giulio, “Optical excitations with electron beams: Challenges and opportunities,” *ACS photonics*, vol. 8, no. 4, pp. 945–974, 2021.
- [68] S. Dai, Q. Ma, M. Liu, T. Andersen, Z. Fei, M. Goldflam, M. Wagner, K. Watanabe, T. Taniguchi, M. Thiemens, *et al.*, “Graphene on hexagonal boron nitride as a tunable hyperbolic metamaterial,” *Nature nanotechnology*, vol. 10, no. 8, pp. 682–686, 2015.
- [69] Y. Qi, M. A. Sadi, D. Hu, M. Zheng, Z. Wu, Y. Jiang, and Y. P. Chen, “Recent progress in strain engineering on van der waals 2d materials: Tunable electrical, electrochemical, magnetic, and optical properties,” *Advanced Materials*, vol. 35, no. 12, p. 2205714, 2023.
- [70] Y. Liu, N. O. Weiss, X. Duan, H.-C. Cheng, Y. Huang, and X. Duan, “Van der waals heterostructures and devices,” *Nature Reviews Materials*, vol. 1, no. 9, pp. 1–17, 2016.
- [71] S. Wu, S. Buckley, J. R. Schaibley, L. Feng, J. Yan, D. G. Mandrus, F. Hatami, W. Yao, J. Vučković, A. Majumdar, *et al.*, “Monolayer semiconductor nanocavity lasers with ultralow thresholds,” *nature*, vol. 520, no. 7545, pp. 69–72, 2015.
- [72] J. R. Schaibley, H. Yu, G. Clark, P. Rivera, J. S. Ross, K. L. Seyler, W. Yao, and X. Xu, “Valleytronics in 2d materials,” *Nature Reviews Materials*, vol. 1, no. 11, pp. 1–15, 2016.
- [73] K. F. Mak and J. Shan, “Photonics and optoelectronics of 2d semiconductor transition metal dichalcogenides,” *Nature Photonics*, vol. 10, no. 4, pp. 216–226, 2016.
- [74] C.-h. Liu, J. Zheng, Y. Chen, T. Fryett, and A. Majumdar, “Van der waals materials integrated nanophotonic devices,” *Optical materials express*, vol. 9, no. 2, pp. 384–399, 2019.
- [75] D. Jariwala, A. R. Davoyan, J. Wong, and H. A. Atwater, “Van der waals materials

- for atomically-thin photovoltaics: promise and outlook,” *Acs Photonics*, vol. 4, no. 12, pp. 2962–2970, 2017.
- [76] Q. Zhang, G. Hu, W. Ma, P. Li, A. Krasnok, R. Hillenbrand, A. Alù, and C.-W. Qiu, “Interface nano-optics with van der waals polaritons,” *Nature*, vol. 597, no. 7875, pp. 187–195, 2021.
- [77] J. D. Caldwell, I. Aharonovich, G. Cassabois, J. H. Edgar, B. Gil, and D. N. Basov, “Photonics with hexagonal boron nitride,” *Nature Reviews Materials*, vol. 4, no. 8, pp. 552–567, 2019.
- [78] K. Li and D. Xue, “Estimation of electronegativity values of elements in different valence states,” *The Journal of Physical Chemistry A*, vol. 110, no. 39, pp. 11332–11337, 2006.
- [79] M. Mohr, J. Maultzsch, E. Dobardžić, S. Reich, I. Milošević, M. Damnjanović, A. Bosak, M. Krisch, and C. Thomsen, “Phonon dispersion of graphite by inelastic x-ray scattering,” *Physical Review B*, vol. 76, no. 3, p. 035439, 2007.
- [80] A. J. Giles, S. Dai, I. Vurgaftman, T. Hoffman, S. Liu, L. Lindsay, C. T. Ellis, N. Assefa, I. Chatzakis, T. L. Reinecke, *et al.*, “Ultralow-loss polaritons in isotopically pure boron nitride,” *Nature materials*, vol. 17, no. 2, pp. 134–139, 2018.
- [81] R. Geick, C. Perry, and G. Rupprecht, “Normal modes in hexagonal boron nitride,” *Physical Review*, vol. 146, no. 2, p. 543, 1966.
- [82] F. Alfaro-Mozaz, P. Alonso-González, S. Vélez, I. Dolado, M. Autore, S. Mastel, F. Casanova, L. Hueso, P. Li, A. Y. Nikitin, *et al.*, “Nanoimaging of resonating hyperbolic polaritons in linear boron nitride antennas,” *Nature communications*, vol. 8, no. 1, p. 15624, 2017.
- [83] M. B. Lundberg, Y. Gao, A. Woessner, C. Tan, P. Alonso-González, K. Watanabe, T. Taniguchi, J. Hone, R. Hillenbrand, and F. H. Koppens, “Thermoelectric detection and imaging of propagating graphene plasmons,” *Nature materials*, vol. 16, no. 2, pp. 204–207, 2017.
- [84] J. Taboada-Gutiérrez, G. Álvarez-Pérez, J. Duan, W. Ma, K. Crowley, I. Prieto, A. Bylinkin, M. Autore, H. Volkova, K. Kimura, *et al.*, “Broad spectral tuning of ultra-low-loss polaritons in a van der waals crystal by intercalation,” *Nature materials*, vol. 19, no. 9, pp. 964–968, 2020.
- [85] G. Ni, d. A. McLeod, Z. Sun, L. Wang, L. Xiong, K. Post, S. Sunku, B.-Y. Jiang, J. Hone, C. R. Dean, *et al.*, “Fundamental limits to graphene plasmonics,” *Nature*, vol. 557, no. 7706, pp. 530–533, 2018.

- [86] H. Raether, “Surface plasmons on gratings,” *Surface plasmons on smooth and rough surfaces and on gratings*, pp. 91–116, 2006.
- [87] F. J. Alfaro Mozaz, *Mid-infrared nanophotonics with hyperbolic phonon polaritons*. PhD thesis, University of the Basque Country, 2020.
- [88] E. Kretschmann and H. Raether, “Radiative decay of non radiative surface plasmons excited by light,” *Zeitschrift für Naturforschung A*, vol. 23, no. 12, pp. 2135–2136, 1968.
- [89] A. Otto, “Excitation of nonradiative surface plasma waves in silver by the method of frustrated total reflection,” *Zeitschrift für Physik A Hadrons and nuclei*, vol. 216, no. 4, pp. 398–410, 1968.
- [90] L. Gilburd, K. S. Kim, K. Ho, D. Trajanoski, A. Maiti, D. Halverson, S. de Beer, and G. C. Walker, “Hexagonal boron nitride self-launches hyperbolic phonon polaritons,” *The journal of physical chemistry letters*, vol. 8, no. 10, pp. 2158–2162, 2017.
- [91] A. Y. Nikitin, E. Yoxall, M. Schnell, S. Vèlez, I. Dolado, P. Alonso-Gonzalez, F. Casanova, L. E. Hueso, and R. Hillenbrand, “Nanofocusing of hyperbolic phonon polaritons in a tapered boron nitride slab,” *ACS Photonics*, vol. 3, no. 6, pp. 924–929, 2016.
- [92] S. Liu, R. He, L. Xue, J. Li, B. Liu, and J. H. Edgar, “Single crystal growth of millimeter-sized monoisotopic hexagonal boron nitride,” *Chemistry of materials*, vol. 30, no. 18, pp. 6222–6225, 2018.
- [93] T. Taliercio and P. Biagioni, “Semiconductor infrared plasmonics,” *Nanophotonics*, vol. 8, no. 6, pp. 949–990, 2019.
- [94] A. Leitis, A. Heßler, S. Wahl, M. Wuttig, T. Taubner, A. Tittl, and H. Altug, “All-dielectric programmable huygens’ metasurfaces,” *Advanced Functional Materials*, vol. 30, no. 19, p. 1910259, 2020.
- [95] S. Law, L. Yu, A. Rosenberg, and D. Wasserman, “All-semiconductor plasmonic nanoantennas for infrared sensing,” *Nano letters*, vol. 13, no. 9, pp. 4569–4574, 2013.
- [96] A. Leitis, A. Tittl, M. Liu, B. H. Lee, M. B. Gu, Y. S. Kivshar, and H. Altug, “Angle-multiplexed all-dielectric metasurfaces for broadband molecular fingerprint retrieval,” *Science advances*, vol. 5, no. 5, p. eaaw2871, 2019.
- [97] Y. Chang, D. Hasan, B. Dong, J. Wei, Y. Ma, G. Zhou, K. W. Ang, and C. Lee, “All-dielectric surface-enhanced infrared absorption-based gas sensor using guided

- resonance,” *ACS applied materials & interfaces*, vol. 10, no. 44, pp. 38272–38279, 2018.
- [98] Y. Chen, H. Lin, J. Hu, and M. Li, “Heterogeneously integrated silicon photonics for the mid-infrared and spectroscopic sensing,” *ACS nano*, vol. 8, no. 7, pp. 6955–6961, 2014.
- [99] D. Rodrigo, A. Tittl, A. John-Herpin, O. Limaj, and H. Altug, “Self-similar multi-resonant nanoantenna arrays for sensing from near-to mid-infrared,” *Acs Photonics*, vol. 5, no. 12, pp. 4903–4911, 2018.
- [100] S. Gottheim, H. Zhang, A. O. Govorov, and N. J. Halas, “Fractal nanoparticle plasmonics: The cayley tree,” *ACS nano*, vol. 9, no. 3, pp. 3284–3292, 2015.
- [101] C. Huck, J. Vogt, M. Sendner, D. Hengstler, F. Neubrech, and A. Pucci, “Plasmonic enhancement of infrared vibrational signals: nanoslits versus nanorods,” *Acs Photonics*, vol. 2, no. 10, pp. 1489–1497, 2015.
- [102] P. R. Griffiths, “Fourier transform infrared spectrometry,” *Science*, vol. 222, no. 4621, pp. 297–302, 1983.
- [103] A. Hartstein, J. Kirtley, and J. Tsang, “Enhancement of the infrared absorption from molecular monolayers with thin metal overlayers,” *Physical Review Letters*, vol. 45, no. 3, p. 201, 1980.
- [104] M. Osawa, “Surface-enhanced infrared absorption,” in *Near-field optics and surface plasmon polaritons*, pp. 163–187, Springer, 2006.
- [105] F. Neubrech, C. Huck, K. Weber, A. Pucci, and H. Giessen, “Surface-enhanced infrared spectroscopy using resonant nanoantennas,” *Chemical reviews*, vol. 117, no. 7, pp. 5110–5145, 2017.
- [106] J. Aizpurua, T. Taubner, F. J. G. de Abajo, M. Brehm, and R. Hillenbrand, “Substrate-enhanced infrared near-field spectroscopy,” *Optics Express*, vol. 16, no. 3, pp. 1529–1545, 2008.
- [107] T. Wang, V. H. Nguyen, A. Buchenauer, U. Schnakenberg, and T. Taubner, “Surface enhanced infrared spectroscopy with gold strip gratings,” *Optics express*, vol. 21, no. 7, pp. 9005–9010, 2013.
- [108] F. Neubrech, A. Pucci, T. W. Cornelius, S. Karim, A. García-Etxarri, and J. Aizpurua, “Resonant plasmonic and vibrational coupling in a tailored nanoantenna for infrared detection,” *Physical review letters*, vol. 101, no. 15, p. 157403, 2008.
- [109] R. Adato, A. A. Yanik, J. J. Amsden, D. L. Kaplan, F. G. Omenetto, M. K. Hong, S. Erramilli, and H. Altug, “Ultra-sensitive vibrational spectroscopy of pro-

- tein monolayers with plasmonic nanoantenna arrays,” *Proceedings of the National Academy of Sciences*, vol. 106, no. 46, pp. 19227–19232, 2009.
- [110] T. Neuman, C. Huck, J. Vogt, F. Neubrech, R. Hillenbrand, J. Aizpurua, and A. Pucci, “Importance of plasmonic scattering for an optimal enhancement of vibrational absorption in seira with linear metallic antennas,” *The Journal of Physical Chemistry C*, vol. 119, no. 47, pp. 26652–26662, 2015.
- [111] A. Agrawal, A. Singh, S. Yazdi, A. Singh, G. K. Ong, K. Bustillo, R. W. Johns, E. Ringe, and D. J. Milliron, “Resonant coupling between molecular vibrations and localized surface plasmon resonance of faceted metal oxide nanocrystals,” *Nano letters*, vol. 17, no. 4, pp. 2611–2620, 2017.
- [112] L. Baldassarre, E. Sakat, J. Frigerio, A. Samarelli, K. Gallacher, E. Calandrini, G. Isella, D. J. Paul, M. Ortolani, and P. Biagioni, “Midinfrared plasmon-enhanced spectroscopy with germanium antennas on silicon substrates,” *Nano letters*, vol. 15, no. 11, pp. 7225–7231, 2015.
- [113] F. B. Barho, F. Gonzalez-Posada, M.-J. Milla-Rodrigo, M. Bomers, L. Cerutti, and T. Taliercio, “All-semiconductor plasmonic gratings for biosensing applications in the mid-infrared spectral range,” *Optics express*, vol. 24, no. 14, pp. 16175–16190, 2016.
- [114] D. Rodrigo, O. Limaj, D. Janner, D. Etezadi, F. J. García de Abajo, V. Pruneri, and H. Altug, “Mid-infrared plasmonic biosensing with graphene,” *Science*, vol. 349, no. 6244, pp. 165–168, 2015.
- [115] H. Hu, X. Yang, F. Zhai, D. Hu, R. Liu, K. Liu, Z. Sun, and Q. Dai, “Far-field nanoscale infrared spectroscopy of vibrational fingerprints of molecules with graphene plasmons,” *Nature communications*, vol. 7, no. 1, p. 12334, 2016.
- [116] D. B. Farmer, P. Avouris, Y. Li, T. F. Heinz, and S.-J. Han, “Ultrasensitive plasmonic detection of molecules with graphene,” *Acs Photonics*, vol. 3, no. 4, pp. 553–557, 2016.
- [117] A. Tittl, A. Leitis, M. Liu, F. Yesilkoy, D.-Y. Choi, D. N. Neshev, Y. S. Kivshar, and H. Altug, “Imaging-based molecular barcoding with pixelated dielectric metasurfaces,” *Science*, vol. 360, no. 6393, pp. 1105–1109, 2018.
- [118] A. Thomas, J. George, A. Shalabney, M. Dryzhakov, S. J. Varma, J. Moran, T. Chervy, X. Zhong, E. Devaux, C. Genet, *et al.*, “Ground-state chemical reactivity under vibrational coupling to the vacuum electromagnetic field,” *Angewandte Chemie*, vol. 128, no. 38, pp. 11634–11638, 2016.
- [119] J. D. Caldwell, A. V. Kretinin, Y. Chen, V. Giannini, M. M. Fogler, Y. Francescato,

- C. T. Ellis, J. G. Tischler, C. R. Woods, A. J. Giles, *et al.*, “Sub-diffractive volume-confined polaritons in the natural hyperbolic material hexagonal boron nitride,” *Nature communications*, vol. 5, no. 1, p. 5221, 2014.
- [120] N. J. Bareza, B. Paulillo, T. M. Slipchenko, M. Autore, I. Dolado, S. Liu, J. H. Edgar, S. Velez, L. Martin-Moreno, R. Hillenbrand, *et al.*, “Phonon-enhanced mid-infrared CO₂ gas sensing using boron nitride nanoresonators,” *ACS photonics*, vol. 9, no. 1, pp. 34–42, 2022.
- [121] A. Huber and K. Crozier, “Controlling the near-field oscillations of loaded plasmonic nanoantennas,” *Nature Photonics*, vol. 3, no. 5, pp. 287–291, 2009.
- [122] J. Alkorta, “Phase-resolved mapping of the near-field vector and polarization state in nanoscale antenna gaps,” *Nano letters*, vol. 10, no. 9, pp. 3524–3528, 2010.
- [123] M. Schnell, P. Alonso-Gonzalez, L. Arzubia, F. Casanova, A. Chuvilin, and R. Hillenbrand, “Nanofocusing of mid-infrared energy with tapered transmission lines,” *Nature photonics*, vol. 5, no. 5, pp. 283–287, 2011.
- [124] S. Chen, A. Bylinkin, Z. Wang, M. Schnell, G. Chandan, P. Li, A. Y. Nikitin, S. Law, and R. Hillenbrand, “Real-space nanoimaging of THz polaritons in the topological insulator Bi₂Se₃,” *Nature communications*, vol. 13, no. 1, p. 1374, 2022.
- [125] S. Chen, P. Leng, A. Konečná, E. Modin, M. Gutierrez-Amigo, E. Vicentini, B. Martín-García, M. Barra-Burillo, I. Niehues, C. Maciel Escudero, *et al.*, “Real-space observation of ultraconfined in-plane anisotropic acoustic terahertz plasmon polaritons,” *Nature Materials*, pp. 1–7, 2023.
- [126] L. Novotny and B. Hecht, *Principles of nano-optics*. Cambridge university press, 2012.
- [127] F. Keilmann and R. Hillenbrand, “Near-field microscopy by elastic light scattering from a tip,” *Philosophical Transactions of the Royal Society of London. Series A: Mathematical, Physical and Engineering Sciences*, vol. 362, no. 1817, pp. 787–805, 2004.
- [128] J.-J. Greffet and R. Carminati, “Image formation in near-field optics,” *Progress in surface science*, vol. 56, no. 3, pp. 133–237, 1997.
- [129] N. Ocelic, A. Huber, and R. Hillenbrand, “Pseudoheterodyne detection for background-free near-field spectroscopy,” *Applied Physics Letters*, vol. 89, no. 10, 2006.
- [130] N. Ocelic, *Quantitative near-field phonon-polariton spectroscopy*. PhD thesis, Technische Universität München, 2007.

- [131] F. Huth, A. Govyadinov, S. Amarie, W. Nuansing, F. Keilmann, and R. Hillenbrand, “Nano-ftir absorption spectroscopy of molecular fingerprints at 20 nm spatial resolution,” *Nano letters*, vol. 12, no. 8, pp. 3973–3978, 2012.
- [132] S. Amarie, T. Ganz, and F. Keilmann, “Mid-infrared near-field spectroscopy,” *Optics Express*, vol. 17, no. 24, pp. 21794–21801, 2009.
- [133] A. A. Govyadinov, I. Amenabar, F. Huth, P. S. Carney, and R. Hillenbrand, “Quantitative measurement of local infrared absorption and dielectric function with tip-enhanced near-field microscopy,” *The journal of physical chemistry letters*, vol. 4, no. 9, pp. 1526–1531, 2013.
- [134] I. Amenabar Altuna, *Infrared nanospectroscopy and hyperspectral nanoimaging of organic matter*. PhD thesis, University of the Basque Country, 2017.
- [135] L. N. Casses, K. J. Kaltenecker, S. Xiao, M. Wubs, and N. Stenger, “Quantitative near-field characterization of surface plasmon polaritons on monocrystalline gold platelets,” *Optics Express*, vol. 30, no. 7, pp. 11181–11191, 2022.
- [136] L. Novotny, “Strong coupling, energy splitting, and level crossings: A classical perspective,” *American Journal of Physics*, vol. 78, no. 11, pp. 1199–1202, 2010.
- [137] D. Yoo, F. de León-Pérez, M. Pelton, I.-H. Lee, D. A. Mohr, M. B. Raschke, J. D. Caldwell, L. Martín-Moreno, and S.-H. Oh, “Ultrastrong plasmon–phonon coupling via epsilon-near-zero nanocavities,” *Nature Photonics*, vol. 15, no. 2, pp. 125–130, 2021.
- [138] X. Wu, S. K. Gray, and M. Pelton, “Quantum-dot-induced transparency in a nanoscale plasmonic resonator,” *Optics express*, vol. 18, no. 23, pp. 23633–23645, 2010.
- [139] U. Muniain, J. Aizpurua, R. Hillenbrand, L. Martín-Moreno, and R. Esteban, “Description of ultrastrong light-matter interaction through coupled harmonic oscillator models and their connection with cavity-qed hamiltonians,” *arXiv preprint arXiv:2402.11944*, 2024.
- [140] U. Muniain Caballero, *Quantum-mechanical study of optical excitations in nanoscale systems: first-principles description of plasmons, tunneling-induced light emission and ultrastrong light-matter interaction*. PhD thesis, University of the Basque Country, 2023.
- [141] M. Pelton, S. D. Storm, and H. Leng, “Strong coupling of emitters to single plasmonic nanoparticles: exciton-induced transparency and rabi splitting,” *Nanoscale*, vol. 11, no. 31, pp. 14540–14552, 2019.

-
- [142] J.-J. Greffet, “Introduction to surface plasmon theory,” in *Plasmonics: From Basics to Advanced Topics*, pp. 105–148, Springer, 2012.
- [143] N. C. Passler and A. Paarmann, “Generalized 4×4 matrix formalism for light propagation in anisotropic stratified media: study of surface phonon polaritons in polar dielectric heterostructures,” *JOSA B*, vol. 34, no. 10, pp. 2128–2139, 2017.
- [144] R. Ritchie, R. Hamm, M. Williams, and E. Arakawa, “Dispersion relations of elementary excitations when damping is present,” *physica status solidi (b)*, vol. 84, no. 1, pp. 367–373, 1977.
- [145] P. Han, X. Wang, and Y. Zhang, “Time-resolved terahertz spectroscopy studies on 2d van der waals materials,” *Advanced Optical Materials*, vol. 8, no. 3, p. 1900533, 2020.
- [146] P. Merkl, F. Mooshammer, P. Steinleitner, A. Girnghuber, K.-Q. Lin, P. Nagler, J. Holler, C. Schüller, J. M. Lupton, T. Korn, *et al.*, “Ultrafast transition between exciton phases in van der waals heterostructures,” *Nature materials*, vol. 18, no. 7, pp. 691–696, 2019.
- [147] Z. Zheng, J. Chen, Y. Wang, X. Wang, X. Chen, P. Liu, J. Xu, W. Xie, H. Chen, S. Deng, *et al.*, “Highly confined and tunable hyperbolic phonon polaritons in van der waals semiconducting transition metal oxides,” *Advanced Materials*, vol. 30, no. 13, p. 1705318, 2018.
- [148] K. S. Kim, D. Trajanoski, K. Ho, L. Gilburd, A. Maiti, L. van der Velden, S. de Beer, and G. C. Walker, “The effect of adjacent materials on the propagation of phonon polaritons in hexagonal boron nitride,” *The journal of physical chemistry letters*, vol. 8, no. 13, pp. 2902–2908, 2017.
- [149] A. Fali, S. T. White, T. G. Folland, M. He, N. A. Aghamiri, S. Liu, J. H. Edgar, J. D. Caldwell, R. F. Haglund, and Y. Abate, “Refractive index-based control of hyperbolic phonon-polariton propagation,” *Nano letters*, vol. 19, no. 11, pp. 7725–7734, 2019.
- [150] R. F. Ribeiro, L. A. Martínez-Martínez, M. Du, J. Campos-Gonzalez-Angulo, and J. Yuen-Zhou, “Polariton chemistry: controlling molecular dynamics with optical cavities,” *Chemical science*, vol. 9, no. 30, pp. 6325–6339, 2018.
- [151] J. Feist, J. Galego, and F. J. Garcia-Vidal, “Polaritonic chemistry with organic molecules,” *ACS Photonics*, vol. 5, no. 1, pp. 205–216, 2018.
- [152] F. Herrera and J. Owrutsky, “Molecular polaritons for controlling chemistry with quantum optics,” *The Journal of chemical physics*, vol. 152, no. 10, 2020.

- [153] Y. Francescato, V. Giannini, J. Yang, M. Huang, and S. A. Maier, “Graphene sandwiches as a platform for broadband molecular spectroscopy,” *ACS Photonics*, vol. 1, no. 5, pp. 437–443, 2014.
- [154] R. W. Alexander, G. Kovener, and R. J. Bell, “Dispersion curves for surface electromagnetic waves with damping,” *Physical Review Letters*, vol. 32, no. 4, p. 154, 1974.
- [155] E. Arakawa, M. Williams, R. Hamm, and R. Ritchie, “Effect of damping on surface plasmon dispersion,” *Physical Review Letters*, vol. 31, no. 18, p. 1127, 1973.
- [156] E. Schuller, H. Falge, and G. Borstel, “Dispersion curves of surface phonon-polaritons with backbending,” *Physics Letters A*, vol. 54, no. 4, pp. 317–318, 1975.
- [157] F. Hu, Y. Luan, M. Scott, J. Yan, D. Mandrus, X. Xu, and Z. Fei, “Imaging exciton–polariton transport in mose2 waveguides,” *Nature Photonics*, vol. 11, no. 6, pp. 356–360, 2017.
- [158] Y. Zhang, Q.-S. Meng, L. Zhang, Y. Luo, Y.-J. Yu, B. Yang, Y. Zhang, R. Esteban, J. Aizpurua, Y. Luo, *et al.*, “Sub-nanometre control of the coherent interaction between a single molecule and a plasmonic nanocavity,” *Nature Communications*, vol. 8, no. 1, p. 15225, 2017.
- [159] M. V. Rybin, S. F. Mingaleev, M. F. Limonov, and Y. S. Kivshar, “Purcell effect and lamb shift as interference phenomena,” *Scientific reports*, vol. 6, no. 1, p. 20599, 2016.
- [160] K. Hennessy, A. Badolato, M. Winger, D. Gerace, M. Atatüre, S. Gulde, S. Fält, E. L. Hu, and A. Imamoglu, “Quantum nature of a strongly coupled single quantum dot–cavity system,” *Nature*, vol. 445, no. 7130, pp. 896–899, 2007.
- [161] I. Pockrand, A. Brillante, and D. Möbius, “Exciton–surface plasmon coupling: An experimental investigation,” *The Journal of chemical physics*, vol. 77, no. 12, pp. 6289–6295, 1982.
- [162] J. Bellessa, C. Bonnand, J. Plenat, and J. Mugnier, “Strong coupling between surface plasmons and excitons in an organic semiconductor,” *Physical review letters*, vol. 93, no. 3, p. 036404, 2004.
- [163] H. Memmi, O. Benson, S. Sadofev, and S. Kalusniak, “Strong coupling between surface plasmon polaritons and molecular vibrations,” *Physical review letters*, vol. 118, no. 12, p. 126802, 2017.
- [164] I. Shlesinger, H. Monin, J. Moreau, J.-P. Hugonin, M. Dufour, S. Ithurria, B. Vest, and J.-J. Greffet, “Strong coupling of nanoplatelets and surface plasmons on a gold

- surface,” *ACS photonics*, vol. 6, no. 11, pp. 2643–2648, 2019.
- [165] G. G. Rozenman, K. Akulov, A. Golombek, and T. Schwartz, “Long-range transport of organic exciton-polaritons revealed by ultrafast microscopy,” *ACS Photonics*, vol. 5, no. 1, pp. 105–110, 2018.
- [166] F. J. Bezares, A. D. Sanctis, J. Saavedra, A. Woessner, P. Alonso-González, I. Amenabar, J. Chen, T. H. Bointon, S. Dai, M. M. Fogler, *et al.*, “Intrinsic plasmon-phonon interactions in highly doped graphene: A near-field imaging study,” *Nano letters*, vol. 17, no. 10, pp. 5908–5913, 2017.
- [167] F. J. Alfaro-Mozaz, S. G. Rodrigo, P. Alonso-González, S. Vélez, I. Dolado, F. Casanova, L. E. Hueso, L. Martín-Moreno, R. Hillenbrand, and A. Y. Nikitin, “Deeply subwavelength phonon-polaritonic crystal made of a van der waals material,” *Nature communications*, vol. 10, no. 1, p. 42, 2019.
- [168] R. Glover III and M. Tinkham, “Conductivity of superconducting films for photon energies between 0.3 and 4 0 k t c,” *Physical Review*, vol. 108, no. 2, p. 243, 1957.
- [169] T. Glaser, S. Beck, B. Lunkenheimer, D. Donhauser, A. Köhn, M. Kröger, and A. Pucci, “Infrared study of the moo3 doping efficiency in 4, 4’-bis (n-carbazoly1)-1, 1’-biphenyl (cbp),” *Organic Electronics*, vol. 14, no. 2, pp. 575–583, 2013.
- [170] E. D. Palik, *Handbook of optical constants of solids*, vol. 3. Academic press, 1998.
- [171] P. Li, I. Dolado, F. Alfaro-Mozaz, A. Y. Nikitin, F. Casanova, L. Hueso, S. Vélez, and R. Hillenbrand, “Optical nanoimaging of hyperbolic surface polaritons at the edges of van der waals materials,” *Nano letters*, vol. 17, no. 1, pp. 228–235, 2017.
- [172] A. A. Bakulin, S. E. Morgan, T. B. Kehoe, M. W. Wilson, A. W. Chin, D. Zigmantas, D. Egorova, and A. Rao, “Real-time observation of multiexcitonic states in ultrafast singlet fission using coherent 2d electronic spectroscopy,” *Nature chemistry*, vol. 8, no. 1, pp. 16–23, 2016.
- [173] A. J. Musser, M. Liebel, C. Schnedermann, T. Wende, T. B. Kehoe, A. Rao, and P. Kukura, “Evidence for conical intersection dynamics mediating ultrafast singlet exciton fission,” *Nature Physics*, vol. 11, no. 4, pp. 352–357, 2015.
- [174] J. Aragón and A. Troisi, “Dynamics of the excitonic coupling in organic crystals,” *Physical Review Letters*, vol. 114, no. 2, p. 026402, 2015.
- [175] K. L. Domina, V. V. Khardikov, V. Goryashko, and A. Y. Nikitin, “Bonding and antibonding modes in metal-dielectric-metal plasmonic antennas for dual-band applications,” *Advanced Optical Materials*, vol. 8, no. 5, p. 1900942, 2020.
- [176] F. Le, D. W. Brandl, Y. A. Urzhumov, H. Wang, J. Kundu, N. J. Halas, J. Aizpurua,

- and P. Nordlander, “Metallic nanoparticle arrays: a common substrate for both surface-enhanced raman scattering and surface-enhanced infrared absorption,” *ACS nano*, vol. 2, no. 4, pp. 707–718, 2008.
- [177] C. D’Andrea, J. Bochterle, A. Toma, C. Huck, F. Neubrech, E. Messina, B. Fazio, O. M. Marago, E. Di Fabrizio, M. Lamy de La Chapelle, *et al.*, “Optical nanoantennas for multiband surface-enhanced infrared and raman spectroscopy,” *ACS nano*, vol. 7, no. 4, pp. 3522–3531, 2013.
- [178] M. He, S. I. Halimi, T. G. Folland, S. S. Sunku, S. Liu, J. H. Edgar, D. N. Basov, S. M. Weiss, and J. D. Caldwell, “Guided mid-ir and near-ir light within a hybrid hyperbolic-material/silicon waveguide heterostructure,” *Advanced Materials*, vol. 33, no. 11, p. 2004305, 2021.
- [179] J. D. Caldwell and K. S. Novoselov, “Mid-infrared nanophotonics,” *Nature materials*, vol. 14, no. 4, pp. 364–366, 2015.
- [180] A. Bylinkin, M. Schnell, M. Autore, F. Calavalle, P. Li, J. Taboada-Gutierrez, S. Liu, J. H. Edgar, F. Casanova, L. E. Hueso, *et al.*, “Real-space observation of vibrational strong coupling between propagating phonon polaritons and organic molecules,” *Nature Photonics*, vol. 15, no. 3, pp. 197–202, 2021.
- [181] P. A. Thomas, K. S. Menghrajani, and W. L. Barnes, “Cavity-free ultrastrong light-matter coupling,” *The Journal of Physical Chemistry Letters*, vol. 12, no. 29, pp. 6914–6918, 2021.
- [182] A. D. Rakić, A. B. Djurišić, J. M. Elazar, and M. L. Majewski, “Optical properties of metallic films for vertical-cavity optoelectronic devices,” *Applied optics*, vol. 37, no. 22, pp. 5271–5283, 1998.
- [183] S. G. Rodrigo, F. García-Vidal, and L. Martín-Moreno, “Influence of material properties on extraordinary optical transmission through hole arrays,” *Physical Review B*, vol. 77, no. 7, p. 075401, 2008.
- [184] P. Zomer, M. Guimarães, J. Brant, N. Tombros, and B. Van Wees, “Fast pick up technique for high quality heterostructures of bilayer graphene and hexagonal boron nitride,” *Applied Physics Letters*, vol. 105, no. 1, 2014.
- [185] I. Dolado, C. Maciel-Escudero, E. Nikulina, E. Modin, F. Calavalle, S. Chen, A. Bylinkin, F. J. Alfaro-Mozaz, J. Li, J. H. Edgar, *et al.*, “Remote near-field spectroscopy of vibrational strong coupling between organic molecules and phononic nanoresonators,” *Nature Communications*, vol. 13, no. 1, p. 6850, 2022.
- [186] M. Barra-Burillo, U. Muniain, S. Catalano, M. Autore, F. Casanova, L. E. Hueso, J. Aizpurua, R. Esteban, and R. Hillenbrand, “Microcavity phonon polaritons from

- the weak to the ultrastrong phonon–photon coupling regime,” *Nature communications*, vol. 12, no. 1, p. 6206, 2021.
- [187] A. Canales, D. G. Baranov, T. J. Antosiewicz, and T. Shegai, “Abundance of cavity-free polaritonic states in resonant materials and nanostructures,” *The Journal of Chemical Physics*, vol. 154, no. 2, 2021.

Acknowledgments

I would like to express my deepest gratitude to Dr. Alexey Nikitin and Prof. Rainer Hillenbrand for the opportunity to work with them. Working alongside them was a journey enriched with valuable lessons, extensive brainstorming, and moments that tested our patience. Their guidance and mentorship have been invaluable to my research, and I am grateful for the learning experiences shared with each of them.

I sincerely thank my tutor, Prof. Nerea Zabala-Unzalu for her guidance and support, especially in navigating the bureaucracy at the university.

Special thanks to Dr. Marta Autore, who played a crucial role during my initial days at Nanogune. Her support and introduction to the lab environment laid the groundwork for my successful integration into the group and the following results.

I am deeply grateful to Dr. Francesco Calavalle from the Nanodevice group, who dedicated countless hours to evaporating molecules for my projects, irrespective of the early mornings or late evenings.

My thanks also extend to all members of the Nanooptics group. Carlos Crespo for his exceptional technical support; Dr. Monika Goikoetxea for her assistance with managing research projects and grants; Dr. Javier Alfaro-Mozaz for his help with numerical simulations; Irene Dolado and Dr. Maria Barra-Burillo for their help with fabrication. Dr. Iban Amenabar, Dr. Andrea Konečná, Dr. Shu Chen, Dr. Martin Schnell, Dr. Peining Li, Dr. Lars Mester, Dr. Eugenio Calandrini, Divya Virmani, Florina Marxer, Iker Herrero-León, Jan Krpensky, Dr. Théo Hannotte, Dr. Elizaveta Nikulina, Dr. Eduardo Vicentini, Dr. Iris Niehues, Isabel Pascual-Robledo, Marita Wagner, and Dr. Philippe Roelli have all contributed to a supportive and collaborative atmosphere. A special acknowledgment to Dr. Carlos Maciel-Escudero for the invaluable discussions during a particularly challenging phase of my PhD, with additional thanks for his assistance with Spanish translations.

I extend my gratitude to the members of the 2D Nanophotonics group at DIPC, including Nathaniel Capote-Robayna, Kateryna Domina, Kirill Voronin, Olga Matveeva, Jehyeok Ryu, and Dr. Gonzalo Álvarez-Pérez, for their warm and supportive environment.

My thanks to Dr. Pablo Alonso-González for hosting me in the Quantum Nano-optics lab

at the University of Oviedo and sharing valuable insights on s-SNOM nanoimaging. I am grateful to all members of the group, especially Dr. Javier Taboada-Gutiérrez, Dr. Jiahua Duan, Ana Fernández-Tresguerres, Christian Lanza-García, and Abel Martínez-Suárez.

To all my friends from Perm and Moscow, thank you for your support, advice, and the many shared moments that have lightened my journey. I extend my thanks to Natalia for her presence and support at the beginning of this PhD journey. Igor and Marina deserve special thanks for our Zoom calls, which were more than simple conversations. They were beacons of hope and encouragement, filled with laughter and insights, highlighting the strength and joy of our friendship.

I wish to express my heartfelt thanks to Dilia, whose encouragement has been crucial during moments of doubt and uncertainty. Her belief in my abilities has consistently served as a source of strength, which helps me move forward.

Finally, I owe a tremendous thank you to my family, who have been the foundation of everything. My mother and father have provided endless support and love. My brother and sister-in-law have been sources of invaluable encouragement. Special thanks to my incredible nephews, Viktoria and Georgiy, who brought smiles during the most challenging days. Their delight and enthusiasm have often been the uplift I needed to push through. Without all of you, I would not have come this far.